A Study of Areas of Low Radio-Thermal Emissivity on Venus

by

Robert Joseph Wilt

Submitted to the Department of
Earth, Atmospheric, and Planetary Sciences
in partial fulfillment of the requirements for the degree of

Doctor of Philosophy in Planetary Science

at the

MASSACHUSETTS INSTITUTE OF TECHNOLOGY

September 1992

Author .....
Department of Earth, Atmospheric, and Planetary Sciences
7 August, 1992

Certified by .....
Gordon H. Pettengill
Professor of Planetary Physics
Thesis Supervisor

Accepted by .....
Thomas H. Jordan
Chairman, Departmental Committee on Graduate Students

A Study of Areas of Low Radio-Thermal Emissivity on Venus

by

Robert Joseph Wilt

Submitted to the Department of Earth, Atmospheric, and Planetary Sciences
on 7 August, 1992, in partial fulfillment of the
requirements for the degree of
Doctor of Philosophy in Planetary Science

Abstract

Observations performed by the Magellan radiometer experiment have confirmed previous findings that a few regions on Venus, primarily at higher elevations, possess unexpectedly low values of radiothermal emissivity, occasionally reaching as low as 0.3. Values of emissivity below 0.7 occur over about 1.5% of the surface, and are associated with several types of feature, including highlands, volcanoes, tectonically uplifted terrain, and impact craters. There is a strong correlation of low emissivity and high elevation, but rather than decreasing gradually with elevation, the emissivity drops rapidly in a small altitude range above a certain "critical radius." The altitude at which the change in emissive properties occurs varies from feature to feature; on average, it lies at a planetary radius of about 6054 km. Notable exceptions to the association of low emissivity and high elevation exist; for example, Lakshmi Planum, Maat Mons, and the summits of many volcanoes display high emissivities at high elevations, while in some impact craters and plains areas we find low emissivities at low elevations.

Two possible explanations for low emissivities have been advanced: (1) emission from a highly reflective single interface between the atmosphere and a surface material having a bulk dielectric constant of order 80 ("high-dielectric" model); and (2) emission from the surface of a low-loss soil having a more usual permittivity (of order 2) which contains subsurface scatterers composed of ordinary rock materials ("volume scattering" model). Theoretical results and Monte Carlo simulations are used to show that the previously proposed volume scattering model cannot account for the observed emissivities; however, scattering from a material with very low loss (loss factor of order 10^{-3} or less) containing subsurface voids could produce the observed results. Consideration of the two models in light of the Magellan observations leads us to believe that the low emissivities on Venus result from the creation of a high--dielectric material by surface-atmosphere interaction, probably a loaded dielectric containing a conductive mineral.

Thesis Supervisor: Gordon H. Pettengill
Title: Professor of Planetary Physics

Acknowledgements

I would like to express my sincerest gratitude to my thesis advisor, Gordon Pettengill, whose guidance and encouragement were instrumental in helping me to complete this work. Special thanks also go to Peter Ford for invaluable scientific and technical assistance, and to Joan Quigley, for technical help and for her cheery company.

I also wish to thank the following individuals for helpful conversations or other assistance: Sean Solomon, Roger Burns, John Wood, Ted Madden, Stan Zisk, Bruce Hapke, Fang Liu, and Anita Killian.

Finally, I extend my warmest appreciation to my parents, Loretta and Herb Wilt, and to the rest of my family and friends, for their continued patience and support.

Contents

List of Figures

List of Tables

Chapter 1

Introduction

Radiometry is the study of the thermal emission of electromagnetic radiation from matter. The main factors controlling the intensity of radiation of a particular frequency emitted from a surface are (1) the physical temperature of the surface, (2) the electrical properties of the material (or materials) composing the surface (i.e. the permittivity and permeability), and (3) the geometric properties of the surface (surface roughness, subsurface distribution of materials, etc.). If the physical temperature of the surface is known, we may compare the observed radiated intensity to the intensity of radiation which would be emitted by a blackbody of the same temperature; the ratio of the two is known as the emissivity. With previous knowledge of the electrical properties of various materials, and of the effects of geometry on emission, we may use measured values of emissivity to place constraints on the possible composition and properties of surfaces.

Radiometric studies of Venus began over thirty years ago. Earth-based radio observations started, quite naturally, with measurements of disk-integrated brightness temperature. The first observations, in the late 1950s and early 1960s, measured a brightness temperature of about 600K for wavelengths greater than 3 cm [13]. Techniques have been improved over the years, and earth-based interferometry is now used to resolve large features on the surface [9]. Spacecraft radiometric observations, however, far exceed earth-based measurements in both resolution and global extent. The first spacecraft measurement, by Mariner 2 in late 1962, observed limb darkening,

and thus served to establish that the high brightness temperature was a result of a hot surface, rather than an atmospheric phenomenon [13]. An extensive radiometric survey of the surface was made in the late 1970s, by the Pioneer Venus radar mapper [21]. The primary purpose of the PV radiometric measurements was to monitor the stability of the radio receiver; the use of the calibration data as a measurement of variations in surface emissivity was not part of the original mission plan [61]. About 94% of the surface was observed, with a maximum surface resolution of 90 km at periapsis. The resolution deteriorates rapidly with higher spacecraft altitude, though, and because of the large orbital eccentricity of PV, the radiometric footprint size was well over 2000 km at the northern and southern fringes of coverage. The major features in the emissivity map of Venus were observed, but the details had to be left for a future mission.

Magellan reached Venus in August of 1990, and is still returning data as of July 1992. Magellan is primarily a radar mapping mission, so the ability to perform radiometric measurements was easily incorporated into the design. About 97% of the surface has been observed to date. The combination of a narrower antenna beamwidth and a less eccentric orbit than Pioneer Venus allow Magellan a better surface resolution across the entire range of coverage; the footprint size is about 20 km at periapsis, and increases to only 85 km at the northern and southern fringes [58]. Looking at the radiometry data in conjunction with the Magellan altimetric and SAR imaging data, we are for the first time able to study the detailed behavior of surface emissivity, and compare it to the surface geology and topography.

This work will concentrate on those parts of the surface where the radio emissivity (as measured by Magellan) is unusually low. The global mean value of emissivity measured during the first mapping cycle was 0.845 [60]; for present purposes, we will use a (somewhat arbitrary) value of 0.7 as an upper limit for what will be considered an unusually low emissivity. This constitutes about 1.5% of the planet's surface, in over 40 distinct areas. For a perfectly smooth surface at normal incidence, an emissivity of 0.7 correspond to a dielectric constant of 12; in comparison, common terrestrial basalts have typical dielectric constants of 5 to 9 at similar frequencies[5,

74]. The most interesting areas are those where the emissivity falls as low as 0.3. Such values require either materials with dielectric constants in excess of 100, or some more subtle mechanism, such as highly efficient volume scattering.

Chapter 2 of this work covers background information. First we define some commonly misused terms; following that we define emissivity and describe its relationship to surface reflectance. The last part of the chapter describes the Magellan radar and radiometer experiments.

Chapter 3 is a study of the areas of the surface where the emissivity falls below 0.7. The areas are listed and sorted by morphology; representative areas are described in detail. Then we explore the relationship between emissivity and altitude, and attempt to find a "critical radius" at which the emissivity characteristics of the surface change.

Chapters 4 and 5 investigate possible causes of low radiothermal emissivity on Venus. Chapter 4 begins with a review of the dielectric properties of materials and the emissivity of smooth surfaces. We then review data on the electrical properties of rocks and minerals, with special attention to those with high dielectric constants. The last part of the chapter discusses the possibility of high-dielectric surfaces on Venus. Chapter 5 investigates volume scattering, and presents results of theoretical models and of Monte-Carlo simulations which place constraints on the properties of surface materials which could produce the observed effects.

Chapter 6 summarizes the results, and points out some possible measurements which could discriminate between high-dielectric surfaces and volume scattering.

Chapter 2

Background

This chapter contains definitions of some commonly confused terms, a review of the theory of emissivity, and a description of the Magellan radar mapper and radiometer.

2.1 Confusing Terms

Certain terms are often used with slightly different meanings by different authors; each reader's understanding of these terms may be slightly different, depending on his background. To avoid later confusion, this section defines these terms as used in this paper.

2.1.1 Intensity

Several slightly different sets of terminology to describe the power of a beam of radiation exist; we will use the following:

Flux density is the power of a perfectly collimated (parallel) beam of radiation, per unit frequency, per unit area normal to the beam. Since the beam never diverges, flux density does not decrease with distance from the source. This quantity is used mainly in theoretical expressions, or as a local approximation to the diverging radiation from a real source, at a great distance from that source.

Radiant intensity is the power of a diverging beam, per unit frequency, per unit solid angle. These are the units in which the radiation pattern of an antenna, or of a

scattering surface or object, are usually expressed.

Intensity, or *brightness*, is the quantity actually measured by a radiometer system. *Brightness* is used in conjunction with surfaces; it is the power falling on (or emitted by) a surface, per unit frequency, per unit solid angle, per unit area normal to the direction of observation (or emission). *Intensity* is used to refer to radiation "in flight"; it is the power of a diverging beam of radiation, per unit frequency, per unit solid angle, per unit area normal to the direction of the beam. This quantity does not decrease with distance from the source, so long as the source is resolved; the power per unit area falling on a target decreases with distance at the same rate as the solid angle subtended by the source.

In the literature, the unmodified term *intensity* is at times used to mean any of these three quantities. In this work, we will use it only as described above; this seems to be its most common usage in papers on radiative transfer theory.

2.1.2 Reflectance and Reflectivity

In scattering theory, there are several terms describing the reflective properties of a surface. Each is defined in terms of the collimation and extent of the source and of the detector, and (when applicable) are functions of the direction of the source, (ϕ_0, θ_0), and/or the detector, (ϕ, θ). (For more information, see [33, 35].)

The *bidirectional reflectance*, $R_{dd}(\phi, \theta; \phi_0, \theta_0)$, is defined as the ratio of the brightness received at a detector viewing a surface from a particular direction, to the flux density incident on the surface from a (possibly different) particular direction.

The *directional-hemispherical reflectance*, $R_{dh}(\phi_0, \theta_0)$, is the ratio of the brightness reflected by a surface, integrated over the entire upper hemisphere, to the flux density incident on the surface from a particular direction.

The *hemispherical-directional reflectance*, $R_{hd}(\phi, \theta)$, is the ratio of the brightness received at a detector viewing a surface from a particular direction, to the brightness incident on the surface, integrated over the entire upper hemisphere.

Finally, the *bihemispherical reflectance*, R_{hh}, is the ratio of the brightness reflected by a surface, integrated over the entire upper hemisphere, to the brightness incident

on the surface, integrated over the entire upper hemisphere.

Reflectivity has a particular meaning in the context of the Pioneer Venus and Magellan radar studies of Venus. It refers to the normal-incidence Fresnel reflection coefficient of the surface. Reflectivity is measured by radar altimeter, simultaneously with altitude; its value is obtained by fitting a particular model of the surface (the Hagfors model) to the radar echo returned from the surface. This is discussed in section 2.3.3.

2.2 Theory of Emissivity

2.2.1 Emissivity

(Some of the material in this section follows [75].)

A blackbody is an ideal, perfectly opaque material that absorbs all radiation incident upon it at all frequencies. As well as being a perfect absorber, a blackbody is a perfect emitter of incoherent, unpolarized radiation. Planck's radiation law describes the emission from a blackbody. According to this law, the surface of a blackbody of temperature T emits unpolarized radiation uniformly in all directions with brightness

$$B_\nu = \frac{2h\nu^3}{c^2} \frac{1}{e^{h\nu/kT} - 1} \tag{2.1}$$

where B_ν is the monochromatic specific intensity of emitted radiation at frequency ν. The units of B_ν are power per unit frequency, per unit solid angle, per unit area normal to the direction of emission. h, k, and c are Planck's constant, Boltzmann's constant, and the speed of light in vacuum, respectively. At low frequencies, where $h\nu/kT \ll 1$, we may use the approximation

$$B_\nu = \frac{2\nu^2 kT}{c^2}. \tag{2.2}$$

This is the Rayleigh-Jeans law, and is applicable at radio and microwave radar frequencies at temperatures of interest in the Solar System. In radiometric work, we

often make use of the linear relationship between brightness and temperature as expressed by the Rayleigh-Jeans law, and speak not of "brightness" but of the equivalent "brightness temperature."

Real surfaces do not emit perfectly; they radiate only a fraction of the power that a blackbody of the same temperature would radiate. This fraction is known as the emissivity. Emissivity is a function of several variables, including the materials composing the body, the radiation frequency and polarization, the emission direction, and the surface and subsurface geometry. It may also depend on other factors, such as temperature and pressure, to the extent that they influence the properties of the surface materials.

To formalize the definition of emissivity, let B_{rad} be the intensity of radiation emitted by a surface at physical temperature T_p, at frequency ν, in a direction at an angle ϕ from the surface normal. (We will assume emissivity to be independent of θ, the azimuthal viewing direction, throughout this work.) Let B_ν be the intensity of radiation emitted by a blackbody at the same temperature and frequency. Then

$$e(\phi) = \frac{B_{rad}(\phi)}{B_\nu}. \tag{2.3}$$

$e(\phi)$ is sometimes called the "directional emissivity" [35] but we shall refer to it simply as the emissivity. The brightness temperature of the surface, T_b, is the temperature of a blackbody which would emit the observed brightness B_{rad}. If T_p and ν are within the regime of the Rayleigh-Jeans law,

$$e(\phi) = \frac{T_b(\phi)}{T_p}. \tag{2.4}$$

When we observe a surface from a given direction, we see the sum of radiation from two distinct sources. First, we see the radiation emitted by the surface into this direction. Second, we see the radiation which is incident on the surface from above (the sky) and scattered into this direction. We can write

$$\begin{aligned} B_{obs}(\phi) &= B_{rad}(\phi) + B_{sca}(\phi; sky) \\ &= e(\phi)B_\nu + B_{sca}(\phi; sky) \end{aligned} \tag{2.5}$$

where

$$B_{sca}(\phi; sky) = \int\int_{sky} R_{dd}(\phi, \theta; \phi', \theta')\, B_{sky}(\phi', \theta')\, \sin\phi'\, d\phi'\, d\theta' \tag{2.6}$$

$R_{dd}(\phi, \theta; \phi', \theta')$ is the bidirectional reflectance, and $B_{sky}(\phi', \theta')$ is the brightness of the sky. If the sky is uniformly bright,

$$B_{sca}(\phi; sky) = R_{hd}(\phi)\, B_{sky} \tag{2.7}$$

where $R_{hd}(\phi)$ is the hemispherical-directional reflectance [35];

$$R_{hd}(\phi) = \frac{1}{2\pi} \int\int_{sky} R_{dd}(\phi, \theta; \phi', \theta')\, \sin\phi'\, d\phi'\, d\theta'. \tag{2.8}$$

Imagine that the surface is enclosed in a blackbody cavity of temperature T, and allowed to come into thermodynamic equilibrium. The isotropic radiation intensity above the surface is B_ν. In order to maintain thermodynamic equilibrium, the radiation intensity incident on the surface from any direction must be exactly balanced by radiation emitted and scattered into that direction from the surface. Thus we require $B_{obs}(\phi) = B_\nu$ and equation 2.5 becomes

$$B_\nu = e(\phi)B_\nu + R_{hd}(\phi)B_\nu \tag{2.9}$$

or

$$e(\phi) = 1 - R_{hd}(\phi). \tag{2.10}$$

This equation is sometimes useful in calculating the emissivity of theoretical surfaces, as will be seen later.

2.2.2 Emissivity vs. Radar Backscatter

As has just been seen, the emissive and reflective properties of a surface are intimately linked, the general rule being that high emissivity is associated with low reflectance, and *vice versa.* Measurements of radar backscatter are measurements of bidirectional reflectance in a single direction and thus cannot be converted directly to emissivity; however, inasmuch as bidirectional and hemispherical-directional reflectances are related, they do serve as an indicator of the possibility of unusual emission properties in a region. The quantity which is generally reported from radar backscatter experiments is the specific radar cross section, σ_0. The radar cross section σ is defined as the area of an isotropic scatterer, normal to the illumination, that would yield the observed echo intensity if it were placed at the target's location. The specific radar cross section is then defined as the radar cross section normalized by the actual (not projected) surface area [56]. A slightly different statement of the definition of σ is [78]:

$$\sigma = 4\pi \frac{\text{Power scattered back per steradian}}{\text{Power incident per unit area normal to the beam}}. \tag{2.11}$$

This can also be expressed in terms of bidirectional reflectance:

$$\sigma = 4\pi R_{dd}(\phi_0, \theta_0; \phi_0, \theta_0). \tag{2.12}$$

Note that σ_0 can easily exceed unity, if the backscatter is highly directional.

Radar has certain advantages over radiometry, the most prominent being the high surface resolution available when using delay-doppler mapping techniques. On the other hand, radar backscatter is usually much more dependent on surface geometry; for example, parts of the surface with favorable tilts can easily dominate the signal, and rough (on the scale of a wavelength) surfaces may return much different echoes than do smooth surfaces of the same composition. The emissivity of the surface is not so strongly influenced by the surface geometry as is its backscatter.

2.3 The Magellan Radar Mapper and Radiometer

2.3.1 Overview

Magellan was launched from Kennedy Space Center, on board the Space Shuttle Atlantis, on May 4, 1989, and deployed that same day. After a journey which carried it 580° around the sun, Magellan arrived at Venus on August 10, 1990. Magellan was placed in a highly inclined (85.5°) and somewhat eccentric (0.39) orbit, which carries it nearly over the north pole at an altitude of 2225 km, and southward to periapsis over latitude 9.9°N at an altitude of 294 km. The orbital period of the spacecraft is 3.26 hours. [64]

Magellan carries a single scientific instrument, a 2.385 GHz (12.57 cm) radar system. This instrument is used in three modes: side-looking synthetic aperature imaging (SAR), altimetry, and radiometry. The spacecraft is equipped with two antennas. The first is a 3.7 m diameter parabolic high-gain antenna (HGA), with angular beam width 2.1° (along track) by 2.5° (across track); this antenna is used in the SAR and radiometric modes. (It should be noted that during normal operation in the first mapping cycle, the orientation of the HGA was such that it sent and received radiation linearly polarized in the horizontal direction—that is, parallel to the surface of the planet.) The second is a small horn antenna, with beam width 10° (along track) by 30° (across track); it is used for altimetry. The two antennas are fixed to the spacecraft structure; aiming them requires orienting the spacecraft itself. During the approximately 40 minutes of data-taking during each orbit, the three modes of operation are interleaved, resulting in full coverage along the orbit in each mode. Data are digitized and recorded on magnetic tape, and later sent back to earth (using the HGA). [58]

The nominal Magellan mission was 243 days, the time it took Venus to rotate once below the plane of the spacecraft's orbit. During this period nearly 1800 spacecraft orbits occurred, and over 90% of the surface was mapped. Subsequent mapping cycles have (to date) been used to fill in data gaps and to view the surface at different angles of incidence. Future possibilities include gravitational mapping, high-resolution to-

pography through interferometry, and changing the orbit to obtain higher resolution imaging data. [64]

The following sections discuss each of the three experiments in more detail. Most of the technical information on the three experiments was found in [58, 22, 60]; additional sources are cited where appropriate.

2.3.2 SAR Imaging

The SAR experiment uses standard delay-doppler radar mapping techniques to produce high-resolution maps of the radar backscatter from the surface. Doppler resolution is achieved through the motion of the spacecraft along its orbit; delay resolution is achieved by viewing the surface at an angle, so that echoes from different parts of the surface within the antenna beam arrive at different times. Delay resolution on the surface would be maximized by viewing the surface at as large of an angle of incidence as possible; however, the returned power and signal-to-noise ratio must also be considered. Because of this, the angle of incidence on the surface is at most 47° at periapsis, and is adjusted downward as the altitude of the spacecraft increases.

In SAR mode, the radar transmits some number of coherent pulses toward the surface (a SAR "burst"), and monitors their echoes. The number of pulses is adjusted from 150 (periapsis) to 800, to maintain a constant along-track resolution of 120 m on the surface (this results in about 5 bursts per second at periapsis, to slightly less than one per second near the edges of coverage). The across-track resolution varies with the viewing angle, from 120 m at periapsis, to 280 m near the edges of coverage. A single point on the surface may be illuminated by several successive SAR bursts; the number of bursts (or "looks") varies with the spacecraft velocity, from a minimum of 5 at periapsis to 17 near the edges of coverage.

Table 2.1 summarizes the SAR surface resolution and incidence angle as a function of spacecraft position.

The echo samples are returned to earth, where they are processed into maps of radar backscatter. The data products released to the scientific community are mosaics known as MIDRs. The quantity mapped in MIDRs is the normalized specific radar

cross section, in decibels; it is obtained by dividing the specific radar cross section of the surface, determined by SAR processing, by a predicted planetary scattering function for that particular angle of incidence [49].

Backscatter from a planetary surface is a rather complicated subject, and thus detailed study of the SAR images requires careful consideration of a number of factors. The ultimate factor controlling the reflection of radiation from a material is its dielectric constant. However, in situations where the surface material is very similar in most places, geometry plays the leading role in determining variations in radar backscatter strength. At angles of incidence below about 20°, quasi-specular reflection dominates; most of the echo comes from radar-smooth surface facets which happen to lie in an orientation perpendicular to the radar's line of sight. At higher angles, fewer surface facets have such a favorable orientation, and diffuse scattering by surface roughness on the scale of a radar wavelength becomes the dominant mechanism. Longer-wavelength slopes in terrain, such as valleys, mountains, etc., can alter the local angle of incidence significantly; such slopes will appear as greater (brighter) or lesser (darker) values of backscatter, depending on the orientation of the slope. Such slopes may also result in geometric distortions of geologic features on the SAR maps, since the SAR processing which performs the geometric mapping projections does not have prior knowledge of the detailed topography of a region.

2.3.3 Altimetry

In altimetric mode, the radar sends 17 coherent pulses through the horn antenna, and records the echo. Near periapsis, an altimetric burst follows every third SAR burst. Further from periapsis, the "skip factor" is decreased; near the edges of coverage, an altimetry burst follows every SAR burst. The surface resolution of the altimeter is determined by the time and frequency characteristics of the radar signal, as well as the spacecraft orbital characteristics. Along-track resolution is achieved through the doppler shifts of the returned echoes; across-track resolution is controlled by the radar waveform, and this depends on the spacecraft altitude. The across-track resolution varies from 12 km at periapsis to 29 km near the edges of coverage; the along-track

resolution is about 2 km at periapsis, and 15 km near the edges of coverage. In the standard data reduction, in order to maintain an acceptable signal-to-noise ratio near periapsis, the data are effectively resampled to an along-track footprint size of at least 8 km.

The horn antenna is at a fixed 25° offset from the HGA, and thus does not usually point directly at the nadir. The large across-track beamwidth, however, insures that even when the horn antenna is pointed at its maximum of 22° from nadir, the gain in the direction of nadir will still be sufficient to receive an echo of acceptable strength.

Table 2.2 summarizes the altimeter footprint size and the antenna pointing direction as a function of spacecraft position.

Echoes from a particular location on the surface are combined, then analyzed in a model-dependent fashion to yield simultaneous estimates of range, meter-scale surface slope (roughness), and normal-incidence surface reflectivity. The model of surface backscatter used in the analysis is given by Hagfors [32]. According to the Hagfors model, the relationship between the specific radar cross section σ_0 and the angle of incidence ϕ is

$$\sigma_0(\phi) = \frac{C\rho}{2}\left(\cos^4\phi + C\sin^2\phi\right)^{-\frac{3}{2}} \tag{2.13}$$

where ρ is the normal-incidence surface reflectivity, and C is the Hagfors parameter, interpreted to be the inverse square of the RMS surface slope at a scale of meters to tens of meters. The processed data are released in two forms: global maps of topography, meter-scale slope, and reflectivity, with pixels at 5 km intervals; and composite records containing the data from each altimetry footprint.

Although the altimetry experiment and data processing described above determines planetary radius quite well over most of the surface, there are some areas where deviations from the Hagfors surface model are sufficient to throw the data reduction process into chaos. For example, a strong echo from a feature located at some horizontal distance from nadir may interfere with the signal from nadir, if this feature has favorable tilts and/or relatively strong reflectivity. The problem is even worse in

certain parts of the highlands, where there are large surface tilts and substantial variations of height even within the altimeter footprint. Many of the problem and suspect data points have been removed from the data set, but some still remain; interesting and unusual topographic features must be viewed with some caution, and their properties confirmed by close examination of the radar echoes and of the corresponding portion of SAR images.

2.3.4 Radiometry

A radiometric observation is made just prior to each SAR burst. In each observation, the radio receiver is connected either to a dummy load, which is used for calibration purposes, or to the HGA, which is pointed at the surface. The angle of incidence on the surface is the same as for the SAR observations. The size of the radiometric footprint is determined by the angular beamwidth of the HGA; the footprint size varies from 15 km (along-track) by 23 km (across-track) at periapsis, to over 75 km by 90 km at the edges of coverage. Table 2.3 summarizes the radiometer footprint size and incidence angle as a function of spacecraft position. Adjacent radiometer footprints overlap both along the orbit (despite the interspersed calibration measurements) and between orbits (even at periapsis, where the ground track of adjacent orbits reach their maximum separation). The system integrates the power received in a 50 ms period, over a 10 Mhz bandwidth; this power is subsequently interpreted as an observed brightness temperature, and used to calculate the brightness temperature of the surface (see below). The standard deviation of statistical fluctuations associated with each measurement of antenna noise temperature is about 1.8K; when overlapping observations are merged, the fluctuations are reduced to less than 1.0K. Tests of the system made before launch suggest that it can determine the antenna noise temperature to an absolute accuracy of about 15K, and can detect short-term variations (adjacent footprints along an orbit) as small as 2K.

The integrated noise power is calibrated with the dummy load measurements, corrected for a number of instrument factors, and converted to an equivalent noise temperature, T_{noise}. The goal is to convert this to a value of surface emissivity. The

first step is to correct T_{noise} by subtracting from it the equivalent brightness temperature of radiation received from outside the main lobe of the antenna pattern. The corrected value will be T_{obs}. An exact determination of T_{obs} would require knowledge of the complete HGA pattern, as well as knowledge of the incident brightness from all directions other than the direction of observation. For cost reasons, the HGA pattern was not measured prior to launch. In the absence of this information, the data reduction team has assumed an antenna pattern with a beam efficiency of 0.80, which is typical for antennas of similar design. This means that 80% of the radiation entering the HGA comes from the main lobe, and thus the area under observation, and 20% originates outside the main lobe. Power received from outside the main lobe may originate from other portions of the surface of the planet, from the sky, or even from the sun. The overwhelming majority is assumed to come from the planet; the integrated sidelobe response is calculated to be the fraction of 4π solid angle filled by the planetary disk, multiplied by a mean brightness temperature of 635K. The equivalent noise temperature is thus given by the sum

$$T_{noise} = 0.80\, T_{obs} + 0.20\ (635\text{K})\ \frac{1}{2}\left(1 - \frac{\sqrt{h(2R_V + h)}}{R_V + h}\right) \tag{2.14}$$

where h is the spacecraft altitude and R_V is the radius of Venus. This equation is easily solved for T_{obs}.

The corrected observed brightness is also the sum of several factors. The main contribution is from the surface itself, the product of the physical temperature of the surface, T_p, and the emissivity of the surface in the direction of observation, e. This contribution is reduced by atmospheric attenuation; Υ will denote the one-way integrated atmospheric transmission coefficient, whose value is derived from previous radio observations [43]. The second contribution, T_{atm}, is from the atmosphere between the surface and the spacecraft; it is related to Υ and its value is also determined from data in [43]. The third contribution is the radiation from the sky reflected by the surface into the direction of the spacecraft. The reflected radiation consists of two parts, radiation from outside of the atmosphere, and radiation from the atmosphere.

For an exact solution, we would need to know the values of bidirectional reflectance from the entire sky into the direction of the spacecraft, as well as the atmospheric contribution and attenuation in each direction, and the brightness of the sky above the atmosphere in each direction. The matter is greatly simplified by assuming that the main contribution is from the specular direction, that the contribution from the sky above the atmosphere is the brightness of the cosmic background radiation, and that the surface reflection coefficient is $1 - e$.

The expression for the observed brightness temperature T_{obs} is thus

$$T_{obs} = T_{atm} + \Upsilon\, e\, T_p + \Upsilon(1 - e)(T_{atm} + \Upsilon\, 2.7\text{K}). \tag{2.15}$$

Solved for emissivity,

$$e = \frac{T_{obs} - T_{atm} - \Upsilon(T_{atm} + \Upsilon\, 2.7\text{K})}{\Upsilon\, T_p - \Upsilon(T_{atm} + \Upsilon\, 2.7\text{K})} \tag{2.16}$$

The one parameter which has not been discussed is the physical temperature of the surface, T_p. Determination of the physical surface temperature on Venus is relatively straightforward. Because of the thick carbon dioxide atmosphere, which acts as an efficient greenhouse insulator, the vertical structure of the lower atmosphere is very nearly adiabatic and rather stable against temperature changes; at a given elevation, the surface temperature is believed to be the same, within about 15K, anywhere on the planet. The temperature changes with altitude at a rate of -7.7K per kilometer (the adiabatic lapse rate is -8.9K per kilometer); the temperature at the mean Venus surface (radius 6051.9 km) is approximately 737K (see table 2.4) [65]. Determination of planetary radius at the point on the surface under observation is made from the pre-Magellan topographic model.

It should be clear from the preceding discussion that a number of approximations have been used in the calculation of surface emissivity from the observed noise power. A second pass of data analysis could improve some of the deficiencies; however, it is not clear whether improved analysis could provide any new information which would

be useful at the moment. The dominant features of the surface emissivity map, such as the areas of extremely low emissivity, are quite apparent already, and still await explanation. The major shortcoming of the radiometry experiment, despite the vast improvement it represents over previous efforts, is its poor surface resolution, especially in light of the high resolution of the SAR images. Improvements in radiometer resolution could be achieved by changes in the spacecraft orbit; however, this does not seem to be a priority at the present time.

Table 2.1: Magellan SAR surface resolutions and incidence angles.

Spacecraft True Anomaly (deg)	Spacecraft Altitude (km)	Latitude (deg)	SAR Resolution Along Track (m)	SAR Resolution Across Track (m)	SAR Incidence Angle (deg)
±70	1800	+80,-60	120	255	16
±60	1360	+70,-50	120	210	20
±50	1020	+60,-40	120	175	25
±40	751	+50,-30	120	150	30
±30	549	+40,-20	120	135	36
±20	407	+30,-10	120	130	42
±10	322	+20,0	120	125	46
0	293	+10	120	120	47

Table 2.2: Magellan altimeter footprint sizes and incidence angles (center of beam).

Spacecraft True Anomaly (deg)	Spacecraft Altitude (km)	Latitude (deg)	Altimeter Footprint Size Along Track[a] (km)	Altimeter Footprint Size Across Track (km)	Altimeter Incidence Angle (deg)
±70	1800	+80,-60	15	27	-9
±60	1360	+70,-50	11	24	-5
±50	1020	+60,-40	8(7.1)	21	0
±40	751	+50,-30	11(5.6)	19	5
±30	549	+40,-20	8(4.2)	16	11
±20	407	+30,-10	9(2.8)	14	17
±10	322	+20,0	9(2.2)	13	21
0	293	+10	8(1.9)	12	22

[a]Values in parentheses are maximum resolution possible if the footprint size is not constrained.

Table 2.3: Magellan radiometer footprint sizes and incidence angles.

Spacecraft True Anomaly (deg)	Spacecraft Altitude (km)	Latitude (deg)	Radiometer Footprint Size Along Track (km)	Radiometer Footprint Size Across Track (km)	Radiometer Incidence Angle (deg)
±70	1800	+80,-60	66	79	16
±60	1360	+70,-50	52	63	20
±50	1020	+60,-40	42	52	25
±40	751	+50,-30	32	42	30
±30	549	+40,-20	25	34	36
±20	407	+30,-10	19	29	42
±10	322	+20,0	16	25	46
0	293	+10	15	23	47

Table 2.4: Temperature and pressure of the near-surface atmosphere of Venus, as given by Kliore et al. [43].

Radius (km)	Temperature (K)	Pressure (bars)
6064	643.2	41.12
6063	650.6	44.16
6062	658.2	47.39
6061	665.8	50.81
6060	673.6	54.44
6059	681.1	58.28
6058	688.8	62.35
6057	696.8	66.65
6056	704.6	71.20
6055	712.4	76.01
6054	720.2	81.09
6053	727.7	86.45
6052	735.3	92.10
6051	743.0	98.119
6050	750.7	104.532
6049	758.4	111.364
6048	766.1	118.642

Chapter 3

Areas of Low Radiothermal Emissivity on Venus

3.1 Introduction

Figure 3-1 presents the global distribution of emissivity determined by radiometric observations during the first eight months (cycle 1) of the Magellan mission. For these observations, the received linear polarization was maintained parallel to the surface; the angle of observation, measured from the surface normal, varied from 16° to 47° (see table 2.3). No adjustment to account for the varying angle has been made to the data; thus, typical values of emissivity tend to rise from about 0.82 at periapsis to about 0.87 near the north and south edges of observation. The mean global value of emissivity for the area observed is 0.845; the median is 0.851. About 91% of the surface of Venus was observed during cycle 1.

Table 3.1 lists the distribution of emissivity by surface area. It is evident from this table, and from the global map, that there is a small amount of the surface whose emissivity is unusually low. In this chapter we will list and discuss those locations on the surface where the measured value of emissivity falls to 0.70 or below. The selection of this cutoff value is somewhat arbitrary; it was chosen high enough to include a diverse selection of areas, but low enough to keep their number workable.

Figure 3-1: (color plate) Global emissivity map of Venus in Mercator projection, covering latitude interval 70°S to 70°N. False color is used to show the values of (horizontally polarized) emissivity determined from the first 8 months of Magellan observations. Note that the color scale has been stretched to emphasize detail lying within the emissivity interval 0.8–0.9. (See [60].)

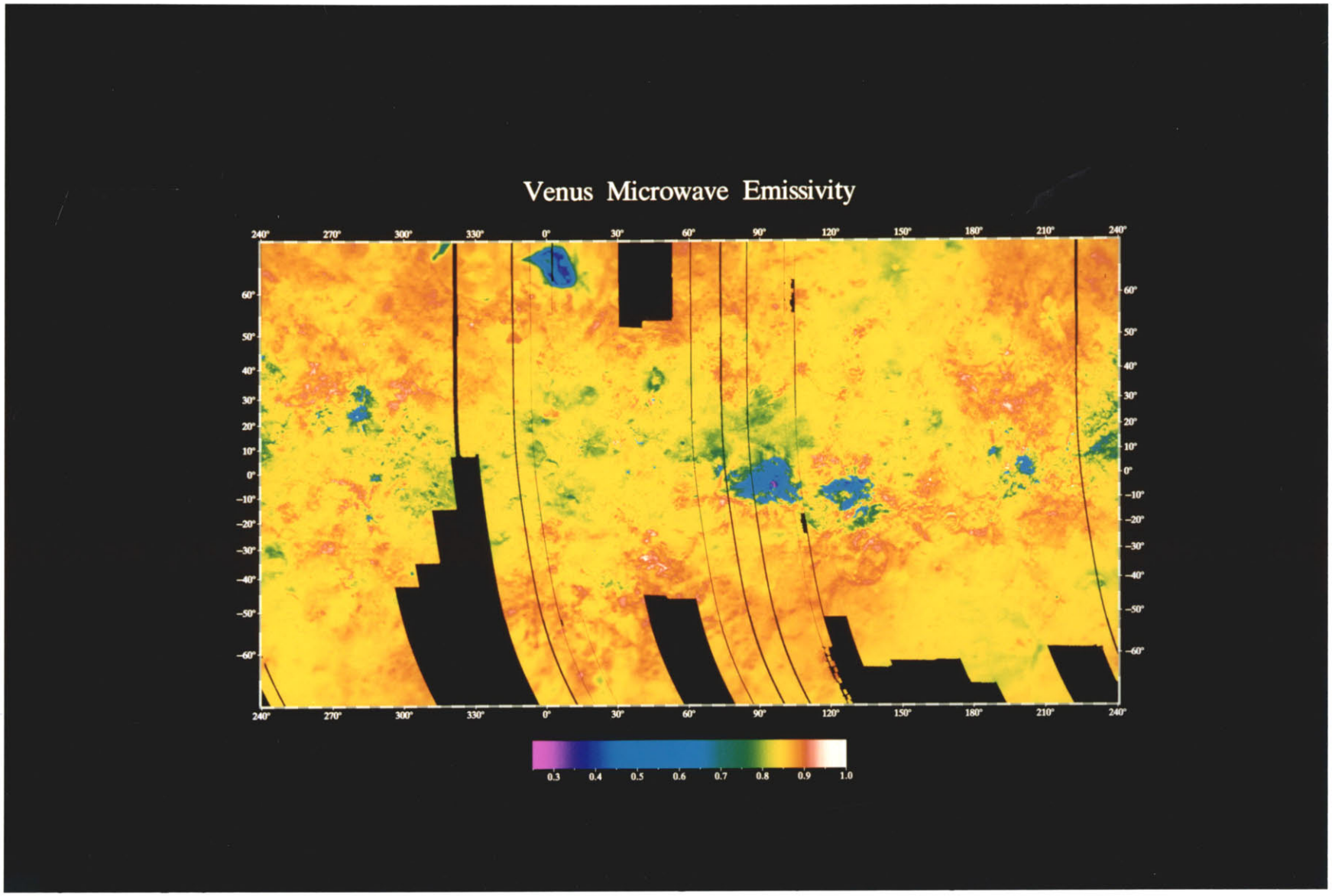
Venus Microwave Emissivity
240° 270° 300° 330° 0° 30° 60° 90° 120° 150° 180° 210° 240°
60° 50° 40° 30° 20° 10° 0° -10° -20° -30° -40° -50° -60°
0.3 0.4 0.5 0.6 0.7 0.8 0.9 1.0

Table 3.1: Distribution of emissivity on surface, by area

Emissivity Range	Area (km^2)	% of Area Observed	Cumulative % of Area Observed
0.0–0.1	0	0.00	0.00
0.1–0.2	0	0.00	0.00
0.2–0.3	194	< 0.01	< 0.01
0.3–0.4	320,291	0.08	0.08
0.4–0.5	1,377,037	0.33	0.41
0.5–0.6	1,987,141	0.47	0.88
0.6–0.7	2,631,192	0.63	1.51
0.7–0.8	19,615,720	4.69	6.20
0.8–0.9	381,686,000	91.20	97.40
0.9–1.0	10,874,977	2.60	100.00
Total	418,492,552	(91% of surface)	

We will, in fact, concentrate to a greater degree on the lowest emissivities, as they are the most difficult to explain.

The general correspondence between low emissivity (and high reflectivity) and high altitude has been recognized since the analysis of the Pioneer Venus data [59, 21]. The superior surface resolutions of the Magellan altimeter and radiometer permit us a better opportunity for detailed analysis of the relationship between the two. A goal of this chapter is to report what we have recently learned of the details of this relationship. In particular, we will examine the rapid decrease in emissivity with altitude which occurs above a certain altitude. It is hypothesized that the drop in emissivity above this "critical radius" is a result of a mineralogical phase change which creates or allows the existence of a material of high dielectric constant at high altitudes [59, 21, 57, 44].

A note on terminology: in this chapter, terms such as "bright," "medium," and "dark" will be used to describe the SAR backscatter intensity[1], a quantity which is controlled by dielectric properties of the surface material, by wavelength scale surface roughness, and by larger scale surface slopes. These terms are the natural ones to use

[1]that is, the normalized specific radar cross section—see section 2.3.2

when referring to SAR images; they are always used in a relative sense. Radiometric brightness temperature will never be addressed directly, but only through values of the inferred emissivity. Likewise, the terms "smooth" and "rough" will be used to describe the backscatter characteristics of an area. Smooth areas are those in which the backscatter remains relatively constant; rough areas are those where it varies, usually due to kilometer scale topography. Again, the terms are relative. Meter scale roughness, as measured by the altimetry experiment, is not addressed in this paper.

3.2 Low Emissivity Areas

Table 3.2 lists the 43 low emissivity features and areas that we have examined. In our study of these areas, we have found it convenient to divide them into a number of categories based on morphology. These categories are as follows:

- *Highlands* are large areas of bright ridged terrain and "tessera," sometimes invaded by darker, smoother areas. Examples are Ovda Regio, Thetis Regio, and Maxwell Montes. These three account for the preponderance of low emissivity terrain on Venus. Except for certain interesting dark features at the highest elevations, low emissivities are pervasive within the ridged terrain and tessera.

- *Large shield volcanoes* include Ozza Mons, Theia Mons, and Gula Mons. Most of the large shields are situated along rift systems. The lowest emissivities tend to be found in lava flows somewhat away from the summits; the summit areas are often dark areas of relatively high emissivity.

- *Rifted volcanoes* are those which have been partially or mostly disrupted by an underlying rift system. Low emissivities tend to be found just outside the rift valley, in the remaining lava flows.

- *Small volcanoes* include several features identified as volcanic mainly by emanating lava flows. In this category are the novae, a particular class of volcano characterized by strong radial fractures; they are usually associated with coronae or with polygonally shaped uplifted plateaus.

- *Ridges* are elevated linear features interpreted to have been raised to their present altitude by tectonic forces. The ridge along the south side of Dali Chasma is an example, as are the edges of plateaus and coronae associated with novae. Also included are other (nonlinear) areas which appear to have been uplifted.

- *Impact craters* such as Boleyn, Mead, Stanton, and Stuart show notable depressions in emissivity relative to the surrounding terrain. We do not include in this category craters lying in larger areas of low emissivity.

There is also a "miscellaneous" category for areas and features which did not fall into any of the above groups, or could not be identified. A few features have characteristics of more than one category.

3.2.1 Highlands

As mentioned above, the highland areas Ovda, Thetis, and Maxwell account for most of the low emissivity terrain on Venus. The surface of Thetis is mostly tessera, a type of surface which appears to have been tectonically folded in more than one direction and consists of a network of valleys and ridges [23, 36]. The tessera terrain is invaded in places by wide areas of smoother, darker surfaces. Ovda contains both tessera and terrain folded predominantly along a single direction (ridged terrain). Maxwell is primarily ridged terrain, with some tessera. Note that other areas at lower elevations comprising extensive tesseral formations, such as Fortuna Tessera (20°E, 65°N) and Alpha Regio (4°E, 25°S) do not show comparable reduced values of emissivity.

Figure 3-2 compares the topography and emissivity of Ovda Regio. The topographic irregularities in the region are due to the kilometer scale roughness of tessera and ridged terrain, which greatly complicates the determination of topography (see section 2.3.3). Emissivity is generally lower in the higher central parts of Ovda. Note, though, that the highest areas often show an increase in emissivity, as well as a darker signature in the SAR image. This dark material usually has sharp boundaries with surrounding bright material; bright edges along the west margins in the left-looking

Table 3.2: Areas of low radiothermal emissivity on Venus. Information includes the feature name and location, the maximum altitude found anywhere within the area, the total surface area with an emissivity less than or equal to 0.70, and the magnitude, location, and altitude of the minimum emissivity in the area. For some features, several additional local minima are listed.

Name or Description	Location Lat	Location Lon	Max. Radius	Area of $e \leq 0.70$ (km^2)	Minimum Emissivity Value	Lat	Lon	Radius
			Highlands					
Ovda Regio	3°S	90°E	6059.7	3113050	0.26	5.8°S	96.3°E	6055.4
Thetis Regio	8°S	127°E	6059.5	1489021	0.35	4.7°S	127.7°E	6055.4
north					0.35	4.7°S	127.7°E	6055.4
northeast					0.37	3.8°S	132.5°E	6055.7
south					0.43	12.1°S	128.6°E	6056.0
Maxwell Montes	65°N	3°E	6062.7	403713	0.37	64.3°N	7.6°E	6058.7
west					0.38	63.7°N	1.9°E	6060.1
east					0.37	64.3°N	7.6°E	6058.7
			Shield Volcanoes					
Ozza Mons	3.8°N	199.3°E	6058.5	400418	0.34	4.1°N	198.4°E	6056.5
west minimum					0.34	4.1°N	198.4°E	6056.5
northwest flows					0.47	5.4°N	199.1°E	6056.2
far north flow					0.52	9.1°N	202.6°E	6052.6
east flows					0.43	4.2°N	201.4°E	6055.2
southeast flows					0.44	2.4°N	200.6°E	6056.3
far southeast flow					0.63	4.4°S	206.6°E	6052.5
Theia Mons	23.6°N	280.2°E	6057.0	278397	0.38	23.8°N	278.7°E	6055.8
east flows					0.38	23.8°N	281.6°E	6055.7
west flows					0.38	23.8°N	278.7°E	6055.8
northeast flows					0.50	27.3°N	283.1°E	6056.1
south flows					0.58	19.1°N	281.9°E	6055.3
Sapas Mons	8.9°N	188.0°E	6055.6	57338	0.46	9.1°N	188.5°E	6054.2
Maat Mons	0.9°N	194.6°E	6060.2	19752	0.53	0.5°S	193.6°E	6055.8
bright south flow					0.53	0.5°S	193.6°E	6055.8
Tepev Mons	29.6°N	45.0°E	6056.7	7280	0.51	29.6°N	44.9°E	6056.2
Sekmet Mons	44.3°N	240.4°E	6053.9	5256	0.58	44.1°N	240.6°E	6053.5
Gula Mons	21.8°N	358.5°E	6055.6	4846	0.57	21.8°N	358.6°E	6055.4

Table 3.2: (continued) Areas of low radiothermal emissivity on Venus.

Name or Description	Location Lat	Lon	Max. Radius	Area of $e \leq 0.70$ (km^2)	Minimum Emissivity Value	Lat	Lon	Radius
				Rifted Volcanoes				
Rhea Mons	32.4°N	282.6°E	6058.5	66837	0.52	30.0°N	281.7°E	6055.5
east area					0.58	33.0°N	284.3°E	6054.9
central area					0.62	31.9°N	282.5°E	6056.2
north flows					0.61	34.5°N	283.0°E	6056.0
southwest flows					0.52	30.0°N	281.7°E	6055.5
(unnamed)	2.0°S	288.0°E	6055.0	28389	0.57	2.0°S	287.0°E	6053.4
east flows					0.60	1.7°S	288.4°E	6054.5
central area					0.63	1.9°S	287.6°E	6053.4
west flows					0.57	2.0°S	287.0°E	6053.4
(unnamed)	17.9°S	285.1°E	6056.5	24986	0.54	17.9°S	285.8°E	6054.9
northeast flows					0.54	17.9°S	285.8°E	6054.9
southwest flows					0.61	18.3°S	284.8°E	6054.4
(unnamed)	17.1°N	194.2°E	6055.5	8874	0.61	16.3°N	193.9°E	6054.8
(unnamed)	18.9°N	268.0°E	6055.6	8745	0.59	19.3°N	268.2°E	6051.8
north flows					0.59	19.3°N	268.2°E	6051.8
south flows					0.66	18.6°N	268.2°E	6053.5
southwest flow					0.63	18.2°N	266.8°E	6053.4
(unnamed)	5.3°N	291.2°E	6053.2	991	0.68	5.3°N	291.1°E	6052.4
				Small Volcanoes				
(nova)	0.7°N	34.4°E	6054.8	11653	0.43	0.6°N	34.6°E	6054.4
(small volcano)	24.2°N	263.8°E	6056.1	9456	0.60	24.5°N	263.8°E	6055.5
north flow					0.60	24.5°N	263.8°E	6055.5
south flow					0.62	23.5°N	263.8°E	6052.4
northeast flow					0.68	26.0°N	265.3°E	6052.6
(nova)	9.0°N	219.1°E	6055.1	5729	0.63	9.0°N	219.1°E	6054.4
(nova)	15.3°N	221.2°E	6055.8	5083	0.50	15.4°N	221.1°E	6055.2
(small volcano)	6.2°S	299.3°E	6054.5	4394	0.55	6.0°S	299.3°E	6053.6
(nova)	2.6°N	45.5°E	6053.8	4136	0.51	2.6°N	45.5°E	6053.4
(nova)	22.2°N	223.7°E	6055.7	4136	0.55	21.5°N	224.2°E	6055.3
(nova)	19.4°N	227.4°E	6056.0	3619	0.62	19.7°N	227.3°E	6055.0
(nova)	1.7°S	215.0°E	6054.8	2068	0.64	1.7°S	215.0°E	6054.4
(nova)	11.1°N	14.3°E	6053.8	1874	0.63	11.0°N	14.4°E	6053.6
(small volcano)	5.6°S	217.1°E	6055.5	1443	0.59	5.7°S	217.2°E	6055.2
(small volcano)	2.6°N	301.5°E	6053.8	1055	0.62	2.4°N	301.5°E	6053.7
(small volcano)	9.7°S	301.3°E	6054.5	108	0.69	9.8°S	301.2°E	6054.2

Table 3.2: (continued) Areas of low radiothermal emissivity on Venus.

Name or Description	Location Lat	Location Lon	Max. Radius	Area of $e \leq 0.70$ (km^2)	Minimum Emissivity Value	Minimum Emissivity Lat	Minimum Emissivity Lon	Minimum Emissivity Radius
			Ridges					
Hestia Rupes	2.3°N	73.3°E	6055.6	57553	0.48	2.5°N	73.7°E	6055.4
Pavlova	14.2°N	39.8°E	6054.3	18933	0.47	12.7°N	39.6°E	6053.6
west edge					0.59	14.2°N	37.7°E	6053.4
south edge					0.47	12.7°N	39.6°E	6053.6
Dali Chasma	20°S	170°E	6059.5	10920	0.57	17.2°S	170.0°E	6056.1
(edge of plateau)	6.7°S	221.3°E	6056.0	4997	0.53	6.1°S	221.1°E	6055.1
(edge of plateau)	11.3°N	219.4°E	6054.8	3726	0.61	10.9°N	219.4°E	6054.1
			Impact Craters					
Boleyn	24.5°N	220.0°E	-	1572	0.61	24.5°N	220.0°E	6051.5
Stanton	23.2°S	199.3°E	-	1486	0.66	23.3°S	199.2°E	6051.1
Stuart	30.8°S	20.2°E	-	409	0.69	30.7°S	20.2°E	6051.0
Mead	12.5°N	57.5°E	-	21	0.70	13.1°N	57.6°E	6051.1
			Miscellaneous					
(plains area)	10°N	234°E	6055.4	98780	0.64	9.1°N	229.4°E	6052.1
(unnamed)	20.1°N	187.6°E	6056.2	2563	0.59	20.1°N	187.9°E	6056.0
(plains area)	4.0°N	219.5°E	6052.7	2132	0.65	4.5°N	220.2°E	6051.7
(unnamed)	20.0°S	187.2°E	6054.6	840	0.67	20.1°S	187.2°E	6054.1
(unnamed)	16.4°N	197.7°E	6056.2	732	0.65	16.4°N	197.8°E	6055.5

Table 3.3: Selected dark summit areas.

Location	Latitude	Longitude	Radius (km)	Maximum Emissivity
Ovda	7.0°S	95.7°E	6057.0	0.84
	9.5°S	95.2°E	6057.5	0.86
	6.4°S	90.0°E	6057.4	0.78
Thetis	11.8°S	135.8°E	6057.0	0.81
Ozza	3.8°N	199.6°E	6058.4	0.92
Theia	23.6°N	280.2°E	6057.1	0.86
Sapas	8.8°N	188.0°E	6055.6	0.69
	8.5°N	188.2°E	6055.3	0.70
Tepev	29.6°N	45.5°E	6056.8	0.76
Asteria	24.5°N	264.1°E	6056.0	0.79

SAR images tend to indicate that they are slightly raised relative to the surroundings (recent examination of some of these areas with right-looking SAR images confirms this hypothesis). Similar behavior is observed at the summits of several volcanoes. Altimetry data over such dark areas sometimes shows them as rises and sometimes as depressions; the ambiguity may be due to the deviations from the scattering model used to determine topography caused by an area of low reflectivity immediately next to one of high reflectivity. In some cases the depression may actually exist; further study and stereographic SAR images may help settle this question. Table 3.3 contains a summary of the resolved dark summit areas and their emissivity characteristics. (Several other dark areas at high elevations in the highlands and at the summits of smaller volcanoes are visible in SAR images but were not resolved by the Magellan radiometer; these are not listed in the table.)

It is interesting to notice that some of the dark areas in Ovda are entirely continuous, while others are in various stages of breaking up. This may represent an evolutionary process. The less broken dark areas seem to occur in ridged terrain, while the more broken occur in tessera; this may indicate the progression of folding and erosion that creates tessera from undeformed material, possibly of the sort found in the lava flow described in the following paragraph.

The largest dark area in Ovda is at 96°E, 7°S. This area is associated with the only

Figure 3-2: (color plate) SAR image of Ovda Regio, overlain (in false color) with topography and emissivity. Ovda Regio accounts for approximately half the planetary area having emissivity below 0.7. Dark stripes result from missing data.

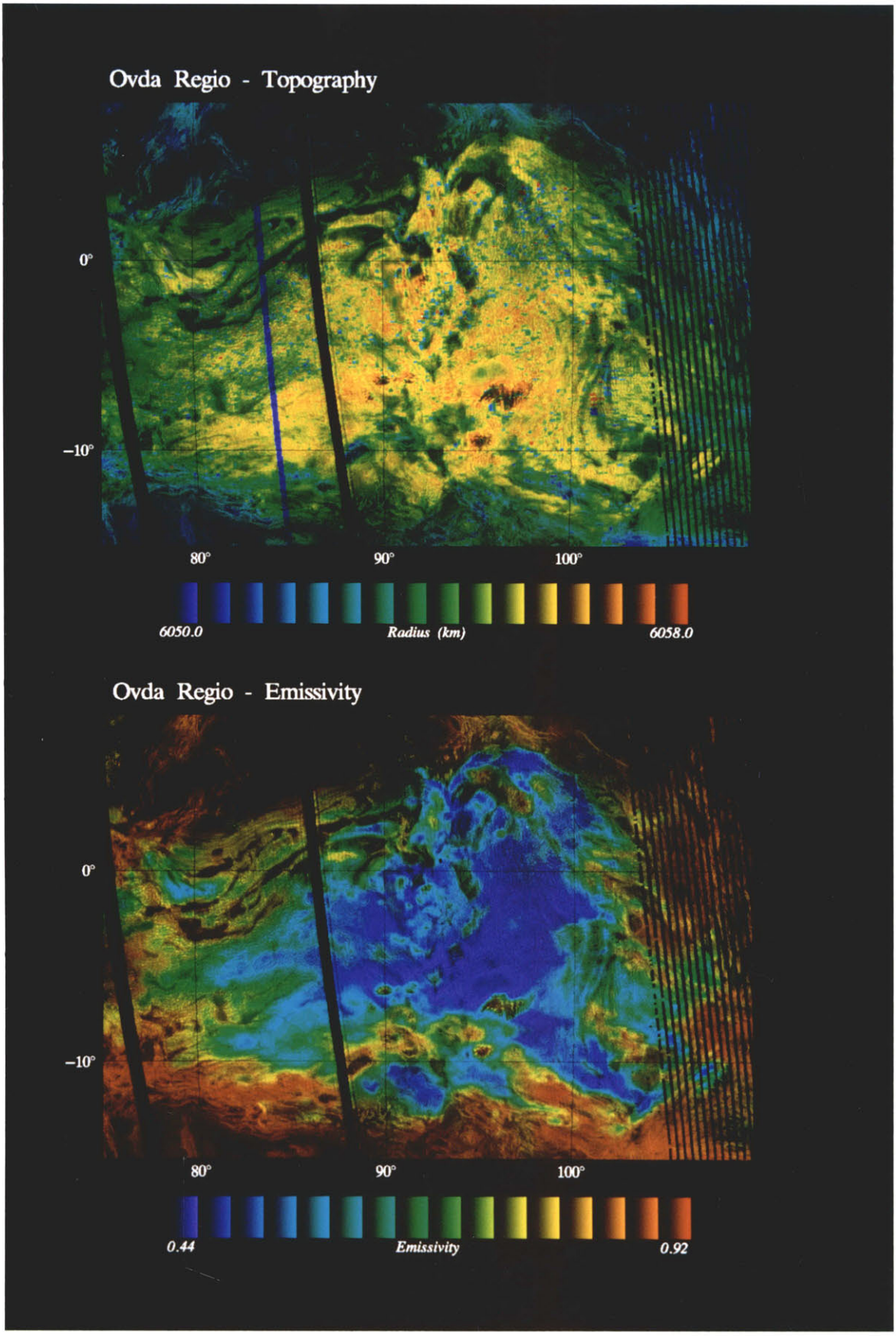
Ovda Regio - Topography
0°
−10°
80°
90°
100°
6050.0
Radius (km)
6058.0
Ovda Regio - Emissivity
0°
−10°
80°
90°
100°
0.44
Emissivity
0.92

bright unfolded area in Ovda, a lava flow about 300 km by 150 km across, just to the north of the dark area (figure 3-3). In most places where the two touch, the darker flow appears to overlie the lighter; in a few places they seem to merge gradually. The vent or fissure from which either type of lava may have flowed is not apparent. The darker flow is more fractured, and in the southwest is discontiguous in places. The light flow (of which the majority seems to have been simultaneously emplaced) has a sharp, though billowy (festooned), boundary with the surrounding terrain; the bright west edges (facing the radar) indicate that the flow is thick. The flow is transversed by several wide (2–3 km) fractures. There are large numbers of small "ripples" of about 1 km wavelength. These ripples are locally parallel but are oriented in different directions across the entire flow.

The surface of the flow is not level (as we deduce it was at the time of emplacement), but rather is depressed in the center. There are two local minima of about 6054.6 km (compared to near 6056.0 km at the edges of the flow). The western minimum is associated with a local rise in emissivity; while the emissivity at the nearby edges of the flow is as low as 0.35, the maximum in this depression is 0.50. The eastern topographic minimum corresponds to a local bend in the emissivity contours, in a direction consistent with the idea that the emissivity of the surface in the depression is lower than it would have been if at higher elevation.

Despite the correlation of higher emissivity with topographic lows in the festooned flow, the relationship outside the depressions is not at all clear. The lowest emissivity in all of Ovda (0.26) occurs in the eastern part of this same lava flow, just to the southeast of the eastern depression, at radius 6055.4 km. The highest elevations in the flow, 6056.3 km, are located along its eastern edge; the emissivity there is about 0.34. This behavior is puzzling; we presently have no explanation for why the emissivity minimum occurs where it does.

Thetis Regio and Maxwell Montes are quite similar to Ovda Regio. Thetis is a large area of tessera terrain, interwoven with areas of smoother, darker material. The lowest emissivities are 0.36 in the northeast, 0.35 in the north central, and 0.43 in the

Figure 3-3: (color plate) Portion of a SAR image of Ovda Regio, showing a festooned flow of high-viscosity magma. The image is overlain (in false color) with topography and emissivity. The lowest emissivity measured by Magellan during the first eight months of mapping (0.26) lies in the eastern part of this flow. Note the topographic low in the western interior that corresponds to a local rise in emissivity. Also note the radar-dark area to the south of the flow, which is higher in elevation than the main flow surface but has a value of emissivity rising to 0.84.

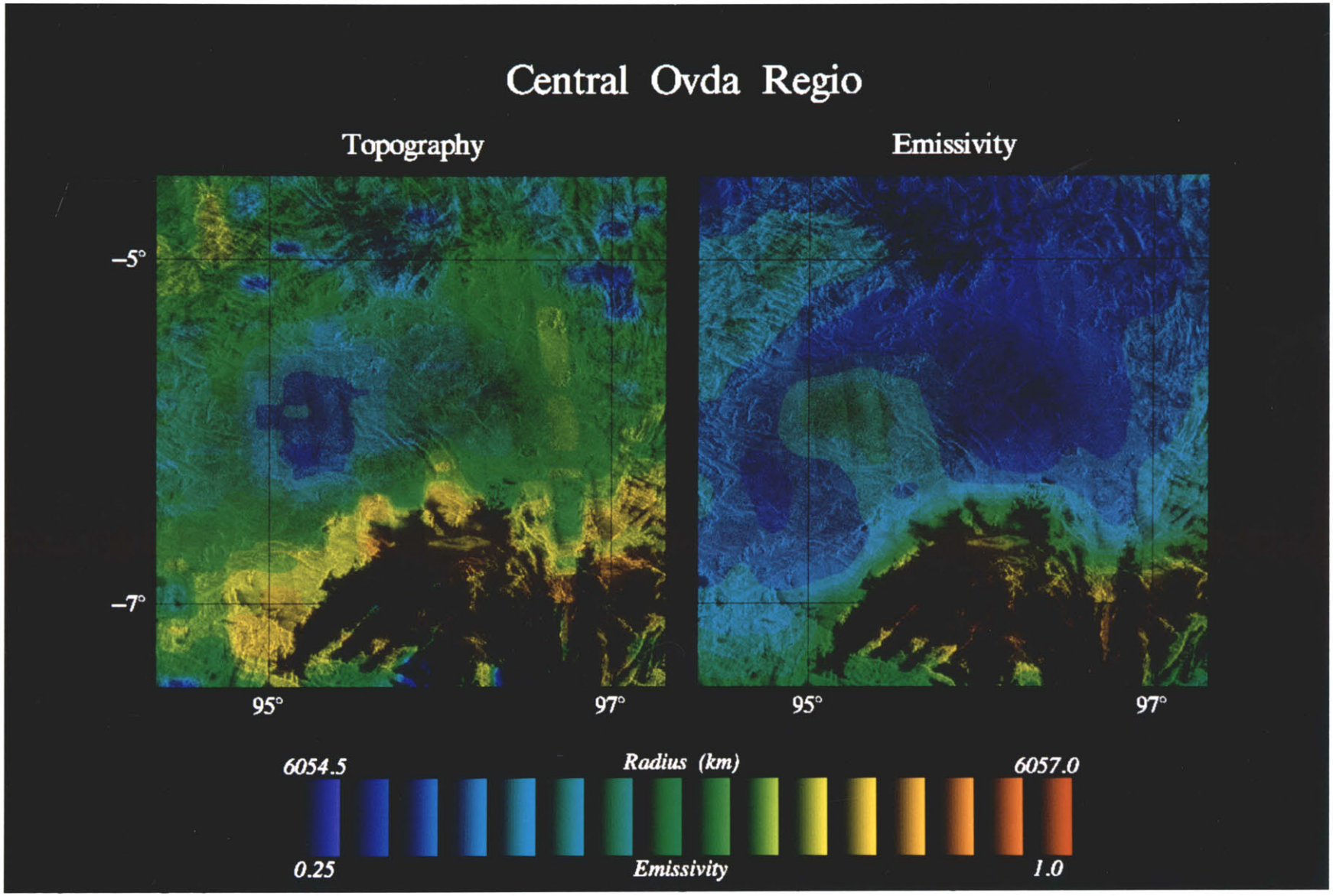
Central Ovda Regio
Topography
Emissivity
–5°
–7°
95°
97°
95°
97°
6054.5
Radius (km)
6057.0
0.25
Emissivity
1.0

south central region; these values are attained at planetary radii in the range 6055.5–6056 km. The south central region is generally as high as the other two regions, but has a lower average emissivity. There are one or two high dark areas similar to those found in Ovda. One interesting feature is an impact crater located in the north central region at 128°E, 6°S; the planetary radius at this point dips to below 6051.5 km, and the emissivity rises to over 0.75.

The highest altitudes on the surface of Venus are located within Maxwell Montes; most of Maxwell is at altitudes above 6058 km. The highest points, over 6062 km radius, are located along the steep cliffs at the western edge; most of this western edge is bright in backscatter and low in emissivity (minimum 0.38). The western half of Maxwell consists mainly of parallel ridges running in a generally north-south direction. These ridges contain an intermixture of bright and dark surfaces; this may in part be due to local slopes directed away from the antenna, however it appears that there is some intrinsically dark material here. Emissivities in this area are about 0.55–0.60. In the eastern half of Maxwell we find the crater Cleopatra, where the radius falls to 6055.1 km and the emissivity rises to 0.65. The rest of this half of Maxwell is comprised of tessera terrain, which merges into the large area of tessera (Fortuna Tessera) to the east. The eastern part of Maxwell is remarkable because while the morphology of the surface does not change across the boundary, the drop in altitude is accompanied by a rapid increase in the surface emissivity and a rapid decrease in the backscatter intensity.

Klose et al. point out that during the left-looking cycle 1 observations, the west half of Maxwell slopes toward the Magellan antenna by about 10° from horizontal, while the east side slopes away by about 5°; these slopes change the radiometer's incidence angle, and in horizontal polarization, the west side should show slightly lower emissivities than the east. (This expectation is due to the properties of the Fresnel emission curve—see section 4.2.4.) Their separation of the data from the east and west shows that this is indeed the case.

3.2.2 Shield Volcanoes

Figure 3-4 compares the topography and emissivity of Ozza Mons. Ozza is fairly representative of the volcanoes we have examined, although like most of the others it has its peculiarities. The summit of Ozza is a broad (80 km wide), roughly oval area of dark material. The western part of this summit area has been measured by the Magellan altimeter to lie at 6057.5 to 6058.0 km. Topographic data also show elevations as low as 6055 km in this dark area, but there is no evidence for a depression of this depth in the SAR images; we suspect the problem to be similar to that encountered in Ovda Regio. The summit plain contains some fracture and collapse features, and on the northwest side there are small cones which have erupted lava of medium backscatter brightness. An extensive area of small cones of the same type lies just to the northwest of the summit area. Many of these cones have a dark rim around the central vent.

Numerous flows of mainly medium and bright lava extend hundreds of kilometers to the north, east, and south. Most of the lava flows from Ozza have apparently flooded pre-existing systems of fracture, although in several places, especially to the north, fractures occur in the lava flows themselves. These fractures lie along the rift zone on which Ozza is situated. To the southeast of the summit the lava flows form a large polygonal plateau, with steep boundaries on the southwest and south edges.

Emissivity rises as high as 0.92 on the dark summit area. In the lava flows, minima of emissivities are 0.44 to 0.47; these minima all lie 100 km or more away from the summit. There seems to be some correlation of emissivity with certain lava units. For example, some of the medium backscatter flows to the southeast have lower emissivities than brighter flows in the same area. To the north, the lowest emissivities are in a high backscatter lava unit. Unfortunately, the low resolution of the radiometry data makes a more detailed analysis along these lines difficult.

The lowest value of emissivity in this region, 0.34, lies in an area about 75 km west of the summit of Ozza. The minimum does not appear to be associated with any identifiable lava flow, or for that matter with any feature seen in the SAR image or

Figure 3-4: (color plate) SAR image of Ozza Mons, overlain (in false color) with topography and emissivity.

Figure 3-5: (color plate) SAR image of Maat Mons, overlain (in false color) with topography and emissivity.

Ozza Mons

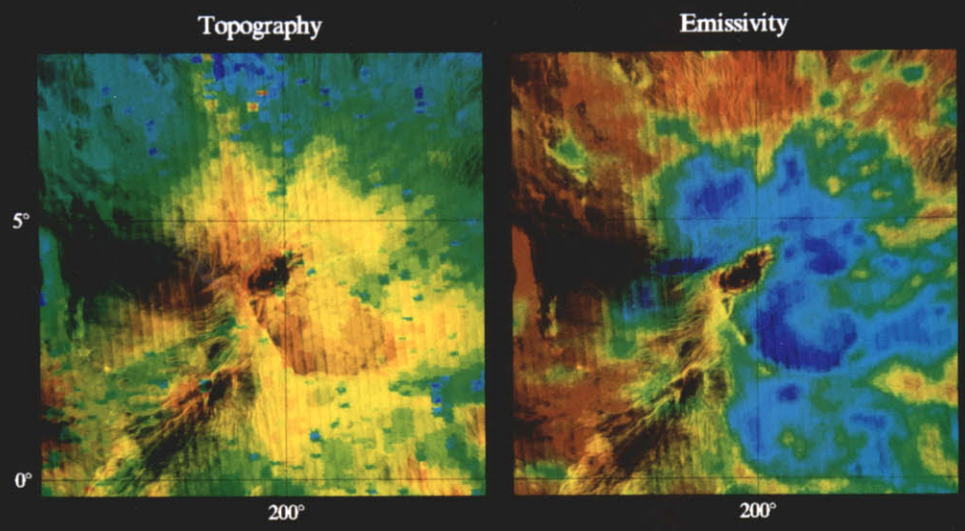

Maat Mons

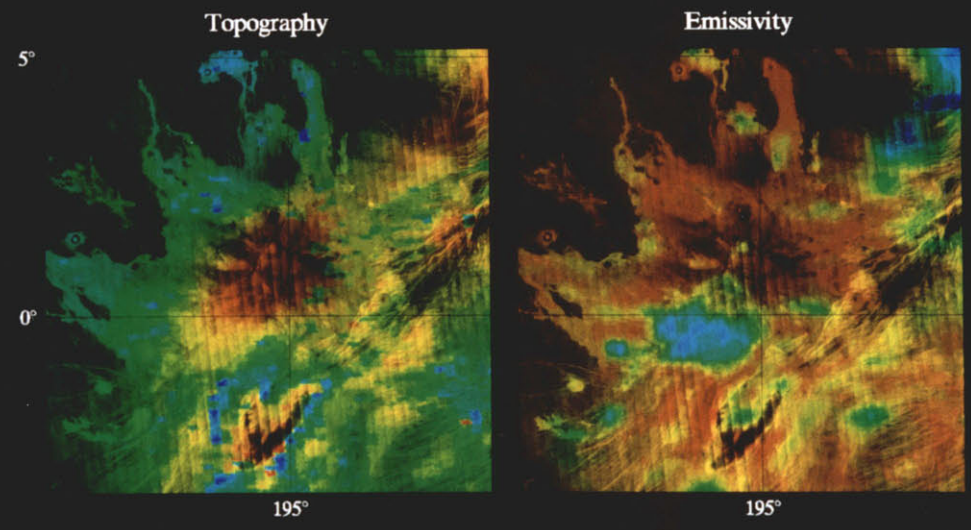

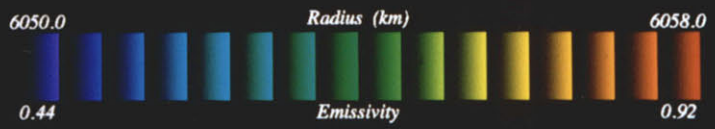

topographic map. The area is relatively low in backscatter; it is cut by a few north-south fracture lines, but is otherwise unremarkable. The elevation at this minimum is 6056.5 km. This feature was also observed to be highly reflective by the Magellan altimeter.

Although each is peculiar in its geology, most other members of this group have emissivity characteristics similar to those of Ozza. The emissivity patterns are not generally symmetric, and the lowest emissivities are found at a distance from the central point. Most have dark summits areas with high emissivities.

Several volcanoes of height comparable to those listed in table 3.2 show much less reduction in emissivity. The volcano at 214.7°E, 46.5°S reaches an elevation of 6055.2 km, but the emissivity falls to only 0.74; possibly this results from incomplete resolution due to the large radiometer footprint size at this latitude. However, Sif Mons, at latitude 22°N, is 6054.6 km high, but has the same minimum emissivity of 0.74. The major exception to the general rule that high volcanoes show lowered emissivities is Maat Mons (figure 3-5). Most of the summit of Maat, which rises to over 6060 km, is covered with dark flows having emissivities between 0.8 and 0.9. On the near flanks, the same flows have emissivity as high as 0.98. Only in a single bright lava unit on the southern flanks does the emissivity fall to 0.54, a value consistent with what is observed on other tall volcanoes.

3.2.3 Rifted Volcanoes

Some of the large volcanoes, such as Ozza and Theia, lie atop extensive rift systems. From the frequency of coincidence of large volcanoes and rift systems, it seems likely that the two are manifestations of the same process. It is difficult to say which appears first, and some evidence indicates that volcanism and extension may occur concurrently for some period [67], but in any case it is evident that the rifting process may continue after the formation of the volcano, and may eventually disrupt it entirely. Early stages of volcano rifting are seen in Ozza and Theia. The volcano at 285.1°E, 17.9°S is in a more advanced stage of disruption. Figure 3-6 shows a portion of the south part of Devana Chasma, where one or possibly two volcanoes

have been rifted apart. The main identifying feature of a rifted volcano is the system of lava flows outside the rift valley, apparently emanating from a point inside the valley. The lowest emissivities around rifted volcanoes occur close to the central point, just outside the rift valley; emissivities in the valley are usually much higher. The distribution and the minima observed are fairly consistent with what is observed for unrifted volcanoes of similar size.

Included in this category is Rhea Mons, which lies along Devana Chasma, to the north of Theia Mons. While long thought to be a large shield volcano similar to Theia and others, Magellan images indicate that Rhea is an area of tessera terrain, with smooth deposits of volcanic origin near the summit [67]. However, we find the emissivity characteristics of Rhea to be similar to those of volcanoes, rather than to those of highland areas or uplifted ridges, and thus include it in the present category. Rhea reaches a topographic high of 6058.6 km; emissivities at the summit are approximately 0.63, and rise to over 0.7 in the smooth volcanic deposits. Emissivities of points on the north and east flanks fall as low as 0.61 and 0.58, respectively, while about 200 km to the south (and outside the main body of tessera) is a minimum of 0.52.

3.2.4 Small Volcanoes

Included in this category are several volcanic features of relatively small area. Over half of the members of this category are novae. A nova has been postulated to be the surface manifestation of the arrival of a rising quasi-spherical plume of hot mantle material at the base of the lithosphere; the buoyancy of the plume upwarps the surface and creates radial extensional faults. Subsequently, the plume head flattens against the overlying crust, spreads radially, and creates a more plateau-like topography, eventually developing into a corona [67]. The novae we have examined in conjunction with low surface emissivity are generally located inside of polygonal plateau-like areas, sometimes raised in the center and sometimes depressed; the plateau edges are usually raised relative to the surrounding terrain. The low emissivities associated with novae

Figure 3-6: (color plate) SAR image of rifted volcano on Devana Chasma at 2°S, 288°E, topography and emissivity.

Figure 3-7: (color plate) SAR image of two novae and plateaus, topography and emissivity.

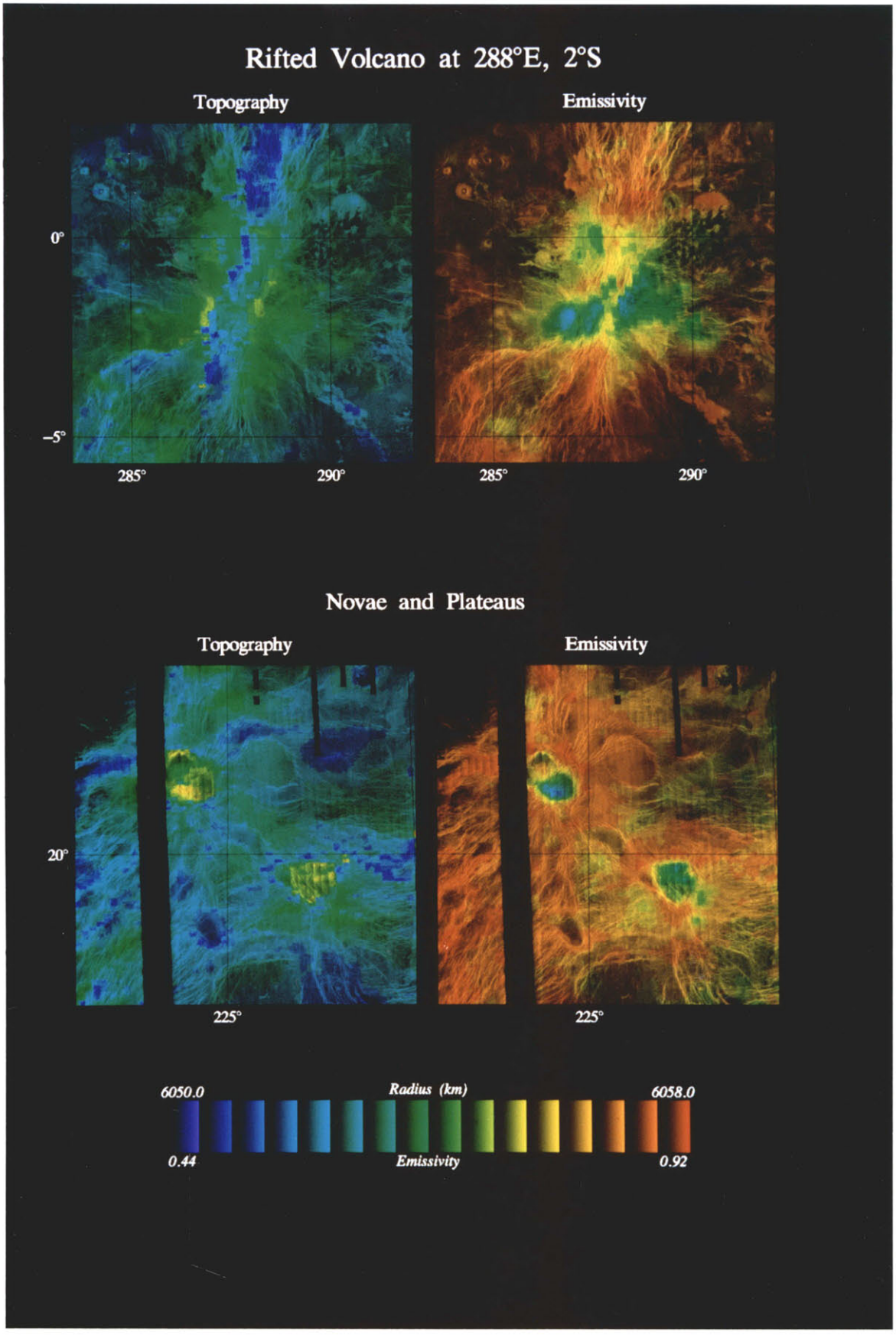
Rifted Volcano at 288°E, 2°S
Topography
Emissivity
0°
−5°
285°
290°
285°
290°
Novae and Plateaus
Topography
Emissivity
20°
225°
225°
6050.0
Radius (km)
6058.0
0.44
Emissivity
0.92

are usually found on or near the nova itself, but in other cases are located at the raised, presumably uplifted, edges of the associated polygonal plateau or corona. We have placed areas of the latter type into the ridge category (below). Although there are numerous novae across the surface of Venus, those of low height do not display the low emissivity phenomenon.

Figure 3-7 shows two nova/plateau combinations. In the northwestern of these two structures, the nova rises to 6055.7 km; the minimum emissivity of 0.55 is found 30 km to the east of the nova center, where the measured radius is 6055.3 km. This plateau dips in its center, but the north edge rises to 6055.5 km. The emissivity on the north edge, though, is 0.80. In the southeastern structure, the emissivity falls to 0.62 at the north end of the plateau, and to 0.64 in the bright area just to the east of the nova center.

Two other structures of interest are located at 34.4°E, 0.7°N and at 45.5°E, 2.6°N. The first of these is the source of extensive light and dark lava flows; it is a bright structure with a hint of the radial fracturing characteristic of novae. This object has a peak elevation of 6054.9 km; the emissivity near the top falls as low as 0.43. This may be a nova in an early active stage. The second object is of similar size and is similarly bright, but with less lava effusion and no radial fracturing. This object rises to 6053.9 km, and has a low emissivity of 0.52. It may be an earlier version of the first object, that is, a young (and possibly active) nova.

Except for the volcano in Asteria Regio at 24.2°N, 263.8°E, which is situated on a rift system and displays some of the morphological and emissive characteristics of rifted volcanoes, the remaining members of this category are morphologically dissimilar to the previously described volcanic structures. Because of their small size, and the limited resolution of the Magellan radiometer, the relationship between emissivity and geology in these cases is more difficult to decipher.

3.2.5 Ridges

This category includes several areas on the surface which we interpret to have been uplifted to their present altitude by tectonic processes; the majority of members of

the category are linear elevated features (thus "ridge").

The most extensive feature in this class is not linear at all. The western margin of Hestia Rupes, just to the east of Ovda Regio, is a triangular region surrounded by a chasm to the north, a fractured area of low altitude to the east, and a region of mottled plains to the southwest. The surface in this area is mainly devoid of lava flows or other features (exceptions being a small corona and another circular feature of unknown type), and is of medium backscatter brightness. An emissivity minimum of 0.48, at altitude 6055.5 km, is located between two topographic highs of 6055.6 km, located 20 km to the east and 40 km to the west. A second emissivity minimum of 0.50 lies further to the south.

Pavlova is a corona of diameter 400 km, with a raised rim and central depression. A well-developed nova rises to 6054.4 km in the western part of the corona. The rim is as high as 6053.8 km in the south, and is cut at right angles by closely-spaced fractures, more numerous to the west. Some of these fractures extend from the nova, but most start and end at opposite sides of the rim (possibly the extensions of these fractures were buried by lava flows). Emissivity on the south rim of Pavlova falls to 0.47; the minimum is not coincident with the topographic high. Near and on the nova itself, the emissivity falls to as low as 0.78, but also rises to 0.92.

The most intriguing low-emissivity ridge is the south rim of Dali Chasma. Figure 3-8 shows a part of the Chasmata area of Aphrodite Terra known (at least locally) as the "Eye of Dali." Dali Chasma runs east to west along the top of the picture. The ridge along the north edge of the eye rises as high as 6057.2 km, and is at 6056.5 km and higher for over 250 km along its length. The minimum emissivity is 0.58 to 0.60 along this entire length.

It is interesting that the lowest emissivity is not centered around the top of the ridge, but falls consistently 10–20 km to the south of the ridge, away from the steep dropoff and toward the interior of the "eye." The low emissivities along other ridges in the area, although not as low, also tend to fall on the interior side of the ridge, where the slope is less steep. This behavior is not peculiar to the Dali area. Features

Figure 3-8: (color plate) SAR image of Dali Chasma area, overlain (in false color) with topography and emissivity.

Figure 3-9: (color plate) SAR image of Crater Stanton, overlain (in false color) with topography and emissivity.

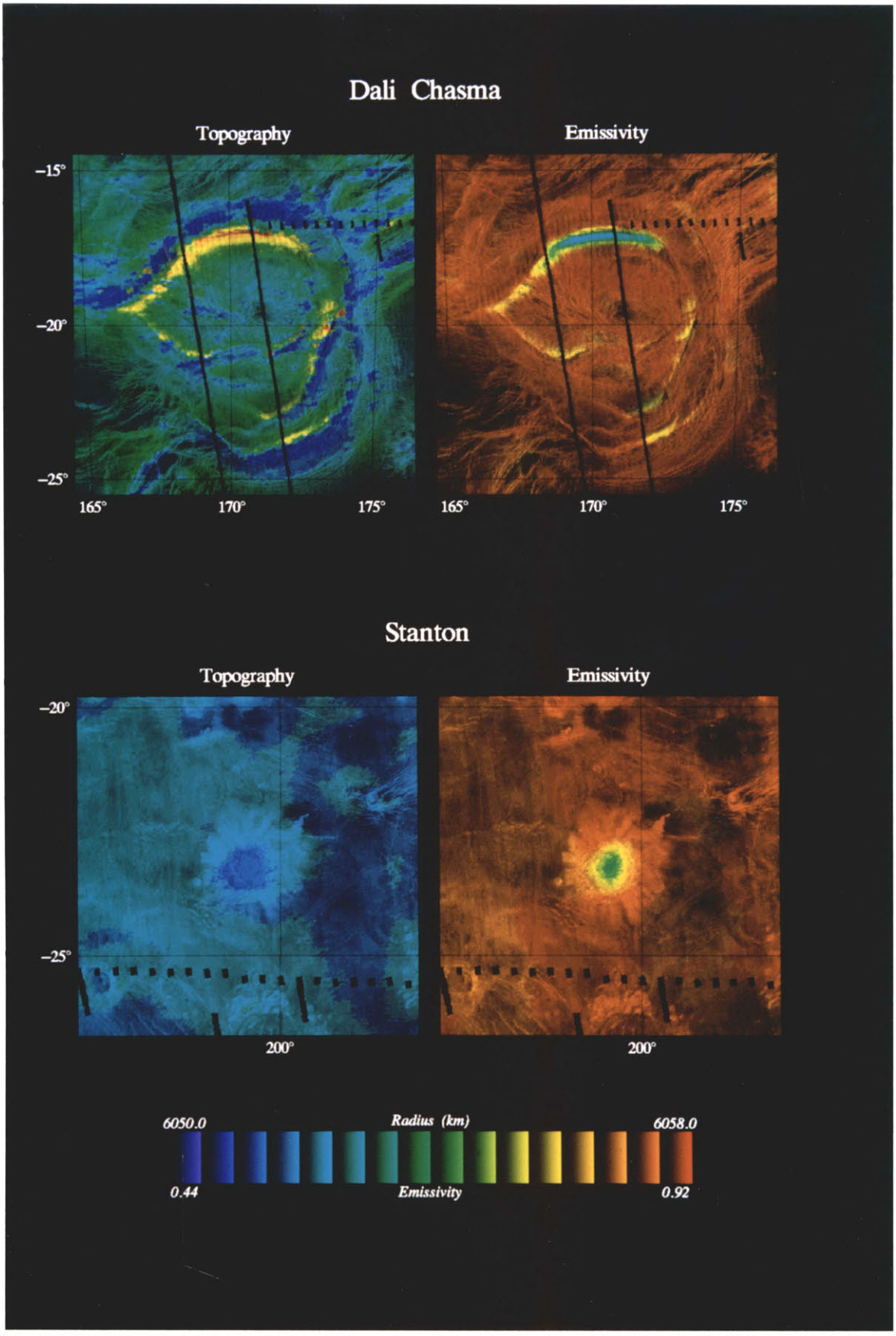
Dali Chasma
Topography
Emissivity
−15°
−20°
−25°
165°
170°
175°
165°
170°
175°
Stanton
Topography
Emissivity
−20°
−25°
200°
200°
6050.0
Radius (km)
6058.0
0.44
Emissivity
0.92

at 6.7°S, 221.3°E and 11.3°N, 219.4°E, which are the edges of polygonal plateaus associated with novae, also display this characteristic. In the first of these, the line of lowest emissivities occurs about 10 km to the south (toward the plateau interior) of the line of maximum elevations (which runs west to east); in the second, the line of lowest emissivities lies about 10 km to the east (also toward the plateau interior) of the line of maximum elevations (which runs south to north). This pervasive distance of 10 km is of the order of the radiometer and altimeter footprint sizes; it is difficult at the moment to determine with any certainty whether this trend actually exists or is caused by some factor associated with viewing geometry or data reduction.

3.2.6 Impact Craters

Figure 3-9 displays the topography and emissivity structures of crater Stanton. We located only four craters whose emissivity fell to 0.70 or below, not including those which lie in larger regions of low emissivity. All four have bright interiors; three of the four also have bright ejecta (the exception being Mead). The diameters of the four are 60 km or greater. All are located in areas where the average planetary radius is 6051 to 6052 km. The pattern of emissivity is always fairly symmetric, with the minimum value located near the center of the crater. Other craters, as well as the paraboloid streaks associated with some craters [1], are associated with depressed emissivities, although none were low enough to be included in our survey. For example, Boulanger (26.5°S, 99.3°E, formerly known as Avila), a 70 km diameter double-ringed crater with a bright interior and ejecta, has a minimum emissivity of 0.76.

3.2.7 Miscellaneous

There are several areas in our survey whose nature was either not obvious, or who did not fit into any of the above categories. The most important of these is an extensive plains area located around 10°N, 234°E. This area contains coronae and related activity, small volcanic domes, and zones of fracture. Although the surface area whose emissivity falls below 0.70 is greater than that of most volcanoes, the lowest

emissivity is only 0.64. The low emissivities tend to be associated with medium-dark lava flows which are relatively unfractured, although the correlation is not precise. Another similar, but much smaller, plains area at 4.0°N, 219.5°E has a minimum emissivity of 0.65. In both of these cases the low emissivities lie at altitudes of about 6052 km.

3.3 Critical Radius

The global relationship between emissivity and altitude is shown in figure 3-10. This figure shows clearly the association of low emissivity surfaces and high elevations. It is also clear that emissivity does not drop linearly with altitude, but rather is relatively constant up to a certain altitude, at which it begins to drop rapidly with height. The altitude at which the emissivity begins to drop is called the "critical altitude" [44], or equivalently the "critical radius."

It must be remembered that above the mean radius of about 6051 km, the total planetary area in a given altitude range decreases with height, so the upper part of figure 3-10 is dominated by a relatively small portion of the planet. The leftward bend (toward lower emissivity) between altitudes 6054 km and 6056 km is controlled by the combination of most of the low-emissivity features described in the last section. The rightward bend (toward higher emissivity) observed in the range 6056–6058 km is a result of the net effect of dark areas at high altitudes in Ovda Regio and Thetis Regio, dark areas at the summits of Ozza Mons and Theia Mons, and higher emissivity areas on Maat Mons and in Freyja and Akna Montes. Above 6058 km, the curve is dominated by data from Maxwell Montes.

Scatter plots of radius vs. emissivity for several low emissivity areas are presented by Klose et al. [44] Figures 3-11 and 3-12 are examples of plots of this type. Klose et al. use these plots to determine the critical altitudes at which the emissivity drops steeply. Their results are listed in table 3.4. A few interesting details of the regions which are difficult to see by other methods are visible in the scatter plots. For example,

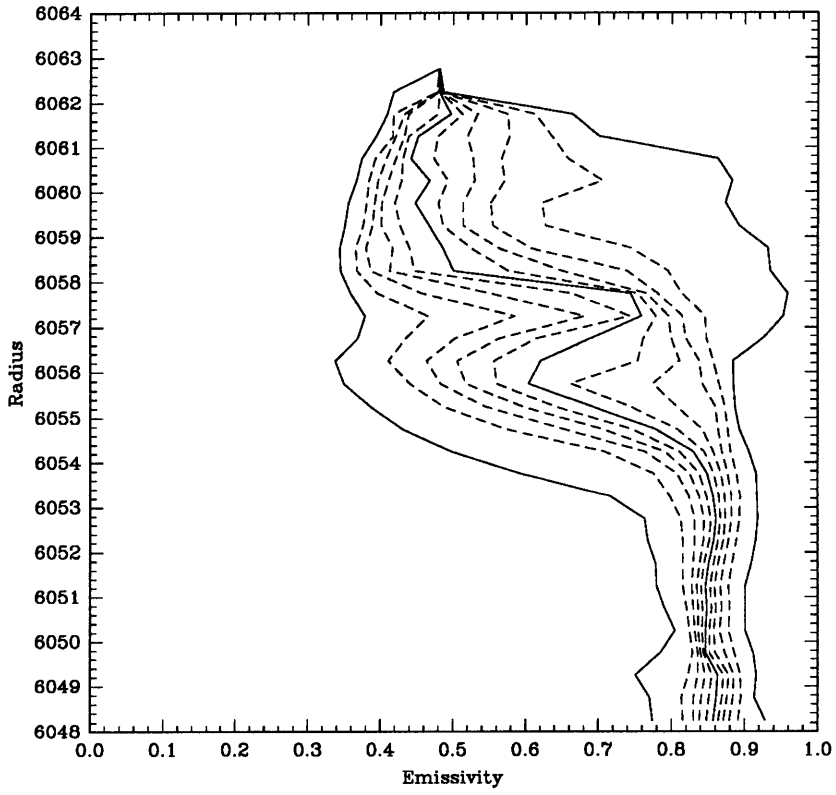

Figure 3-10: Altitude vs. emissivity on Venus, from Magellan cycle 1 results. The leftmost (solid) curve shows the emissivity of the first percentile of data at a given altitude (that is, 99% of the area at the given altitude has an emissivity higher than this value); the rightmost curve shows the 99th percentile. Intermediate (dotted) lines are 10% increments; the central (solid) line depicts the median. Data were sampled in 0.5km intervals.

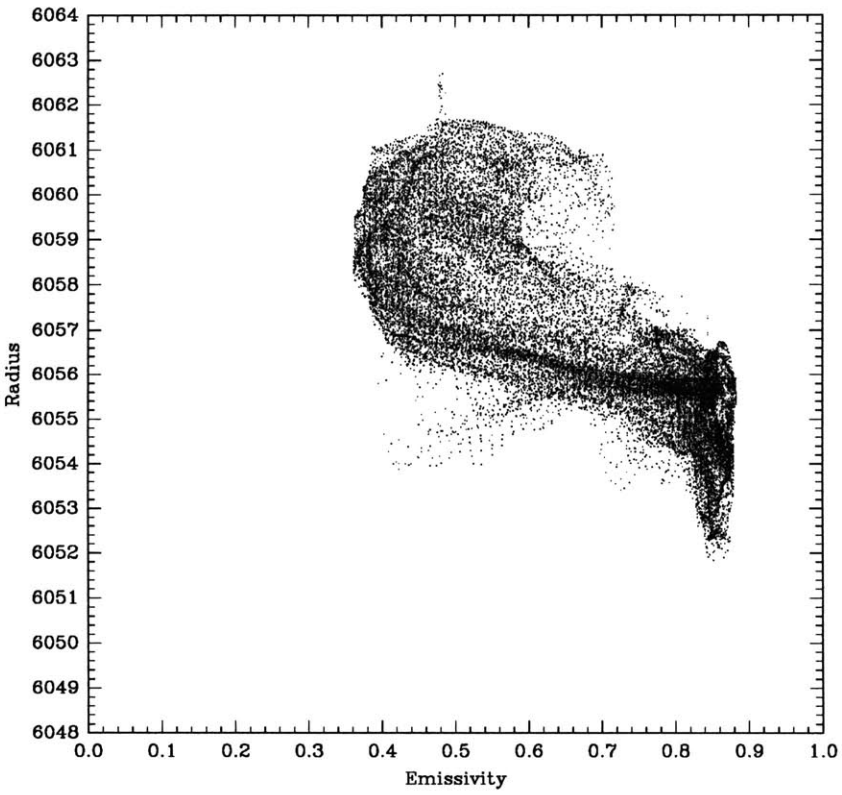

Figure 3-11: Scatter plot of altitude vs. emissivity in Maxwell Montes. Each point represents an equal area on the surface. Data are taken from an area on the surface with corners (69.4°N,350.5°E), (69.4°N,15.4°E), (60.6°N,354.0°E), (60.6°N,11.9°E).

Klose et al. point out the "wing" of low-emissivity data points descending below the critical altitude, associated with a steep cliff on the western scarp of Maxwell. This is probably due to the large radiometer footprint size causing misregistration between altimetry and radiometry data; it might also be due to landslides carrying low-emissivity material down to lower elevations.

We have determined critical radii by two different methods. Both methods are based on an examination of the median value of emissivity as a function of altitude; in both methods we assume that the emissivity at low altitudes is constant, then decreases rapidly over a short altitude span. The behavior at high altitudes is not important. Features which do not exhibit this general behavior, such as the craters,

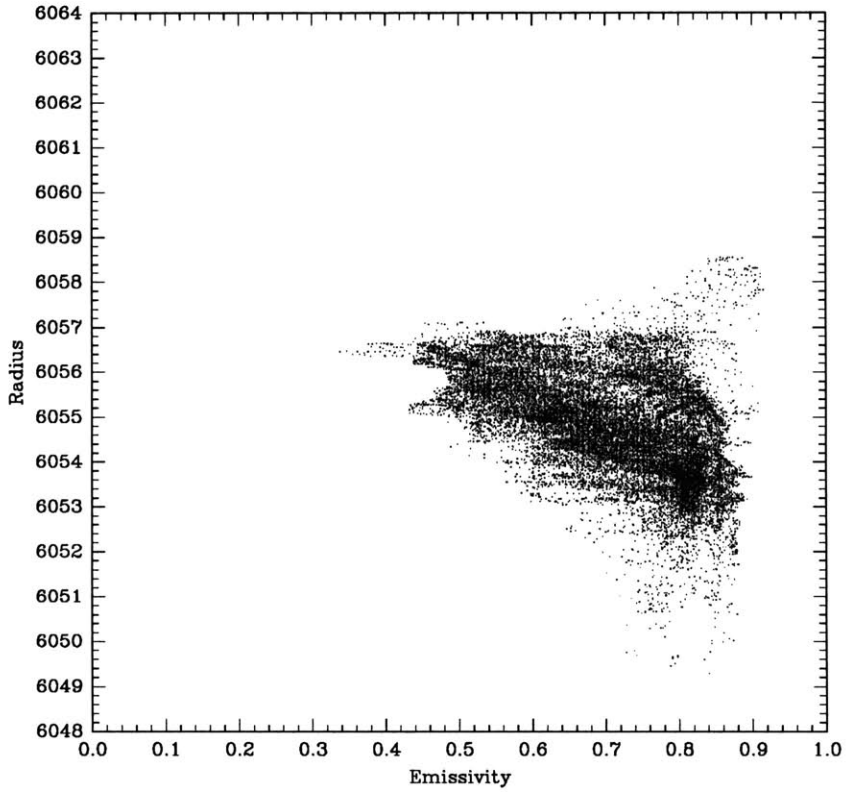

Figure 3-12: Scatter plot of altitude vs. emissivity on Ozza Mons. Each point represents an equal area on the surface. Data are taken from an area on the surface bounded by latitudes 1.7°S, 7.1°N and longitudes 197.1°E, 205.9°E.

Table 3.4: Critical radius of various regions, reported by Klose et al. [44]. Note that Beta Regio includes both Rhea Mons and Theia Mons, and that Atla Regio includes both Maat Mons and Ozza Mons.

Region	Critical Radius (km)
Maxwell Montes	6055.75
Freyja Montes	6055.42
Danu Montes	6054.00
Gula Mons	6053.90
Ovda Regio	6054.10
Thetis Regio	6054.33
Dali Chasma	6054.80
Atla Regio	6054.50
Maat Mons	6056.60
Sapas Mons	6053.49
Beta Regio	6053.50

plains areas, and Maat Mons, are not considered in this part of the survey. The first method simply defines the critical radius as the lowest altitude at which the median emissivity fall below 0.70. In the second method, we fit a set of connected line segments to the data. The first line segment rises vertically from low altitudes to the altitude defined as the critical radius, and represents the relatively constant average emissivity at low altitudes. The second segment rises to the left, and represents the fall in emissivity with altitude just above the critical radius. The third segment rises to the right, and the fourth rises vertically; these are used to fit the high-altitude emissivity behaviors of various features, and their main function is to prevent the upper altitude data from interfering with the fit to the low altitude data.

Table 3.5 presents our measurements of the critical radius of various low emissivity features. Included in the table are data for Akna and Freyja Montes. The measured emissivities in these mountain ranges do not fall below 0.7, and thus they have not been considered so far. However, these are narrow mountain ranges located at high latitudes, and are not fully resolved by the Magellan radiometer; based on their high altitudes and bright SAR backscatter, it seems likely that the actual emissivities in these ranges are much lower than those measured. The altitude vs. emissivity plot for the two areas does show a distinct bend. A fourth highland area, located in the far southwest of Aphrodite Terra, has also been incorporated. Information in the table includes the feature name and location, the altitude at which the median emissivity falls below 0.7, and the two interesting parameters from the line segment fit—z_0, the altitude at which emissivity begins to fall, and de/dz, the rate at which emissivity changes with altitude in the segment above z_0. The value of z_0 is more representative of the altitude at which the emissive properties of the surface begin to change than is the altitude at which the median falls through 0.7; throughout the rest of this work, we shall refer to values of z_0 as the critical radius.

A few minor trends are apparent. The three areas in the far north (Maxwell, Akna, and Freyja) are the only areas whose critical radius is above 6054.5 km; this is consistent with the fact that Lakshmi Planum, which is bordered by all three mountain ranges and lies at a planetary radius in the range 6055–6056 km, does not

Table 3.5: Critical radius of selected features (see text). z_0 is the best estimate of critical radius.

Name or Description	Location Lat	Lon	Critical Radius Median ≤ 0.70	Line Segment Fit z_0	de/dz
		Highlands			
Ovda Regio	3°S	90°E	6054.7	6054.0	-0.138
Thetis Regio	8°S	127°E	6054.8	6053.7	-0.228
Maxwell Montes	65°N	3°E	6056.4	6055.5	-0.158
(SW Aphrodite)	10°S	63°E	-	6054.0	-0.290
		Shield Volcanoes			
Ozza Mons	3.8°N	199.3°E	6054.9	6053.5	-0.089
Theia Mons	23.6°N	280.2°E	6055.0	6054.1	-0.120
Sapas Mons	8.9°N	188.0°E	6053.7	6053.4	-0.392
Tepev Mons	29.6°N	45.0°E	6055.1	6053.3	-0.103
Sekmet Mons	44.3°N	240.4°E	6053.2	6052.7	-0.193
Gula Mons	21.8°N	358.5°E	6054.6	6053.3	-0.096
		Rifted Volcanoes			
Rhea Mons	32.4°N	282.6°E	6055.6	6054.2	-0.148
(unnamed)	2.0°S	288.0°E	6054.6	6053.3	-0.103
(unnamed)	17.9°S	285.1°E	6054.0	6053.3	-0.229
(unnamed)	17.1°N	194.2°E	-	6054.4	-0.075
		Small Volcanoes			
(nova)	0.7°N	34.4°E	6053.0	6052.3	-0.268
(small volcano)	24.2°N	263.8°E	6054.9	6051.6	-0.038
(nova)	9.0°N	219.1°E	-	6053.5	-0.135
(nova)	15.3°N	221.2°E	-	6053.5	-0.135
(small volcano)	6.2°S	299.3°E	6054.1	6053.5	-0.175
(nova)	2.6°N	45.5°E	6053.3	6052.7	-0.328
(nova)	22.2°N	223.7°E	6055.2	6053.9	-0.145
(nova)	19.4°N	227.4°E	6054.8	6052.8	-0.067
(nova)	1.7°S	215.0°E	6054.6	6053.7	-0.123
(nova)	11.1°N	14.3°E	6053.5	6053.1	-0.148
(small volcano)	5.6°S	217.1°E	6055.2	6053.1	-0.086
(small volcano)	2.6°N	301.5°E	6053.6	6053.1	-0.196
(unnamed)	46.5°S	214.7°E	-	6053.5	-0.061
(unnamed)	8.8°S	305.3°E	-	6052.7	-0.085
		Ridges			
Hestia Rupes	2.3°N	73.3°E	6054.8	6054.3	-0.156
Pavlova	14.2°N	39.8°E	6053.3	6053.1	-0.436
Dali Chasma	20°S	170°E	6056.1	6054.4	-0.151
(edge of plateau)	6.7°S	221.3°E	6054.9	6053.3	-0.191
(edge of plateau)	11.3°N	219.4°E	-	6053.5	-0.135
Akna Montes	68°N	316°E	-	6054.7	-0.051
North Devana Chasma	18.8°N	281.8°E	6055.1	6052.9	-0.084
Freyja Montes	74°N	333°E	-	6056.0	-0.054

exhibit the low emissivity phenomenon. (It is also of interest to note that models of the thermal structure of the atmosphere by Seiff [65] predict that the near-surface atmospheric temperature at a given altitude is about 5K–10K higher at high latitudes than it is near the equator.) The critical radii of most other large features lie in the range 6053.3–6054.2 km; the critical radii of smaller features usually lie in the range 6052.7–6053.5 km. The rate at which emissivity falls with altitude above the critical radius varies markedly from feature to feature, from lows near 0.05 km^{-1} to a high of over 0.4 km^{-1}; except for Akna and Freyja Montes, where we would expect this value to be low, there is no obvious pattern.

A fit to the median of the global data (see figure 3-10) gives a critical radius of 6054.4 km, and a rate of decrease of emissivity with altitude above the critical radius of 0.15 km^{-1}. The higher global value of critical radius is caused by various higher emissivity areas at altitudes 6053.0–6054.5 km.

3.4 Summary of Results

The major findings of our survey are as follows:

- Approximately 1.5% of the surface of Venus has an emissivity of 0.70 or less. In places, emissivities fall to as low as about 0.3.
- The low emissivity phenomenon occurs in highlands, on volcanoes, and on uplifted ridges. Surfaces which are apparently geologically similar, but do not lie at high elevation, do not exhibit the phenomenon.
- A relatively sharp altitude boundary separates the low emissivity phenomena at high altitudes from the "normal" emissivity behavior at low altitudes. The change in behavior occurs at a planetary radius of about 6054 km.

In addition, the following observations must be noted:

- The altitude at which the onset of low emissivity phenomena occurs varies from feature to feature. It is substantially higher than average at very high

latitudes; it is generally higher for large features, such as highlands and large shield volcanoes, than for smaller features.

- The rate at which emissivity falls above the critical radius varies from feature to feature.
- There are several occurrences of low emissivities at low altitudes, such as a few impact craters and plains areas.
- There are several occurrences of high emissivities at high altitudes, such as the dark summits in highlands and on volcanoes, the dark flows from Maat Mons, and the areas to the east and west of Maxwell Montes (Lakshmi Planum and western Fortuna Tessera).
- Even on features without dark summits (such as ridges and other uplifted areas), the minimum emissivities tend to lie at a distance from the highest altitudes.

3.5 Discussion

Our ultimate goal is to discover the particular mechanism(s) and material(s) responsible for high reflectivity and low emissivity on certain parts of Venus. Two mechanisms for low emissivity have been previously suggested, emission from high-dielectric surfaces and efficient subsurface volume scattering; within each of these is the possibility of a variety of materials. We will discuss these mechanisms in detail in the next two chapters.

In deciding which is the best model, we must consider, in addition to the specific observations described above, a number of more general questions.

1. How many different mechanisms and materials are responsible for low-emissivity surfaces on Venus? Because of the relative rarity of low-emissivity surfaces on Venus and elsewhere, it seems reasonable that only one mechanism is at work here. On the other hand, because of the different geological settings in which the phenomenon is observed, it is not hard to imagine that more than one material

is involved. We might use a second material to explain low emissivities in areas of low altitude, such as the plains areas. Also, the low emissivity of craters might be a result of material introduced by the impacting body, or of surface materials altered in the impact. Still, it seems likely that the majority of the low emissivity surfaces are the result of a single mechanism and material.

2. Is the average surface material in areas of low emissivity, as originally emplaced, somehow different from the average material emplaced elsewhere? If it is different, then we must explain how the difference comes about and why the different material occurs where it does on the surface, and not elsewhere. The difference might be one of composition, possibly just a single key component, or it might be a physical characteristic, such as the vesicularity of the lava. If the materials are on average the same in areas of low emissivity as elsewhere, then we must explain how the surface is altered to its present condition. We might also consider the possibility that a material is deposited onto the surface from the atmosphere.

3. What are the relative rates of chemical weathering, erosion, and resurfacing in the areas of interest? We must decide which plays the dominant role in a given location. If erosion or resurfacing occurs more quickly than weathering, for example, then chemical stability of materials might not be important. On the other hand, if the important constituent is not destroyed, but rather is *created* by chemical weathering, then we would prefer this reaction to occur more rapidly than erosion or resurfacing.

The rates of these processes are not well known, although we have some general ideas. The crater count on the surface somewhat constrains the overall rate of volcanism. An initial analysis of Magellan crater counts indicates a surface age of from 0 to 800 million years, indicating that the surface is geologically active [62]. The activity varies from place to place, though. The rate of erosion depends to a large degree on the local wind speed, as well as local surface relief. Chemical weathering in many cases reduces the density of rocks, making them more susceptible to erosion [18]. Early Magellan data reveal windblown deposits and evidence for slow, steady mass movements [1]. Pioneer Venus reflectivity data, though, indicates that the av-

erage permittivity of most of the surface is too high for exposure of soils greater than 10 cm deep [29]; the Venera panoramas, as well as the Magellan emissivity data, support this view. The rate of chemical weathering is largely unknown, although the high temperatures and pressures at the surface of Venus tend to accelerate chemical reactions. The absence of liquid water, though, would tend to slow many reactions as compared to similar reactions on earth. Further study of reaction rates under Venus surface conditions is needed.

5. Is the composition of the lower atmosphere stable? Changes in the concentration of certain gasses would have profound effects on the stability of certain minerals. If the atmosphere of Venus were somewhat different in the past, we may be looking at a surface which was created under different circumstances than exist at present, and has yet to equilibrate with the current atmosphere.

We will return to some of these points in the next two chapters, when we consider specific models for low emissivity surfaces on Venus.

Chapter 4

High-Dielectric Surfaces

4.1 Introduction

In the last chapter we found that there are significant portions of the surface of Venus which display an unusually low radiothermal emissivity. About 1.5% of the observed surface has an emissivity below 0.7; in a few places the emissivity falls as low as 0.3. At present, two possible explanations for this phenomenon have been advanced. The more recent explanation is that low-loss surface materials with efficient subsurface scattering may produce the observed effect, in essence by helping to block radiation from escaping from the material. This possibility is explored in the next chapter. The older explanation for low emissivity areas is that materials of unusually high dielectric constant exist at the surface in these places. In this case, surfaces composed of materials with bulk dielectric constants up to 170 would be needed to explain the lowest observed emissivities. Except for liquid water, which cannot exist at the surface of Venus, materials of dielectric constant much greater than 15 are not common in terrestrial environments. Most surface rocks on Earth have dielectric constants of 10 or less. However, high-dielectric rocks do exist, and it is possible that conditions on Venus may be favorable to their creation. The possibility of high-dielectric surfaces on Venus is the topic of this chapter.

The next section contains a review of the theory of dielectric properties of materials; section 4.3 reviews general data on the dielectric properties of rocks. (Informa-

tion from both of these sections will be useful in the next chapter as well.) We then specifically consider rocks with high dielectric constants, and the possibility that such materials could exist on Venus.

4.2 Dielectric Properties of Materials

(This section is derived mainly from von Hippel [79].)

4.2.1 Permittivity and Permeability

The behavior of radiation in a medium is governed by the dielectric properties of the medium. In an isotropic medium, the electric displacement $\vec{D}$ and the electric field intensity $\vec{E}$ are related by the (complex) scalar permittivity ε^* of the medium:

$$\vec{D} = \varepsilon^* \vec{E}. \tag{4.1}$$

The relative permittivity ε of the medium is given by

$$\varepsilon = \frac{\varepsilon^*}{\varepsilon_0} \tag{4.2}$$

where $\varepsilon_0 = 8.854 \times 10^{-12}$ F/m is the permittivity of free space. The relative permittivity may be written as the combination of its real and imaginary parts:

$$\varepsilon = \varepsilon' - i\varepsilon''. \tag{4.3}$$

ε'' is often referred to as the loss factor, and the ratio

$$\tan\delta = \frac{\varepsilon''}{\varepsilon'} \tag{4.4}$$

the loss tangent. The relative permittivity is also known as the dielectric constant. It is dependent on many factors, including the frequency of the applied field. For most materials, and for all materials we will consider in this paper, $\varepsilon' \geq 1.0$. If ε'' is

greater than zero, the material is said to be lossy.

Similarly, the magnetic field $\vec{H}$ and the magnetic induction $\vec{B}$ are related by the (complex) permeability μ^* of the medium:

$$\vec{B} = \mu^* \vec{H}. \tag{4.5}$$

The relative permeability μ of the medium is given by

$$\mu = \frac{\mu^*}{\mu_0} \tag{4.6}$$

where $\mu_0 = 1.257 \times 10^{-6}$ H/m is the permeability of free space. The relative permeability may be written as the combination of its real and imaginary parts:

$$\mu = \mu' - i\mu''. \tag{4.7}$$

μ'' is sometimes called the magnetic loss factor, and the ratio

$$\tan \delta_\mu = \frac{\mu''}{\mu'} \tag{4.8}$$

the magnetic loss tangent. Like permittivity, permeability is also dependent on many factors, including the frequency of the applied field. For real materials, permeability may be either greater than one (paramagnetic and ferromagnetic materials) or less than one (diamagnetic materials). Only ferromagnetic materials, though have permeabilities significantly different from 1; in general, materials are considered non-magnetic ($\mu = 1$) unless otherwise stated.

Commonly used related quantities are the index of refraction,

$$n = \sqrt{\varepsilon \mu}, \tag{4.9}$$

and the intrinsic impedance,

$$Z = \sqrt{\frac{\mu^*}{\varepsilon^*}}. \tag{4.10}$$

4.2.2 Microscopic Phenomena Controlling Permittivity

Much research has been done into the molecular and atomic phenomena which control macroscopic dielectric properties. An electric field applied to a material tends to separate the positive and negative charges within the material, thus inducing a polarization. The magnitude of the polarization is directly related to the real part of the dielectric constant.

Four types of polarization are possible. In *electronic polarization*, the electron clouds are displaced relative to the atomic nucleus. *Atomic polarization* is the displacement of atoms in ionic molecular bonds from their equilibrium positions. *Dipole*, or *orientation polarization* involves the alignment of permanent dipole molecules (for example, free water molecules) with the applied field. The fourth type of polarization involves the motion of free charges (electrons or ions) in a heterogeneous material. Called *interfacial polarization*, or *surface charge polarization*, it occurs when the free charges, moving under the influence of the applied field, build up at surfaces across which the charges cannot move (for example, at the edges of conducting inclusions within an insulator). [39, 79]

The frequency spectrum of the dielectric constant is related to the time that it takes each type of polarization within a material to occur. At low frequencies, all types of polarization may occur; in a steady-state field, the real part of the permittivity is at its maximum value. As frequency increases, the inertia of the molecules, atoms, and even electrons causes them to lag behind the applied field, until in the high frequency limit, no polarization occurs and the material has a relative permittivity of 1. All four types of polarization may occur at radio frequencies. [39, 53]

Dielectric loss is the result of "friction" which occurs as the material reacts to the applied electric field [53]. At the risk of oversimplifying a very complicated subject, we divide loss into two general types. The first type, associated mainly with electronic, atomic, and orientation polarization, occurs at frequencies where the polarization lags behind the changes in the applied field. Reviews of the theories and mechanisms

involved in this type of loss may be found in [53, 38]. The second type of loss is the ohmic loss associated with the transport of charge carriers (usually electrons) through the medium. This occurs in materials where interface polarization occurs, but may also occur in materials where there are no surfaces at which the charge accumulates. In certain materials, such as metals, this factor dominates all other polarization and loss factors in the material. If a material has a frequency-independent ohmic conductivity σ, we may write the relative permittivity as

$$\varepsilon = \varepsilon' - i\left(\varepsilon_a'' + \frac{4\pi\sigma}{\omega\varepsilon_0}\right) \tag{4.11}$$

where ε_a'' is the non-ohmic loss and ω is the angular frequency of the applied field.

A given material (for example, a rock) may contain several different types of atoms and molecular bonds, as well as crystal defects, impurities, grain interfaces, pore spaces, etc. Each different polarization mechanism in a material will probably have a different amplitude and different frequency characteristics. Although the general principles are known, it is difficult to predict the dielectric properties of most materials based on theory alone. Actual measurements of permittivity, especially at or near the frequency of interest, are very important.

4.2.3 Propagation of Radiation in Matter

The propagation of radiation in a medium is governed by the dielectric properties of the medium and by Maxwell's equations. For a plane wave of angular frequency ω propagating along the z axis in the positive direction,

$$\vec{E} = \vec{E}_0 e^{i\omega t - \gamma^* z}, \tag{4.12}$$

$$\vec{H} = \vec{H}_0 e^{i\omega t - \gamma^* z}. \tag{4.13}$$

The complex propagation factor γ^* is given by

$$\gamma^* = i\omega\sqrt{\varepsilon^*\mu^*} = \alpha + i\beta \tag{4.14}$$

where α is the attenuation factor and β is the phase factor of the wave. If we expand γ^* in the above equations, they become

$$\vec{E} = \vec{E}_0 e^{-\alpha z} e^{i(\omega t - \beta z)}, \tag{4.15}$$

$$\vec{H} = \vec{H}_0 e^{-\alpha z} e^{i(\omega t - \beta z)}. \tag{4.16}$$

Thus the fields are attenuated by a factor of $e^{-\alpha}$ per unit length. The Poynting flux is proportional to the product of the electric and magnetic field magnitudes, and therefore the power is attenuated by a factor of $e^{-2\alpha}$ per unit length. We define the power attenuation coefficient in the medium as

$$\alpha_P = 2\alpha = 2\mathrm{Re}\left\{i\omega\sqrt{\varepsilon^*\mu^*}\right\}. \tag{4.17}$$

The power absorption length, the distance over which the power is attenuated by a factor of e, is the reciprocal of the power attenuation coefficient:

$$L_{abs} = \frac{1}{\alpha_P}. \tag{4.18}$$

4.2.4 Emissivity of a Homogeneous Half-Space

If we know the dielectric properties of a medium, we can predict the emissivity of a smooth, flat surface composed of that medium. Consider the case of a plane wave in a homogeneous, isotropic medium with relative permittivity ε_1 and relative permeability μ_1, incident on the smooth surface of a homogeneous, isotropic medium with relative permittivity ε_2 and relative permeability μ_2 (Figure 4-1). The ratio of power reflected from the surface to power incident on the surface is given by the Fresnel reflection coefficients [79]:

$$R_\perp(\phi) = \left(\frac{Z_2\cos\phi - Z_1\cos\phi'}{Z_2\cos\phi + Z_1\cos\phi'}\right)^2, \tag{4.19}$$

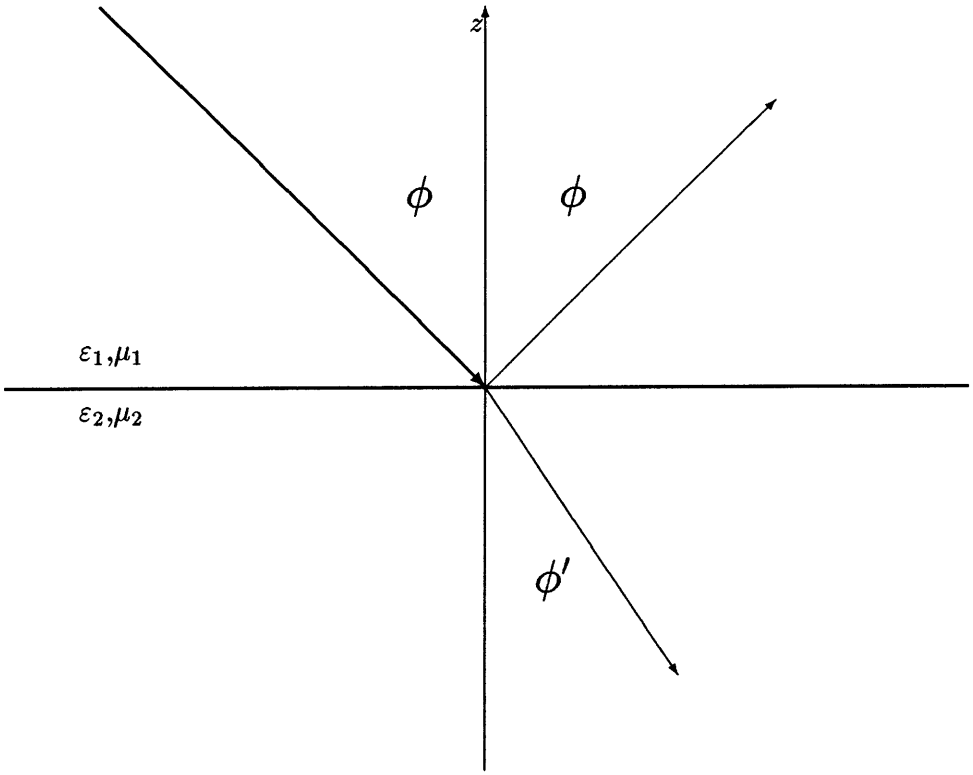

Figure 4-1: Geometry of Fresnel reflection and transmission. The scattering plane is defined by the direction of the incident radiation and the surface normal (in this case, the scattering plane is the plane of the paper). Radiation whose electric field vector vibrates in the scattering plane is said to have vertical polarization (subscript "$\|$"); radiation whose electric field vector vibrates normal to the scattering plane is said to have horizontal polarization (subscript "$\perp$").

$$R_{\|}(\phi) = \left(\frac{Z_2 \cos\phi' - Z_1 \cos\phi}{Z_2 \cos\phi' + Z_1 \cos\phi}\right)^2 . \tag{4.20}$$

(4.21)

Z_1 and Z_2 are the intrinsic impedances of the media, ϕ is the angle of incidence (measured from the upward surface normal), and ϕ' is the angle of refraction (measured from the downward surface normal). ϕ' is given by Snell's law:

$$\frac{\sin\phi}{\sin\phi'} = \frac{n_2}{n_1} \tag{4.22}$$

where n_1 and n_2 are the refractive indices of the media.

The emissivity of the smooth surface of a homogeneous, isotropic half-space, as a function of polarization and emitting angle, is the complement of the Fresnel reflectivity for the same polarization and incidence angle:

$$e_{\perp}(\phi) = 1 - R_{\perp}(\phi), \tag{4.23}$$

$$e_{\parallel}(\phi) = 1 - R_{\parallel}(\phi). \tag{4.24}$$

This is an application of equation 2.10; for specular reflection from a single surface, the hemispherical-directional reflectance is simply the Fresnel reflectivity at that angle. The polarization ratio, the ratio of radiation emitted with vertical polarization to radiation emitted with horizontal polarization, is

$$\frac{V}{H} = \frac{e_{\parallel}(\phi)}{e_{\perp}(\phi)} = \frac{1 - R_{\parallel}(\phi)}{1 - R_{\perp}(\phi)}. \tag{4.25}$$

Figure 4-2 displays the Fresnel emissivities of materials of dielectric constants 5, 20, 80, and 170, in vacuum. The emissivity at low angles falls as the permittivity of the material increases; also, while the difference in emission between the two polarizations at low angles is relatively small, the difference at large angles is very pronounced. Figure 4-3 plots the emissivity at normal incidence as a function of the dielectric constant of the material. Figure 4-4 shows the polarization ratio at viewing angles 25°, 40°, and 50° as a function of the dielectric constant of the material.

It is important to realize that most planetary surfaces do not behave quite so simply. Two effects are of particular note. The first is the roughness of the surface. Roughness is difficult to study, as it is very difficult to quantify. Although roughness may occur on any scale, we generally distinguish only roughness at scales on the order of a wavelength, smaller than the wavelength, and larger than the wavelength.

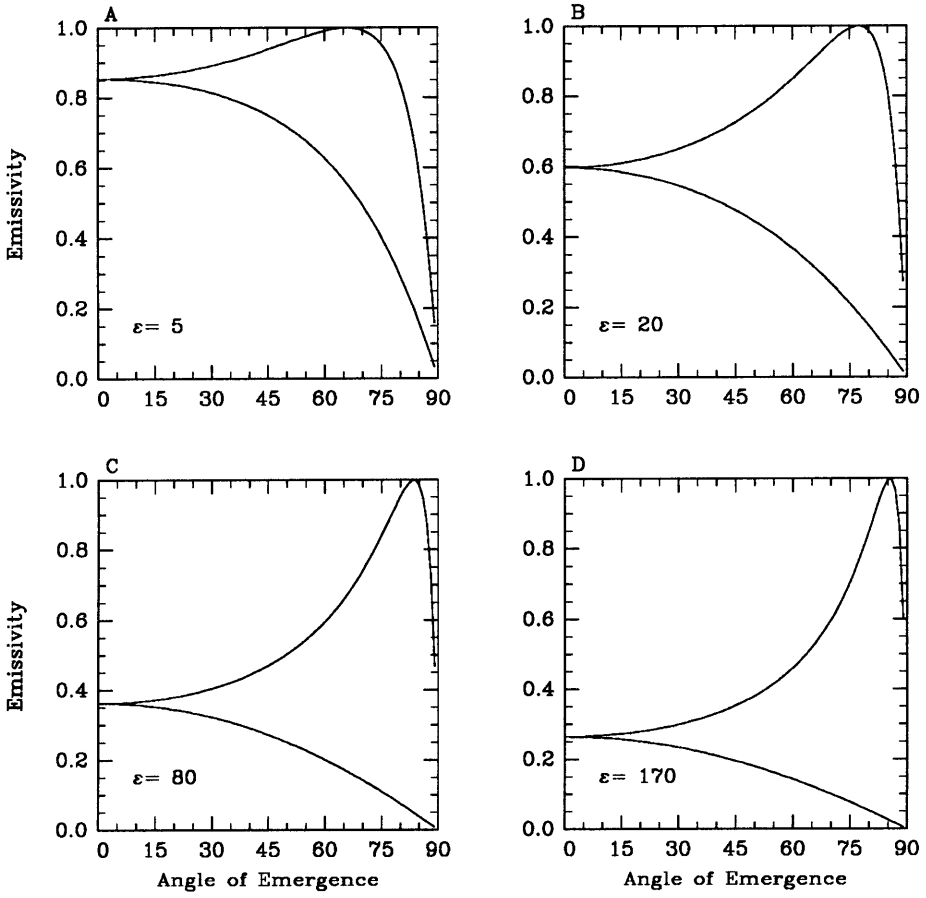

Figure 4-2: Fresnel emissivity as a function of emergence angle (equations 4.23 and 4.24) for materials of dielectric constant 5 (A), 20 (B), 80 (C), and 170 (D), under vacuum. Upper curves are vertical polarization, lower are horizontal.

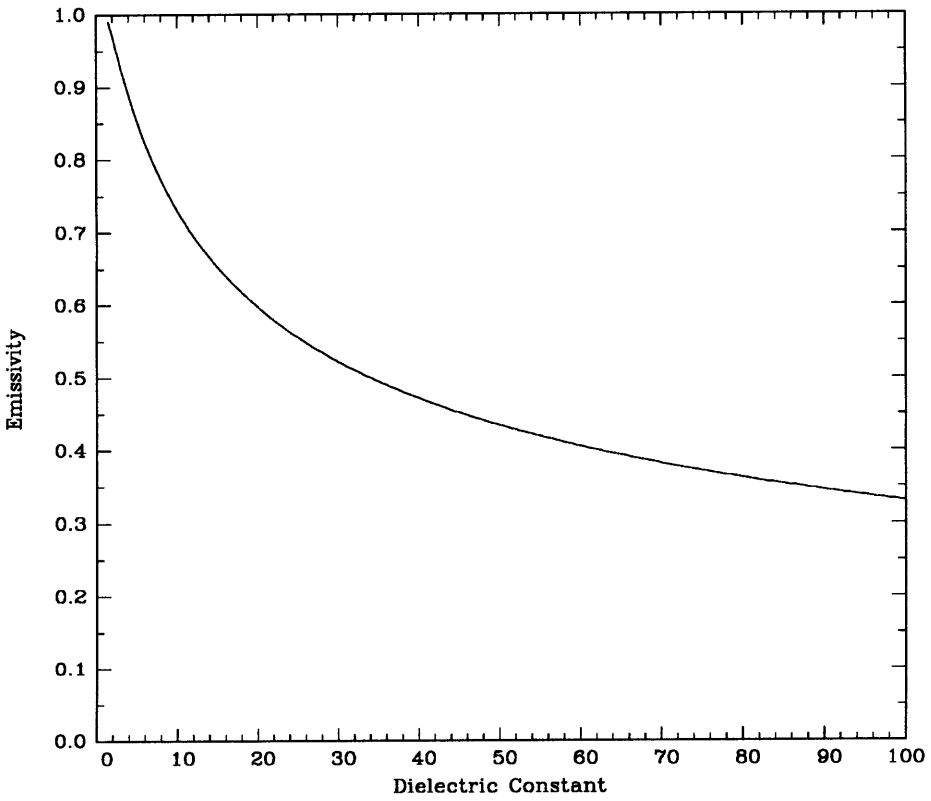

Figure 4-3: Fresnel emissivity viewed normal to the surface as a function of dielectric constant for materials under vacuum.

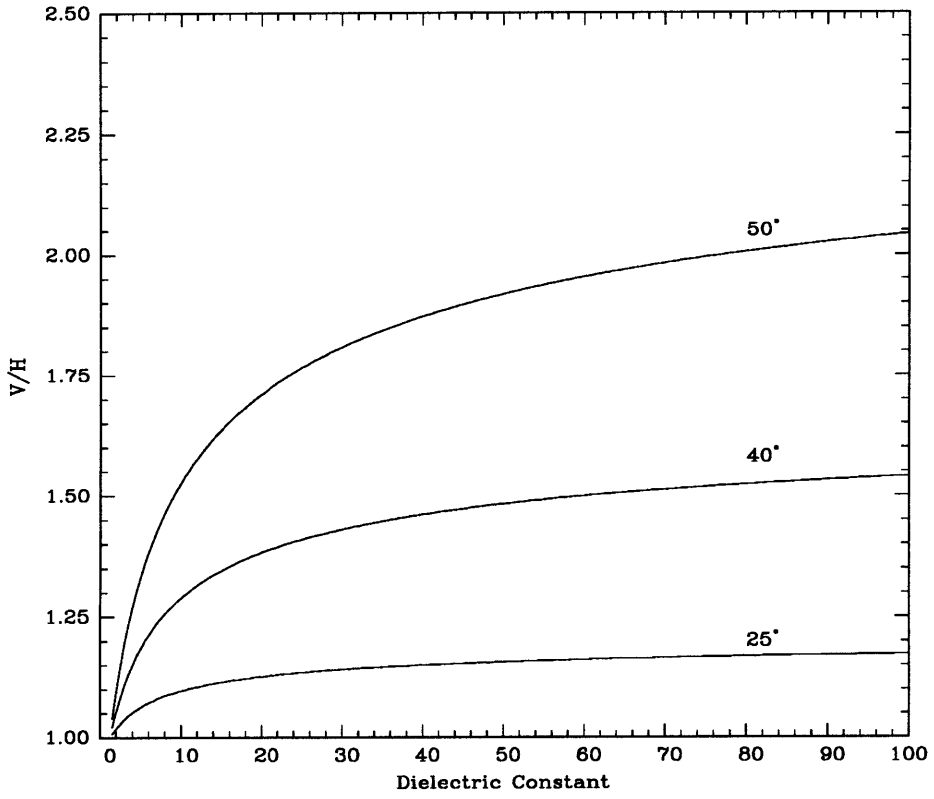

Figure 4-4: Fresnel emissivity polarization ratio as a function of dielectric constant (equation 4.25) for materials under vacuum, for emergence angles 25°, 40°, and 50°.

Fortunately for us, while roughness may substantially affect the scattering pattern of the surface, it does not greatly alter the total amount of radiation which is transmitted through the surface, when averaged over areas larger than the scale of the roughness. Thus the overall impact of roughness on emissivity is minimal. The specific effects are to decrease the difference between the polarizations, drawing them toward their average, and also to average the emissivity as a function of viewing angle, resulting in a flatter curve. [76]

The second effect is subsurface scattering, or volume scattering. Volume scattering may increase the reflectance of a surface, and likewise reduce its emissivity. A discussion of the effects of volume scattering on the emissivity of a surface may be found in the next chapter.

4.3 Dielectric Properties of Rocks

4.3.1 General Studies

As a reference point for our theoretical study of the causes of low emissivity surfaces on Venus, it is useful to know the dielectric properties of ordinary rocks at microwave frequencies. Many studies of the electrical properties of rocks have been done over the years, but only a few at microwave frequencies. In this section, we will review the results of two studies, one by Campbell and Ulrichs [5], and another by Ulaby et. al [74, 73].

In the late 1960's, Campbell and Ulrichs [5] measured the permittivities of various igneous rocks at 450 MHz and 35 GHz. Samples were dried for two days at 200°C in a vacuum oven prior to measurement. At 450 MHz, the permittivity was determined by a resonant cavity technique; at 35 GHz, a waveguide (transmission line) method was used. Reported values represent the average of at least three measurements. Table 4.1 lists the complex permittivities measured in this study, at both frequencies.

Campbell and Ulrichs make a few observations about the permittivity data. First, they note that the real part of the permittivity does not vary remarkably between the

two frequencies, supporting the notion that the spectrum of these rocks is rather flat in this range. Second, there is a tendency for the real part of the permittivity to be higher in basaltic rocks than in granites and rhyolites; this difference may be a result of density differences, or bulk composition, or both. Third, the power absorption lengths vary by more than a factor of ten, and there is not a strong correlation between absorption length and rock type.

In addition to the study of solid rocks, Campbell and Ulrichs measured the permittivities of several powdered rocks. They find that the best fit to the data is given by the Rayleigh mixing formula,

$$\frac{1}{\rho}\frac{\varepsilon-1}{\varepsilon+2} = \frac{1}{\rho_0}\frac{\varepsilon_0-1}{\varepsilon_0+2}, \tag{4.26}$$

where ε_0 and ρ_0 are the relative permittivity and density of the solid material, respectively, and ε and ρ are the relative permittivity and density of the powder. Their calculations show that for the rocks in the study, the Rayleigh mixing formula predicts that for a rock powder of density 1.0 g/cm^3, the real part of the permittivity will fall between 1.8 and 2.1, no matter what the composition. The absorption lengths of rock powders are somewhat longer than those of their solid counterparts.

Finally, Campbell and Ulrichs measure the effect of temperature on the permittivity of five (solid) rock samples (tholeiitic and olivine basalts, quartz, aplite granite, and olivine peridotite). They found that (at 35 GHz) the real part of the permittivity did not vary significantly over the range 300K to 800K, although in four of the five cases there was a slight rise with temperature (at most 15%). The loss tangent of four of the five samples rose significantly over the temperature range; the loss tangent of the quartz sample rose and then fell.

A more recent study of the electrical properties of rocks was made by Ulaby, et al. [74, 73]. They investigated the permittivities of 80 rock samples at frequencies from 0.5 GHz to 18 GHz. The real part of the permittivity, ε', was measured in 0.1 GHz increments across the entire range, although it was found that ε' is approximately independent of frequency in this range. The imaginary part of the permittivity, ε'',

was measured at 1.6 Ghz, 5 GHz, 7.8 GHz, 11.4 GHz, and 16 GHz. Samples were dried at 100°C for 15 minutes prior to testing. A dielectric probe system was used to measure ε'; resonant cavities were used to measure ε''. Reported values of ε' represent the average of at least 16 measurements at different locations on the sample surface, averaged over frequency; values of ε'' are the averages of measurements for five different samples of the same rock. Table 4.2 lists some of the permittivity data from this study.

For comparison, a few measurements of permittivity were performed without drying the sample prior to testing. There was little difference in the real part of the permittivity with and without drying; the imaginary part, however, was found to vary by as much as a factor of two in some cases.

Ulaby, et al. also measured the bulk density of all samples, and analyzed the bulk chemical composition of 56 of the samples. With this information, it was determined that within particular rock types, about 50% of the variance in ε' could be attributed to bulk density, and that 90% of the variance could be explained by the combination of density and fractional contents of SiO_2, Fe_2O_3, MgO, and TiO_2. On the other hand, statistically significant correlations between ε'' and either density or chemical composition could not be made.

4.4 Rocks with High Dielectric Constants

The data from the two studies in the previous section lead us to believe that no ordinary rocks have high enough dielectric constants to bring about emissivities as low as 0.3–0.6. If we wish to explain low emissivities on Venus by surfaces with high dielectric constants, we must search for more unusul materials.

4.4.1 Water

The most common high dielectric substance on the surface of the earth is water. At room temperature, at a wavelength of 10 cm, ordinary water has a permittivity of approximately $\varepsilon = 80 - i12$ [78, 46], which implies a normal emissivity of 0.36. Unfor-

Table 4.1: Permittivities of rocks measured by Campbell and Ulrichs [5].

Name	450 MHz		35 GHz	
	ε'	ε''	ε'	ε''
andesite, hornblende	5.1	0.020	5.0	0.070
anorthosite	6.8	0.054	6	0.096
basalt	8.9	0.160	9.2	0.828
basalt	8.0	0.240	8.6	0.602
basalt, amygdaloidal	7.2	0.101	7.6	0.175
basalt, hornblende	6.7	0.087	6.5	0.260
basalt, leucite-nepheline tephrite	5.6	0.058	5.3	0.122
basalt, olivine	8.1	0.138	8.0	0.720
basalt porphyry, olivine	8.2	0.131	8.1	0.486
basalt, tholeiitic	9.6	0.864	8.0	0.896
basalt, vesicular	7	0.119	5.3	0.212
gabbro, bytownite	7	0.140	7	0.126
granite, alkali	5.2	0.177	5.3	0.122
granite, aplite	5.2	0.099	4.9	0.044
granite, biotite	6	0.120	5.7	0.285
granite, biotite	5.4	0.038	5.5	0.082
granite, graphic	5.0	0.020	5.0	0.040
granite, hornblende	6	0.060	5.2	0.052
granite, porphyritic biotite	5.5	0.060	5.6	0.112
obsidian	6.8	0.884	5.6	0.280
obsidian	5.5	0.074	5.4	0.206
peridotite, mica	6.0	0.204	5.3	0.180
peridotite, olivine (dunite)	6.2	0.062	6.1	0.122
peridotite changing to serpentine	7.5	0.060	7.6	0.084
phonolite	6.5	0.195	6.3	0.183
pumice	2.5	0.017	2.4	0.048
rhyolite	3.38	0.051	3.41	0.024
serpentine	6.4	0.070	6.4	0.256
serpentine	7	0.133	6.4	0.384
syenite, augite (larvikite)	8	0.400	6.7	1.340
trachyte	5	0.130	5.43	0.136
tuff, gray	6.1	0.366	5.4	0.378
tuff, rhyolitic	3.6	0.022	3.4	0.068
tuff, semi-welded	2.6	0.029	2.6	0.078
volcanic ash	3.4	0.238	2.84	0.040
volcanic ash shale	2.7	0.081	2.6	0.039

Table 4.2: Permittivities of rocks measured by Ulaby et al. [74]. Values of ε' are averages across range 0.5–18 GHz; values of ε'' are those measured at 1.6 GHz.

Name	ε'	ε''
gypsum	3.9	<0.002
limestone	7.4	0.026
calcite	7.7	0.022
limestone	7.9	0.032
limestone	6.8	0.027
limestone	6.4	0.028
limestone	7.6	0.030
dolomite	6.8	0.036
dolomite	6.5	0.027
dolomite	6.7	0.031
calcareous sandstone	7.0	0.074
silicified volcanic	4.8	0.014
dacite/dellenite	5.8	0.211
dacite - lava flow	5.6	0.130
dacite - lava flow	6.3	0.099
dacite/rhyodacite	5.8	0.147
rhyolite - flow	5.2	0.074
rhyolite clasts	5.0	0.046
rhyolite - lava	5.4	0.075
rhyolite - lava	5.2	0.080
rhyolite - tuff	4.8	0.121
rhyolite - tuff	4.0	0.035
rhyolite - tuff	3.7	0.050
rhyolite - tuff	4.8	0.105
rhyolite - tuff	6.0	0.158
andesite	6.5	0.039
diabase	6.6	0.112
basalt	7.3	0.180
basalt	7.6	0.158
diabase	7.2	0.132
basalt	6.1	-
basalt	6.0	-
basalt	5.5	-
basalt	6.0	-
basalt	3.6	-
basalt	6.7	-
oceanic basalt	6.5	0.080
basalt/andesite	7.6	0.111

Name	ε'	ε''
quartzite	4.9	<0.002
alk granite	6.5	0.120
altered granodiorite	5.3	0.048
tonalite	5.9	0.048
diorite/quartz	6.1	0.105
monzonite	6.2	0.105
grandodiorite	6.0	0.047
diorite	6.5	0.052
gabbro	7.3	0.161
ol-gabbro	6.6	0.075
nepheline syenite	6.0	0.016
ijolite	6.4	0.032
norite	6.4	0.106
lamprophyre	8.3	0.101
pyroxenite	7.0	0.238
dunite	6.1	0.021
sandstone	2.5	0.015
sandstone	6.0	0.077
sandstone	4.0	0.028
sandstone	3.4	0.035
sandstone	3.7	0.042
sandstone	5.3	0.112
sandstone	4.0	0.040
sandstone	3.5	0.021
bentonite	5.7	0.220
shale	4.8	0.082
sandstone	4.3	0.076
siltstone	5.6	0.120
sandstone	3.1	0.024
shale	5.4	0.140
shale	5.3	0.140
siltstone	4.8	0.080
sandstone	3.0	0.030
sandstone	5.0	0.040
siltstone	6.5	0.038
sandstone	4.7	0.050
siltstone	5.9	0.245
sandstone	2.9	-
N/A	6.1	0.100
Elgygytgyn	5.6	0.030
aplite	5.4	<0.002
alkalic	5.6	0.074

Table 4.3: DC electrical resistivity (at 470°C) and dielectric loss factor (at 2.385 GHz) for some common conductors. Resistivity was calculated from room-temperature values and temperature coefficients (when available) given in [80, pg. F-122]. Loss factor calculation assumes that the conductivity is independent of frequency.

Element	Resistivity ($\mu\Omega$-cm)	ε''
Aluminum	4.6	1.3×10^{10}
Carbon (graphite)	1375.	4.3×10^{7}
Copper	3.4	1.8×10^{10}
Iron	12.6	4.7×10^{9}
Manganese	185.	3.2×10^{8}
Titanium	42.	1.4×10^{9}

tunately, due to the extreme temperature, liquid water cannot exist on the surface of Venus. Water is actually somewhat of a hindrance in the study of dielectric properties of materials, since adsorbed and pore water can cause inaccurate measurements of the dielectric constants of other materials. (This is why the drying of specimens is so important.)

4.4.2 Metals

Other common high dielectric materials are the metals. Metals have high dielectric constants for two reasons. First, the real part of the dielectric constant is somewhat high because of the relatively large atomic radii of the atoms, which leads to a high electronic polarizability [55]. The loss factor is high as a result of conduction in the crystal structure. As was shown earlier, the conductivity of a material directly affects the loss factor. From equation 4.11, it is easily found that to achieve a value of the loss factor of 75 or above at the Magellan radar frequency, the resistivity of a material must be less than about 10 Ω-cm. Table 4.3 lists the dielectric loss factors for a few common conducting elements. Calculations of the loss factor in this table assume that the conductivity is independent of frequency. At microwave frequencies, most metals are nearly indistinguishable from perfect conductors, and are almost totally reflecting.

Along with their study of terrestrial rocks, Campbell and Ulrichs [5] measured the

Table 4.4: Permittivities of meteorites at 450 MHz (from Campbell and Ulrichs [5]; meteor types from Nozette [52].)

Meteorite	Type	ε'	$\tan\delta$
Bonita Springs	H5	43–81	0.13–0.19
Burderheim	L5	9.0–11.9	0.035–0.048
Colby	L5	10.6–11.8	0.045–0.054
Forest City	H5	16–33	0.11–0.22
Holbrook	L5	7.8	0.015
Indarch	E4	130–150	0.065–0.117

permittivities of a few meteorites at 450 Mhz. Results are shown in table 4.4. The meteorites with low metal content (type L) have dielectric properties consistent with those of ordinary rocks, whereas the meteorites with substantial metal content (types H and E) have much higher values of ε' (possibly due to interfacial polarization) and dielectric loss.

4.4.3 Ore Minerals

More likely than the existence of free metals on the surface of Venus is the existence of metallic ores. Various authors have suggested that minerals such as pyrite (FeS_2), pyrrhotite (Fe_xS), magnetite (Fe_3O_4), rutile (TiO_2), ilmenite ($FeTiO_3$), pyrolusite (MnO_2), etc., may explain the areas of high reflectivity (and low emissivity) on Venus (see next section). Very little study has been made of the dielectric properties of ore-bearing rocks at microwave frequencies. We can derive some information from data compiled by Parkhomenko [55] from a variety of other sources. Table 4.5 lists the minerals from Table 2 of [55] which have a permittivity of 20 or more. The frequency at which the measurements were done is not known in most cases; it is likely that these are static (zero frequency) values. Since polarization mechanisms have their maximum effect at zero frequency, we would expect that ε' would, if anything, decrease with frequency; we are thus safe in ignoring the other minerals in the table, as far as ε' is concerned.

As in metals, the dielectric loss in minerals is, in addition to a function of the loss incurred in polarization, a function of their conductivity; as in metals, a high conduc-

Table 4.5: Permittivities of selected minerals (data from Parkhomenko [55]).

Mineral	Formula	ε	Frequency (Hz)
Graphite	C	> 81	-
Chalcocite	Cu_2S	> 81	-
Argentite	Ag_2S	> 81	-
Galena	PbS	> 81	-
Pyrrhotite	Fe_xS	> 81	-
Molybdenite	MoS_2	> 81	-
Pyrite	FeS_2	$> 33.7 < 81$	-
Cobaltite	CoAsS	$> 33.7 < 81$	-
Arsenopyrite	FeAsS	> 81	-
Hematite	Fe_2O_3	25	-
Magnetite	Fe_3O_4	$> 33.7 < 81$	-
Ilmenite	$FeTiO_3$	$> 33.7 < 81$	-
Braunite	$3Mn_2O_3 \cdot MnSiO_3$	> 81	-
Pyrolusite	MnO_2	10^5	-
Lead monoxide	PbO	26	-
Platnerite	PbO_2	26	-
Brookite	TiO_2	78	-
Anatase	TiO_2	48	-
Rutile	TiO_2	89–173	50
Perovskite	$CaTiO_3$	170	50
Cassiterite	SnO_2	24	-
Cerussite	$PbCO_3$	23	-
Wulfenite	$PbMoO_4$	27	-
Pyromoerphite	$Pb_5(PO_4)_3Cl$	26	-

tivity can cause the dielectric loss to dominate the dielectric constant. Table 4.6 lists resistivity data for a number of semiconductor minerals as compiled by Parkhomenko [55]. (Similar data for a different set of minerals, including many uncommon minerals, is contained in [6].) Only minerals with a minimum resistivity of less than 50 Ω-cm are listed. Data for a few nonconducting minerals is shown for comparison. Many of the ore minerals have sufficient conductivity to result in high values of ε' at microwave frequencies. It is also interesting to note that certain groups of ore minerals which had sufficiently high ε (≥ 20) to appear in table 4.5—in particular, most ores of lead, titanium, and manganese—do not have correspondingly high conductivities.

4.4.4 Rocks

We finally arrive at the question, "What sort of rocks have high dielectric constants?" Three possibilities come to mind. The first is rather trivial: a rock composed entirely of a mineral with a high dielectric constant. We need not discuss this possibility further at the moment. The second possibility is somewhat exotic: a rock with a surface coating of a high dielectric material. This is similar to what happens when a layer of water is adsorbed onto the surface of a material, as mentioned above. Such a layer could arise, for example, from vapor deposition of a metal, or from condensation of some atmospheric component, or from chemical weathering of the rock surface.

The third possibility is the most familiar scenario: rocks containing some amount of ordinary, low-dielectric minerals, along with some high-dielectric minerals. Qualitatively, one expects the effective dielectric constant to lie somewhere above the minimum of the dielectric constants of the components. Thus, for example, a rock consisting of crystals of rutile in a quartz matrix would have a dielectric constant somewhat higher than plain quartz. There are many ways of calculating the effective dielectric constants of composite materials. Reviews of mixing formulas are contained in [4, 55, 77]. Selection of the proper mixing formula to use in a particular situation is a difficult task; mixing formulas are derived using a variety of different physical models, assumptions, and approximations. Common practice in the field is to first measure the permittivity of various mixtures of two components, and then to find the

Table 4.6: Resistivities of semiconductor minerals, with resistivities of a few less conducting and nonconducting minerals for comparison. (data from Parkhomenko [55, tables 11 and 12]; rutile data from [6]).

Mineral	Formula	Resistivity (Ω-cm)
	Semiconductors	
Graphite	C	0.1–1000
Covellite	CuS	0.0001–0.003
Chalcocite	Cu_2S	4–2000
Argentite	Ag_2S	$0.2–1 \times 10^6$
Galena	PbS	0.003–30
Pyrrhotite	Fe_xS	0.0006–0.1
Molybdenite	MoS_2	50–20000
Pyrite	FeS_2	0.003–200
Marcasite	FeS_2	1–10
Chalcopyrite	$CuFeS_2$	0.001–5
Bornite	Cu_5FeS_4	0.002–0.5
Cobaltite	CoAsS	0.04–5
Arsenopyrite	FeAsS	0.01–0.4
Nicolite	NiAs	0.0002
Cuprite	CuO	0.1
Hematite	Fe_2O_3	$0.4–6 \times 10^5$
Magnetite	Fe_3O_4	$0.008–6 \times 10^5$
Braunite	$3Mn_2O_3 \cdot MnSiO_3$	20–100
Cassiterite	SnO_2	0.04–400
Manganite	MnO[OH]	1–30
	Poor Semiconductors	
Pyrolusite	MnO_2	200
Ilmenite	$FeTiO_3$	200
Rutile	TiO_2	3000–90000
	Nonconductors	
Diamond	C	5×10^{14}
Sulfur	S	1×10^{17}
Stibnite	Sb_2S_3	$1 \times 10^7–1 \times 10^{14}$
Anhydrite	$CaSO_4$	1×10^{11}
Calcite	$CaCO_3$	5×10^{14}
Quartz	SiO_2	$1 \times 10^{14}–2 \times 10^{16}$

mixing formula which best fits the data.

If the high-dielectric component of a rock is one of the relatively nonconductive minerals, such as the titanium and lead compounds, we would expect little interfacial polarization or ohmic loss; the dielectric constant of the rock should be intermediate between the dielectric constants of the components. Olhoeft and Strangway [54] have compiled data for the dielectric constants of lunar samples. The data indicate that lunar rocks containing up to about 12% by weight TiO_2 and 20% by weight FeO have dielectric constants of at most about 11 (at frequencies between 1 and 450 MHz). It seems that much higher concentrations of titanium than are found even in the lunar high-titanium basalts are needed to bring dielectric constants up into the desired range. More study of rocks containing Ti, Pb, and Mn would be helpful.

If the high-dielectric component of a rock is a semiconductor or conductor, the situation is more interesting. We can consider two different cases. In one case, the conductor occurs in isolated grains throughout a relatively nonconducting matrix. In the second, the conductor forms a continuous network throughout the rock (either because the grains are so numerous that they touch each other, or because the conductor is disseminated through the rock in a dendritic or layered manner).

In the case of the continuous network, there will be some degree of interfacial polarization at the boundaries between the conductor and matrix, but conduction and ohmic loss will probably play a more important role. Because of the continuous conducting paths, the measured DC conductivity of the rock will be similar to that of the pure conductive mineral, although in practice it is always somewhat less.

When the concentration of the conductive mineral is too low, or the distribution is geometrically unfavorable, there will not be continuous conducting paths, and the measured DC conductivity of the rock will be close to that of the nonconducting matrix material. The charge carriers in the conducting mineral will not be able to travel as far before running up against barriers. The importance of ohmic loss will decrease, but the effects of interfacial polarization will be greater. A material of this type, an insulating material containing isolated conducting grains, is sometimes called a "loaded dielectric".

Table 4.7: Permittivities of sulfide ores, measured by Nozette [52]. Sudbury samples were too conductive for measurement of permittivity.

Source	Volume Percent of Ore			1 GHz		1.7 GHz	
	FeS_2	Fe_xS	$CuFeS_2$	ε'	ε''	ε'	ε''
Bedford, NH	5%	2%	< 0.2%	21 ± 4	29 ± 7	14.7 ± 0.2	23 ± 10
Bedford, NH	4%	4%	2%	20 ± 6.5	6.2 ± 0.6	15.9 ± 0.5	6.4 ± 0.1
Sudbury, Ont.	45%	< 5%	45%				
Sudbury, Ont.	20%	< 2%	< 25%				
Sudbury, Ont.	40%	< 5%	40%				

Table 4.8: Resistivities of ores. (Data from Parkhomenko [55, tables 11 and 13–17].)

Mineral	Resistivity (Ω-cm)	
	Ore	Pure Mineral
Pyrite	10–30000	0.003–200
Pyrrhotite	10–200	0.0006–0.1
Chalcopyrite	0.01–70	0.001–5
Arsenopyrite	0.01–40	0.01–0.4
Galena	10–300	0.003–30
Chalcocite	3	4–2000
Magnetite	$50–2 \times 10^7$	$0.008–6 \times 10^5$
Hematite	$1–2 \times 10^5$	$0.4–6 \times 10^5$

A study by Nozette [52] contains measurements of the dielectric properties of a few samples of sulfide ores at microwave frequencies. Two samples were of metamorphic rocks from Berlin, New Hampshire; in addition to the sulfides, these rocks contained plagioclase, biotite, and chlorite, with minor amounts of magnetite and anthophyllite. Three more samples of high grade ore came from Sudbury, Ontario. Table 4.7 contains a summary of the results of the study. It should be noted that the Sudbury samples were too conductive to allow measurement of their dielectric constants. Measurements of the conductivity of these three samples were in the range 30–7500 $(\Omega\text{–cm})^{-1}$.

Data on the resistivity of metallic ores is compiled by Parkhomenko [55]. Table 4.8 contains a summary of the data, with a comparison to the resistivities of the pure minerals.

A very interesting study of the dielectric properties at microwave frequencies of a material with conducting inclusions was made by Kelly et al. [41]. Paraffin wax ($\varepsilon' = 2.25$, $\tan\delta < 0.0002$) was used as a matrix; in it were dispersed various types

Table 4.9: Dielectric constants of mixtures of paraffin and metal powders (from Kelly et al. [41]).

Suspended Material	Density (g/cm^3)	Volume Fraction	Particle geometry	Maximum dimension	Dielectric Properties ε'	$\tan\delta$	μ'	$\tan\delta_\mu$
Aluminum	2.7	0.18	Flakes	0.0008	28.0	< 0.01	0.86	0.09
Aluminum	2.7	0.18	Clumps	0.0002	6.1	< 0.01	0.90	0.07
Carbon	1.9	0.05	Powder	-	4.6	0.11	0.99	< 0.01
Carbonyl Iron	7.8	0.19	Spheres	0.0001	6.0	< 0.01	1.10	0.34
Copper	8.9	0.19	Clumps	0.0006	8.4	< 0.01	0.83	0.09
Magnetite	5.2	0.18	Powder	-	6.2	< 0.01	1.02	0.25
Rutile	4.3	0.12	Powder	-	4.7	< 0.01	1.00	< 0.01
Zinc	7.0	0.20	Spheres	0.0002	5.7	< 0.01	0.89	0.07
Zinc	7.0	0.24	Spheres	0.0002	8.2	0.02	0.82	0.09
Zinc	7.0	0.29	Spheres	0.0002	13.3	0.04	0.72	0.10

of metallic powders. The permittivities and permeabilities of the resulting mixtures were measured. Table 4.9 summarizes results for various types of suspended metallic particles. Despite the nonuniformity of the particle concentration at which the listed values of dielectric parameters were measured, it is clear that the aluminum flakes were the most effective in raising the permittivity of the mixture. A plot of the value of ε' for the mixture, as a function of the volume fraction of aluminum flakes, is shown in figure 4-5. Other data in the paper suggests that at least some other particle types may raise the permittivity at higher concentrations.

This data has been further analyzed by Pettengill et al. [57]. They use a theoretical expression for the bulk dielectric constant of a loaded dielectric to recalculate the data in figure 4-5 for a matrix composed of rock of dielectric constant 5.0 (instead of 2.25 for paraffin). The expression is based on previous work by Mossotti [51], Clausius [10], and others. If V is the volume fraction of conducting inclusions (which must be small compared to the radiation wavelength), and ε_1 is the permittivity of the host matrix material, then the bulk permittivity of the mixture is given by

$$\varepsilon = \varepsilon_1 \left[\frac{1 + (1 - \kappa)\gamma}{1 - \kappa\gamma} \right] \tag{4.27}$$

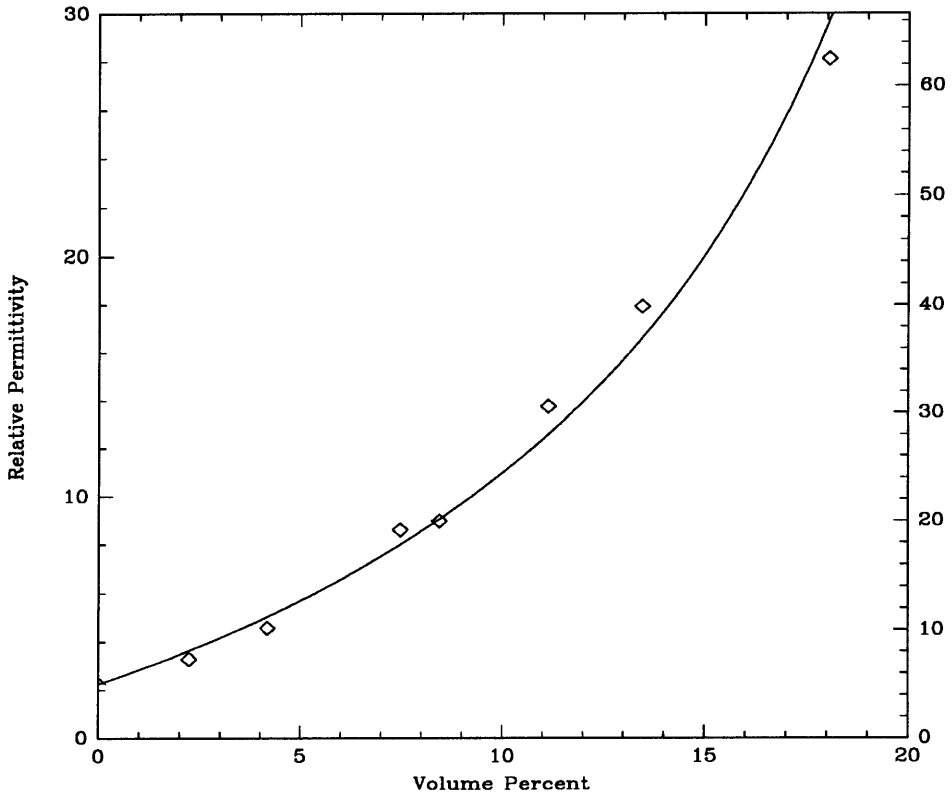

Figure 4-5: Bulk dielectric constant of mixture of paraffin and aluminum flakes (from Kelly et al. [41]). Right vertical axis shows the scale corrected to a rock matrix of permittivity 5.0 [57]. Curve is best fit to data of equation 4.27 [57] (see text).

where

$$\gamma = \frac{1}{3} V \sum_{i=1}^{3} \frac{1}{A_i}. \tag{4.28}$$

The quantities A_i are the depolarization factors, which characterize the particle shape. Values of A_i are easily calculated for ellipsoidal shapes (see [68, 77]). For spheres,

$$A_i = (\frac{1}{3}, \frac{1}{3}, \frac{1}{3}). \tag{4.29}$$

For prolate spheroids (cylinders, needles, rods, etc.),

$$A_i = (\frac{1}{2} - \xi, \frac{1}{2} - \xi, 2\xi), \tag{4.30}$$

where $\xi \rightarrow 0$ as the spheroid gets longer. For oblate spheroids (lamellae, disks, flakes, etc.),

$$A_i = (\xi, \xi, 1 - 2\xi), \tag{4.31}$$

where $\xi \rightarrow 0$ as the spheroid gets flatter. Note that $\sum A_i = 1$ in all cases.

κ in equation 4.27 parameterizes the effective permittivity surrounding each grain. The value of κ is not predicted by the theory, except that it is required to lie between 0 and 1, which correspond to effective surrounding permittivities of ε_1 and ε, respectively. A low value of κ indicates that the inclusions are decoupled from one another; we expect this to be true when their density is low.

As can be seen from the model, correction of the original data for a paraffin matrix to a matrix of rock of permittivity 5.0 is easily accomplished by multiplying the permittivities by the ratio 5.0/2.25 (also shown in figure 4-5). Pettengill et al. also performed a least squares fit to the data, and determined values for the parameters as follows: $\kappa = 0.137$, $\gamma/V = 25.3$.

4.4.5 Summary

There exist many naturally-occurring materials with high values of dielectric constant. Liquid water has a reasonably high permittivity at microwave frequencies, but cannot exist on the surface of Venus. Metals have very high permittivities, largely

because of their conductivity. Many ore minerals have high permittivities; some, but not all, have high conductivities. In order to have a high dielectric constant, a rock must contain some amount of high-dielectric minerals. The amount of these minerals is very important in determining the permittivity of the rock; however, the spatial distribution of the minerals can have an extremely important effect also. For example, relatively small amounts of conducting particles in a nonconducting matrix can raise the permittivity of the rock significantly, especially if the particles have an advantageous shape (lamellae or long needles). Experimental data on the permittivities of rocks with high dielectric constants is rare.

4.5 High Dielectric Materials on Venus

4.5.1 Surface Composition

The ambitious Soviets sent a total of thirteen missions to Venus over the past 25 years, and soft-landed ten spacecraft [11]. Information returned from the Venera and Vega landers gives us our best picture of the composition of the surface of Venus. Two types of elemental analysis were performed. Veneras 8, 9, 10, and Vegas 1 and 2 carried gamma-ray spectroscopy experiments. These experiments measured the gamma radiation emitted by surface rocks in the spectral range 0.3–3.0 MeV, which allowed determination of the absolute and relative abundances of potassium, uranium, and thorium. The analysis showed that the Venera 8 rocks were similar in radioactivity to alkaline basalts, while the Venera 9 and 10 surfaces were less radioactive, closer to terrestrial tholeiites [69]. Veneras 13, 14, and Vega 2 carried x-ray fluorescence experiments. In this experiment, a drill was used to obtain a rock sample from a depth of about 3 cm; the sample was irradiated in an evacuated chamber, and a spectrometer used to measure fluorescent x-ray radiation. From this information, abundances of the elements in the range Mg to Fe were determined (Vega 2 extended the range down to Na, and measured abundances of a few heavier elements). The Venera 13 sample was found to be similar in composition to a terrestrial leucitic basalt with a large

Table 4.10: Geochemical analysis of surface of Venus (from [18, table 3]).

Component	Mass %		
	Venera 13	Venera 14	Vega 2[a]
SiO_2	45.1±3.0	48.7±3.6	45.6±3.2
TiO_2	1.59±0.45	1.25±0.41	0.2±0.1
Al_2O_3	15.8±3.0	17.9±2.6	16.0±1.8
FeO	9.3±2.2	8.8±1.8	7.7±1.1
MnO	0.2±0.1	0.16±0.08	0.14±0.12
MgO	11.4±6.2	8.1±3.3	11.5±3.7
CaO	7.1±0.96	10.3±1.2	7.5±0.7
Na_2O	2.0±0.5	2.4±0.4	2.0
K_2O	4.0±0.63	0.2±0.07	0.1±0.08
SO_3	1.62±1.0	0.88±0.77	4.7±1.5
Total	98.1%	98.7%	95.4%

[a]Vega 2 also set the following upper limits:
< 0.3% Cl, Cu, Pb; < 0.2% Zn;
< 0.1% Sr, Y, Zr, Nb, Mo; < 0.08% As, Se, Br.

fraction of potassium; the Venera 14 rock was close to a tholeiitic basalt; and the Vega 2 rock was similar to an olivine gabbro norite [50, 70]. Table 4.10 summarizes data from the three x-ray fluorescence experiments.

Pictures returned from Veneras 9, 10, 13, and 14 [19, 50] show a landscape dominated by dark, flat rocks interspersed with darker soil. Grains and fragments are visible; some are noted to move between pictures. The rock density measured with a gamma ray densitometer by Veneras 9 and 10 was 2.8 g/cm^3, which is typical for low-porosity basalts [69]. The lander pictures, however, would lead one to think that portions of the surface are covered by some depth of loose soil, and thus are of lower density. The Venera 13 and 14 gamma ray detectors estimated rock densities of 1.5–2.0 g/cm^3 [20].

The sites which have been explored by the Venera landers are not in areas where low emissivity is observed; the locations are, as far as we know, typical of most of the surface. The observed basaltic composition is consistent with the widespread existence of volcanic structures, lava flows, etc. observed by Pioneer Venus, Veneras 15, 16, and Magellan. We have no first hand knowledge of the surface composition in the areas of interest in this paper.

4.5.2 Possible High-Dielectric Materials

Although we have knowledge of many natural materials with high dielectric constants, it is difficult to say which of these might exist on the surface of Venus. In papers discussing the high reflectivity areas on Venus, iron sulfides have been suggested several times; titanium and iron oxides have been suggested also.

Pettengill and colleagues [59, 21, 52, 57] suggest pyrite (FeS_2) because it is a rather widespread trace mineral on earth; more importantly, it is a fair conductor, and thus relatively small quantities dispersed in a rock matrix could result in a loaded dielectric (as discussed above). The study of surface-atmosphere chemical interactions by Klose et al. [44] confirms that iron sulfide phases may exist at high altitudes on Venus.

Suggestions of materials high in titanium and iron oxides have been made by Garvin, Head, and colleagues [24, 25, 27, 37]. These suggestions are based mainly on analogies with certain (uncommon) terrestrial and lunar basalts, such as terrestrial ultrapotassic basalts and the lunar basalts with over 10% TiO_2 mentioned earlier. Garvin et al. [27] also suggest the possibility of deposition of high-dielectric layers by posteruptive hematite (Fe_2O_3) production, which could be important in areas where fumarolic activity is extensive. The hematite could also be accompanied by oxides of manganese and copper [24].

Some suggestions rely on erosion to concentrate high-dielectric materials, which are generally of higher density than minerals with low dielectric constants. Head et al. [37] suggest that aeolian activity might concentrate higher density mineral grains; Greeley et al. [30] performed experiments which indicate that dense mineral grains can be concentrated on the surfaces of windblown sediments.

Fegley et al. [18] have published their own study of surface-atmosphere reactions and equilibria. Their calculations predict that iron sulfides, ilmenite ($FeTiO_3$), and perovskite ($CaTiO_3$) are not stable anywhere on the surface; magnetite (Fe_3O_4) and rutile (TiO_2) are stable. They suggest that Klose et al. [44] erroneously concluded that iron sulfides were stable at high altitudes because they neglected to consider the gas COS in their calculations. Fegley et al. also performed experiments which suggest that pyrite and pyrrhotite (Fe_xS) would weather rapidly to magnetite (Fe_3O_4) under

Venus surface conditions. Weathering of perovskite, on the other hand, is expected to be slow on a geological timescale, so they find this mineral the most likely candidate of those considered.

4.5.3 Conclusions

Each of the materials described in the previous section has its problems.

Perovskite may exist in places. However, the surfaces analyzed by the Soviet landers were not found to contain any unusual amount of TiO_2. If perovskite, or any titanium, manganese, or lead compound, is responsible for the surfaces of low emissivity, then we must require it to be emplaced almost exclusively in regions of high elevation. We know of no reason why this should occur. Furthermore, to account for the lowest emissivities, we would need nearly pure perovskite surfaces in places. This seems highly unlikely.

Posteruptive hematite deposits might also exist in places, but it seems unlikely that extensive deposits could exist in the highlands and in other places which are not volcanically active. Being a surface phenomenon, erosion would be likely to disperse the hematite over time. Also, hematite is weathered to magnetite under the oxidation conditions believed to exist at the surface of Venus [44]; however, the dielectric constants and conductivities of the two are sufficiently close that this would not make a difference.

The most promising solution to the problem is that some sort of conductive inclusions (probably an iron oxide or sulfide), created by chemical weathering of surface materials, result in a loaded dielectric. There are several reasons. First, iron is much more abundant than titanium, lead, or manganese. Also, oxygen and sulfur are abundant in atmospheric gasses. Thus, the proper constituents for the creation of iron oxides and sulfides are known to be present. Second, only small quantities of a conductor are needed to produce a surface with the desired properties. We still might require an unusually large fraction of conductor in the rock to explain the lowest emissivities, but we do not need rocks composed entirely of the conductor. Third, a phase change from a nonconductive mineral at low altitudes to a conductive mineral

at high altitudes would result in a sharp altitude boundary at which the phase change occurs. Even though our observations do not identify a single, clearly demarcated boundary between low and high emissivities, we do observe behavior consistent with such a phase change. Fourth, since weathering creates the high-dielectric phase from ordinary surface material, areas such as the south rim of Dali Chasma could be uplifted to altitudes above the critical radius, and the nonconductive phase near the surface converted to the conductive phase.

Differences in emissivity above the critical altitude could result from differences in the metal content of the rocks, from differences in surface erosion, and from differences in age. The dark flows of Maat Mons have a high emissivity because they have not had time to weather yet (as suggested by Klose et al. [44]). Areas of low emissivity at low altitudes are not explained by this model; neither are the dark summits, unless we regard them, along with Maat, as areas of recent activity, or decide that they are in fact depressions after all. There are other minor inconsistencies which would have to be addressed.

The loaded dielectric model has a few more serious problems. The first is one of chemistry. All of the iron minerals which have been considered so far—pyrite, pyrrhotite, magnetite, and hematite—are about equally conductive, at least according to existing data. Thus, we are left without a candidate for the nonconductive phase. Even though some of the thermodynamic models (i.e. that of Klose et al. [44]) predict a phase change from magnetite to pyrite at some altitude on the surface, this does not help us if the magnetite is as conductive as the pyrite. On the other hand, Klose et al. point out that the volume of pyrite per iron atom is greater than that of magnetite, by a factor of about 1.6. Since the bulk dielectric constant of a loaded dielectric depends on the volume fraction of the conducting inclusion (figure 4-5), the phase change from magnetite to pyrite should cause an increase in the bulk dielectric constant of the surface rocks. The effect could be enhanced by favorable changes in the shape of the conductive inclusions, for example, if the pyrite were to expand into planar regions between other mineral grains.

Another problem is the question of quantity. The largest fraction of iron measured

in any of the rocks tested by the Soviet landers was $(9.3 \pm 2.2)\%$ by weight FeO. If we take the upper end of the error bar (11.5% FeO), and, using sulfur from atmospheric gasses, convert all of the iron to pyrite, we obtain 17.8% by weight FeS_2. However, pyrite is denser than basalt; with a density of 5 g/cm^3 for pyrite, and 3 g/cm^3 for the rest of the basalt (which is rather high), we are left with 11.5% by volume of pyrite. Is this enough? It depends. If the dielectric constant of the matrix rock were 5.0, and the shape of the pyrite grains was the same as that of the aluminum flakes from Kelly's experiments (see figure 4-5), we could expect a dielectric constant of about 26. Equation 4.27, however, allows us three ways to increase the bulk dielectric constant of a loaded dielectric other than by increasing the quantity of the conducting phase: we may increase the dielectric constant ε_1 of the matrix, we may increase κ, which parameterizes the effective field around each grain, or we may change the shape of the grains so as to increase γ (equation 4.28). We could probably only justify an increase in ε_1 by a factor of at most 2, thereby raising the dielectric constant to around 50 (and in doing so ignoring the fact that the weathering which produced the pyrite possibly decreased the density and dielectric constant of the host rock). Further increases would have to arise through the other two parameters. At present, we do not have any basis on which to decide what value κ might take in a basalt loaded with pyrite, or what shape the grains would be.

In the original loaded dielectric model proposed by Pettengill et al. [59], iron sulfides are constituents of the originally emplaced lava in highland areas and tall volcanoes. The conducting phase is not required to be chemically stable; erosional processes uncover fresh material faster than it is weathered. We are required once again to explain why the lava which bears the high-dielectric component only appears at high altitudes; the explanation could be that it does not appear only at high altitudes, but that the weathering process is slower there and the erosional process much more efficient. Thus the critical altitude is not necessarily a sharp boundary caused by a phase transition, but rather is an inflection point in the change of the relative rates of weathering and erosion with altitude. The dark flows of Maat Mons and the dark summit areas must be explained as different types of lava, which do

not contain the conducting phase. Low emissivity in uplifted areas occurs when erosion uncovers fresh materials containing the iron sulfide. This model again leaves us wondering what the nonconductive weathering product is. While nearly workable, this model is not quite as satisfying as the model where the conductive mineral is created by weathering.

There is much room for work in this area. Measurements of the dielectric constants of real loaded dielectric rocks would help us to decide if Kelly's experiments with paraffin, and the Clausius-Mosotti relation (equation 4.27), can in fact be extrapolated into geological settings. Better measurements of the conductivities of iron sulfides and oxides, especially if done at Venus surface temperatures, would allow us to decide if there is any advantageous difference between them. Finally, the range of materials under consideration should be expanded if possible; finding a phase transition between a conductive and a nonconductive mineral at approximately 6054 km altitude would solve most of the problems.

Chapter 5

Volume Scattering

5.1 Introduction

In this chapter we explore the possibility that low-emissivity surfaces on terrestrial planets, in particular on Venus, may result from scattering by entities dispersed throughout the subsurface material. This is known in general parlance as *volume scattering.* The term is loosely defined; it is at times applied to any of a number of subsurface scattering phenomena, including scattering by bodies embedded in the surface, scattering by cracks below the surface, and scattering by localized but continuous changes in the dielectric properties of the surface material. Other subsurface phenomena, such as reflection by layers of different composition below the surface, and refraction by continuous changes in dielectric constant with depth, might also be termed volume scattering; however, they are somewhat different in character from the previously mentioned phenomena. In this chapter we will consider only discrete scatterers, such as rocks or bubbles, embedded in the surface material.

The effects of volume scattering on reflection and emission are as follows. For an ordinary surface composed of a homogeneous medium, without any internal scatterers, the only point at which radiation's direction of travel can be changed is the atmosphere-surface interface. Thus, for example, radiation incident on the surface is either reflected at the interface, or is transmitted into the surface and "lost". However, if there are subsurface scatterers, the radiation transmitted into the surface has

a second chance to be reflected; depending on the nature and density of the scatterers, and the properties of the surface medium, this effect may substantially enhance the reflectance of the surface. The situation with emissivity is somewhat similar. In the absence of subsurface scatterers, radiation emitted upward at some distance below the surface may be absorbed between the point of emission and the surface, or reflected back downward at the atmospheric interface; if neither of these occur, the radiation escapes. Internal scatterers, though, add another obstacle, and so tend to reduce the amount of emitted radiation which escapes.

A multitude of theoretical and experimental studies of volume scattering have been done. Most theoretical work refers back to the classic treatise on radiative transfer by Chandrasekhar [8]. A majority of authors work in an optical context—for example, light scattering by interstellar dust, by clouds, or by particles suspended in liquids. At optical frequencies, the primary consideration is the scattering, reflection, and absorption of incident light. At lower frequencies (infrared and radio), the effects of volume scattering on the emission properties of the medium are also of interest. The effects of volume scattering on thermal emission have been explored by Conel [12], Emslie and Aaronson [15], England [16, 17], Kong and colleagues [72, 66, and others], Lumme and Bowell [47], and Hapke [35]. In section 5.2.2, we will expand on the work of Hapke [35].

Volume scattering has been applied in a number of situations in planetary science. Scattering and reflection from planetary rings, for example, is naturally treated by radiative transfer and Mie scattering theory (e.g. [14]). Applications in the field of planetary atmospheres are numerous. The use of volume scattering to explain properties of planetary surfaces, though, is more recent. Goldstein and Green [28] explain the unusual radar reflectivity of Ganymede by an ice surface containing a large number of randomly-oriented subsurface ice-vacuum interfaces (that is, cracks). England [17] and Keihm [40] both discuss the effect of volume scattering on the lunar microwave brightness temperature, finding that the brightness temperature can be lowered by a measurable amount. Most recently, Tryka and Muhleman [71] invoke a volume scattering model to explain high reflectivities and low emissivities in Alpha

Regio on Venus. The model of Tryka and Muhleman is discussed in more detail below.

A quite logical question to ask is why in some cases do we treat a material with inclusions with an effective medium theory (such as the loaded dielectrics of the last chapter), and in other cases treat a material with inclusions with volume scattering theory? In general, the difference is one of scale. Effective medium theory is generally applied to media where the inhomogeneities are small on the scale of a wavelength, and where the particles may lie relatively close together, and thus affect each other's scattering characteristics. Volume scattering theory is applied to all sizes of scatterer, but in situations where each scatters independently from the others; thus the scatterers must be further apart. The traditional division of the field of an oscillating source into near ($r \ll \lambda$), intermediate ($r \sim \lambda$), and far ($r \gg \lambda$) zones is the usual measure of the independence of the scatterers. Unfortunately, there is still a largely unexplored gray area between the effective medium and volume scattering regimes; until it is better understood, we must tread in this area with some caution.

5.2 Theory

In this section we will examine some theoretical models of volume scattering. First we briefly review the standard radiative transfer model of an isotropically-scattering atmosphere [8], and the derivation of its emissivity made by Tryka and Muhleman [71]. Similar results are obtained by Hapke [35]. We then derive an improved expression for the emissivity of a half-space containing isotropic scatterers. The derivation of this expression parallels the derivation by Hapke [35], with a few simplifications; however, our derivation takes into account both the effects of the loss in the surface medium between scatterers, and the effects of the dielectric discontinuity at the surface-atmosphere boundary.

5.2.1 Emissivity of Isotropically Scattering Atmosphere

The usual approach to solving the problem of the emissivity of a scattering layer employs traditional radiative transfer theory. Chandrasekhar [8] solves the problem

of scattering from a semi-infinite scattering layer for certain simple forms of the particle phase function. The basic solution assumes that there is no dielectric interface at the boundary of the half-space containing the scatterers, and that the material between the scatterers is lossless. The density of scatterers is not specified, and is not important as long as far-field approximations apply. Polarization is not a consideration in this solution.

The simplest phase function is the phase function for isotropic scattering,

$$P(\phi) = \text{constant} = \varpi_0. \tag{5.1}$$

ϖ_0 is the single scattering albedo, the fraction of radiation intercepted from the incident beam by the particle which is scattered into other directions. (The remaining fraction of intercepted radiation is absorbed.) The law of diffuse reflection from a half-space of isotropic scatterers is given as follows. Imagine a parallel beam of radiation with power πF per unit area normal to itself, incident on a semi-infinite layer of isotropic scatterers with single scattering albedo ϖ_0, at an angle ϕ_0 to the surface normal. The intensity of radiation scattered into an angle ϕ to the surface normal, independent of azimuthal direction, is given by ([8, chap. V, eqn. 109])

$$I(\mu, \mu_0) = \frac{1}{4}\varpi_0 F \frac{\mu_0}{\mu + \mu_0} H(\varpi_0, \mu) H(\varpi_0, \mu_0), \tag{5.2}$$

where $\mu_0 = \cos(\phi_0)$, $\mu = \cos(\phi)$, and the H functions for isotropic scattering are tabulated by Chandrasekhar [8, table XI]. These functions are given approximately by

$$H(\varpi_0, x) = \frac{1 + 2x}{1 + 2x\sqrt{1 - \varpi_0}}, \tag{5.3}$$

which is everywhere accurate to within 4 per cent [35].

From equation 5.2, Tryka and Muhleman [71] derive the emissivity as a function of ϕ. The method is the same as is described in section 2.2.1. We imagine the scattering half-space to be at thermodynamic equilibrium in an isothermal cavity. The isotropic radiation intensity inside the cavity is B_{nu}. Thermodynamic equilibrium requires that

the intensity of radiation incident on the surface B_{nu} at angle ϕ be equal to the sum of what is emitted by the surface at angle ϕ and what is reflected into direction ϕ from all directions:

$$B_\nu = e(\mu)B_\nu + \frac{\varpi_0}{4\pi}H(\mu)\int_0^{2\pi}\int_0^1 \frac{\mu_0 B_\nu H(\mu_0)}{\mu+\mu_0}\,d\mu_0\,d\theta \tag{5.4}$$

Integrating over θ and rearranging,

$$e(\mu) = 1 - \frac{\varpi_0}{2}H(\mu)\int_0^1 \frac{\mu_0 H(\mu_0)}{\mu+\mu_0}d\mu_0 \tag{5.5}$$

[71, eqn. 6]. This last integral is solved with the help of Chandrasekhar [8, chap. 5, eqns. 14 and 108], and the result is

$$e(\mu) = \sqrt{1-\varpi_0}H(\mu). \tag{5.6}$$

The same effective result is obtained by Hapke [35]; incorporating his expression for $H(\mu)$,

$$e(\mu) = \sqrt{1-\varpi_0}\frac{1+2x}{1+2x\sqrt{1-\varpi_0}}. \tag{5.7}$$

Figure 5-1 shows the emissivity given by equation 5.6 as a function of angle for various values of ϖ_0.

5.2.2 Emissivity of a Bounded Lossy Medium Containing Isotropic Scatterers

Here we will derive a new expression for the emissivity of a half-space containing isotropic scatterers. This derivation parallels one by Hapke [35]. We will incorporate a few simplifications, such as a uniform temperature profile with depth and isotropic scattering; however, our derivation will take into account both the loss in the surface medium between scatterers, and the dielectric discontinuity at the surface-atmosphere boundary.

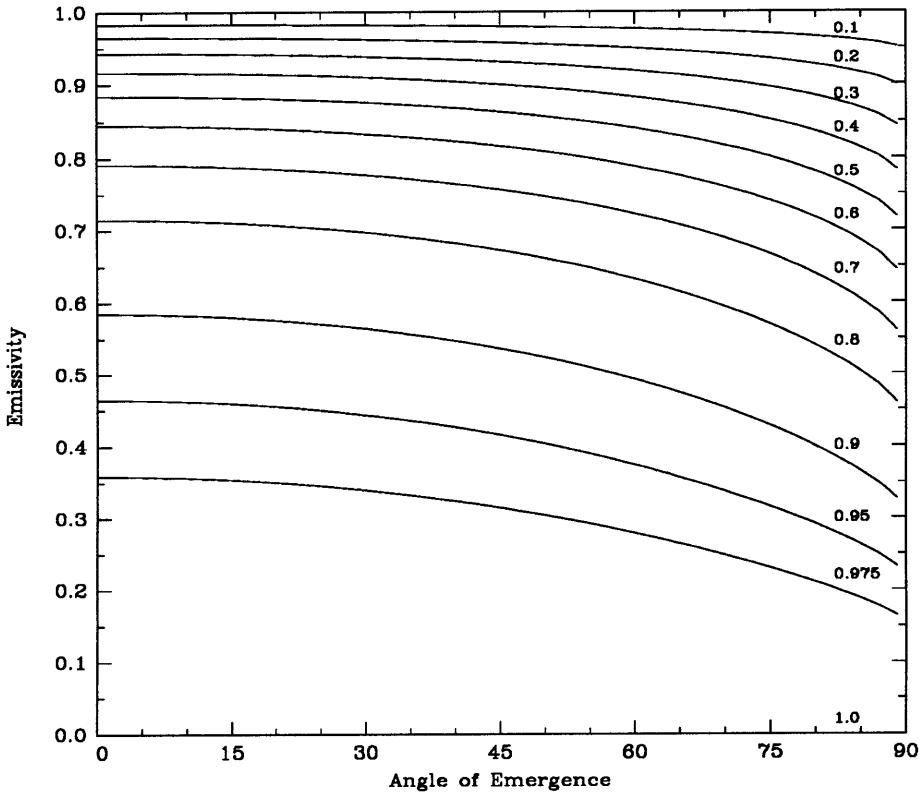

Figure 5-1: Theoretical emissivity of an isotropically-scattering atmosphere (equation 5.6), for various values of the single scattering albedo, ϖ_0 (shown near curve). For $\varpi_0 = 1.0$, the atmosphere is perfectly reflecting and the emissivity is 0.

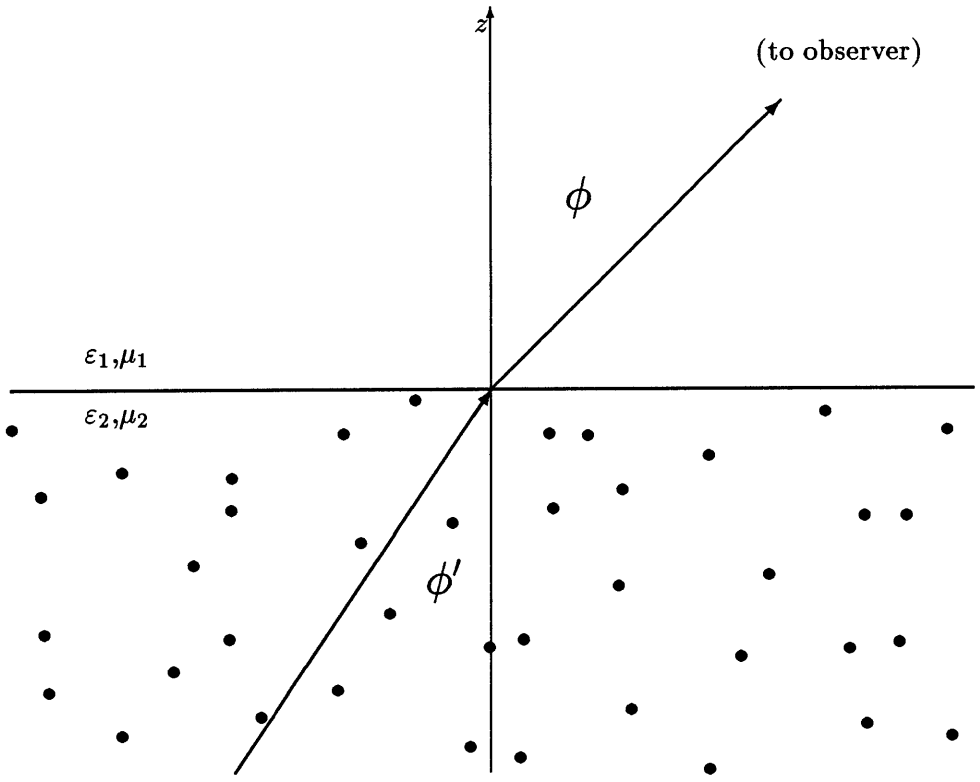

Figure 5-2: Geometry of a bounded lossy medium containing isotropic scatterers.

Properties of the Surface

The geometry of the problem is show in Figure 5-2. The hypothetical observation of surface emission will be carried out at a frequency ν, and all frequency-dependent parameters will be determined accordingly. The surface medium has a constant and uniform physical temperature T. The sky is considered to be cold and dark, contributing negligible radiation to the system. The atmosphere has relative permittivity ε_1 and relative permeability μ_1; the surface medium has relative permittivity ε_2 and relative permeability μ_2. The surface is viewed at an angle ϕ from the surface normal. Note that the direction of travel is deflected at the surface boundary, due to the refraction. The angle between the direction of travel and the internal surface normal is ϕ', and is given by Snell's law (equation 4.22).

Below the surface are isotropic scatterers. Each different type of scatterer i is characterized by its number density N_i, its average geometric cross section $C_{geo\,i}$, and

its extinction, scattering, and absorption efficiencies, $Q_{ext\,i}$, $Q_{sca\,i}$, and $Q_{abs\,i}$, respectively. The net extinction, scattering, and absorption coefficients of the collection of scatterers are, respectively,

$$E_s = \sum_i N_i\, C_{geo\,i}\, Q_{ext\,i}, \tag{5.8}$$

$$S_s = \sum_i N_i\, C_{geo\,i}\, Q_{sca\,i}, \tag{5.9}$$

$$A_s = \sum_i N_i\, C_{geo\,i}\, Q_{abs\,i}. \tag{5.10}$$

These quantities have units of inverse length, and may be interpreted either as the net cross section per unit volume, or as the extinction, scattering, or absorption per unit distance travelled by an electromagnetic wave. Note that since $Q_{ext\,i} = Q_{sca\,i} + Q_{abs\,i}$, $E_s = S_s + A_s$.

The average particle single scattering albedo ϖ_s is

$$\varpi_s = S_s/E_s. \tag{5.11}$$

To take into account the loss of the medium, we may calculate the power attenuation coefficient of the medium by

$$\alpha_P = 2\alpha_2 = 2\mathrm{Re}\left\{\gamma_2^*\right\} = 2\mathrm{Re}\left\{i2\pi\nu\sqrt{\varepsilon_2^*\mu_2^*}\right\} \tag{5.12}$$

(section 4.2.3). This represents a purely absorptive extinction per unit length, or cross section per unit volume. The power attenuation coefficient may be added directly to the net particle extinction and absorption coefficients, to give the effective coefficients

$$E = E_s + \alpha_P, \tag{5.13}$$

$$S = S_s, \tag{5.14}$$

$$A = A_s + \alpha_P. \tag{5.15}$$

Note again that $E = S + A$.

The net emission coefficient of the medium F is necessarily equal to the absorption coefficient:

$$F = A. \tag{5.16}$$

The effective average single scattering albedo in the medium, ϖ_0, is given by

$$\varpi_0 = S/E, \tag{5.17}$$

and the effective average emissivity e_0 is

$$e_0 = F/E = 1 - \varpi_0 = \gamma^2; \tag{5.18}$$

γ is the albedo factor:

$$\gamma = \sqrt{1 - \varpi_0}. \tag{5.19}$$

Emissivity Including Refraction and Reflection at the Surface

The quantity to be calculated is the emissivity of the surface as a function of observation angle, $e(\phi)$. If $I_{obs}(\phi)$ is the observed intensity, we may calculate the emissivity by comparing this intensity to B_ν, the intensity we would expect to observe from a blackbody at the known surface temperature:

$$e(\phi) = I_{obs}(\phi)/B_\nu. \tag{5.20}$$

We will denote by $I(z, \phi')$ the upward specific intensity below the surface as a function of depth, in direction ϕ'; the upward intensity just below the surface will be $I(0, \phi')$. Part of the upward radiation just below the surface will be reflected by the surface/atmosphere interface, and the rest will be transmitted into the direction of the observer. Let the Fresnel reflection coefficients for radiation incident on the interface from *below* the surface be $R'_\perp(\phi')$ and $R'_\parallel(\phi')$ for horizontal and vertical polarizations, respectively; these are calculated from equations 4.19 and 4.20. The

observed emissivity in each polarization will be:

$$e_\perp(\phi) = \frac{I(0,\phi')}{B_\nu}(1 - R'_\perp(\phi')), \tag{5.21}$$

$$e_\parallel(\phi) = \frac{I(0,\phi')}{B_\nu}(1 - R'_\parallel(\phi')). \tag{5.22}$$

The next task is to find an expression for $I(z,\phi')$ and thus $I(0,\phi')$.

Equation of Radiative Transfer

As a beam of radiation travels through the medium, three things may change its intensity. First, it may be attenuated by the medium, through scattering or absorption. Second, radiation travelling in other directions may be scattered into the direction of the beam and add to it. Third, radiation may be emitted by the medium into the direction of the beam. The equation of radiative transfer is thus

$$\frac{dI(r,\phi')}{dr} = -EI(r,\phi') + \frac{1}{4\pi}\int_{4\pi} S\, I(r,\Omega')\, d\Omega' + e_0 E B_\nu \tag{5.23}$$

where r is measured in the direction of travel of the beam. In this equation we have incorporated assumptions of isotropic scattering and emission.

It will be helpful to express distance in terms of the extinction coefficient E. Let $u = Ez$ be the scale height; then $du = E\,dz = E\,dr\,\cos\phi'$, and the equation of radiative transfer becomes

$$\cos\phi'\,\frac{dI(u,\phi')}{du} = -I(u,\phi') + \frac{\varpi_0}{4\pi}\int_{4\pi} I(u,\Omega')\, d\Omega' + e_0 B_\nu. \tag{5.24}$$

Two-Stream Approximation

In order to solve the equation of radiative transfer, we will use the two-stream approximation to find the integral in the scattering term, then solve the resulting first order equation directly.

Let

$$\Phi(u) = \int_{4\pi} I(u,\Omega')\, d\Omega' \tag{5.25}$$

be the intensity integrated over all directions at some depth u. We can separate $\Phi(u)$ into an upward and a downward component:

$$\Phi(u) = \Phi_U(u) + \Phi_D(u) \tag{5.26}$$

where

$$\Phi_U(u) = \int_{\Omega_U} I(u, \Omega')\, d\Omega', \tag{5.27}$$

$$\Phi_D(u) = \int_{\Omega_D} I(u, \Omega')\, d\Omega'. \tag{5.28}$$

Integrating, we find that the average intensities in the upward and downward directions are $\langle I(u)\rangle_U = \Phi_U(u)/2\pi$ and $\langle I(u)\rangle_D = \Phi_D(u)/2\pi$.

We may integrate equation 5.24 over both the upper and lower hemispheres, substituting the appropriate average values of I:

$$\frac{d\Phi_U(u)}{du} = -2\Phi_U(u) + \varpi_0(\Phi_U(u) + \Phi_D(u)) + 4\pi e_0 B_\nu, \tag{5.29}$$

$$-\frac{d\Phi_D(u)}{du} = -2\Phi_D(u) + \varpi_0(\Phi_U(u) + \Phi_D(u)) + 4\pi e_0 B_\nu. \tag{5.30}$$

Adding these equations gives

$$\frac{d\Delta\Phi(u)}{du} = -2\Phi(u) + 2\varpi_0\Phi(u) + 8\pi e_0 B_\nu, \tag{5.31}$$

and subtracting gives

$$\frac{d\Phi(u)}{du} = -2\Delta\Phi(u), \tag{5.32}$$

where we have made use of the parameter $\Delta\Phi(u) = \Phi_U - \Phi_D$. Differentiating equation 5.32, we get

$$\frac{d^2\Phi(u)}{du^2} = -2\frac{d\Delta\Phi(u)}{du}; \tag{5.33}$$

combining with equation 5.31, we arrive at

$$\frac{d^2\Phi(u)}{du^2} = 4e_0\Phi(u) - 16\pi e_0 B_\nu. \tag{5.34}$$

This is an ordinary second-order differential equation, and may be solved without much difficulty. The boundary conditions are as follows: as u goes to $-\infty$, the radiation field should be isotropic,

$$\Delta\Phi(-\infty) = 0, \tag{5.35}$$

and the intensity equal to the blackbody intensity,

$$\Phi(-\infty) = 4\pi B_\nu. \tag{5.36}$$

At the surface, the average upward and downward intensities are related by $\mathcal{R}'$, the hemispherically-averaged Fresnel reflectivity from the bottom of the surface-atmosphere interface:

$$\Phi_D(0) = \mathcal{R}'\Phi_U(0), \tag{5.37}$$

and thus

$$\Phi(0) = \Phi_U(0)(1 + \mathcal{R}') \tag{5.38}$$

and

$$\Delta\Phi(0) = \Phi_U(0)(1 - \mathcal{R}'). \tag{5.39}$$

$\mathcal{R}'$ is found by performing the integral

$$\mathcal{R}' = \int_0^{\frac{\pi}{2}} \frac{R'_\perp(\phi') + R'_\parallel(\phi')}{2} \sin\phi' \, d\phi'. \tag{5.40}$$

The solution to equation 5.34 with these boundary conditions is

$$\Phi(u) = 4\pi B_\nu \left(1 - \frac{e^{2\gamma u}}{1 + \gamma\frac{(1+\mathcal{R}')}{(1-\mathcal{R}')}}\right). \tag{5.41}$$

Solution of the Radiative Transfer Equation

We may substitute our solution for $\Phi(u)$ into the equation of radiative transfer, equation 5.24:

$$\cos\phi' \frac{dI(u,\phi')}{du} = -I(u,\phi') + \varpi_0 B_\nu \left(1 - \frac{e^{2\gamma u}}{1+\gamma\frac{(1+\mathcal{R}')}{(1-\mathcal{R}')}}\right) + e_0 B_\nu. \tag{5.42}$$

This is a simple first-order differential equation. If as a boundary condition we require that $I(-\infty,\phi') = B_\nu$, the solution is

$$I(u,\phi') = B_\nu \left(1 - \frac{\varpi_0 e^{2\gamma u}}{(1+2\gamma\cos\phi')(1+\gamma\frac{(1+\mathcal{R}')}{(1-\mathcal{R}')})}\right). \tag{5.43}$$

The final solution for the emissivity of the surface is

$$e_\perp(\phi) = \left(1 - \frac{\varpi_0}{(1+2\gamma\cos\phi')(1+\gamma\frac{(1+\mathcal{R}')}{(1-\mathcal{R}')})}\right)(1 - R'_\perp(\phi')), \tag{5.44}$$

$$e_\parallel(\phi) = \left(1 - \frac{\varpi_0}{(1+2\gamma\cos\phi')(1+\gamma\frac{(1+\mathcal{R}')}{(1-\mathcal{R}')})}\right)(1 - R'_\parallel(\phi')). \tag{5.45}$$

The average emissivity is

$$e(\phi) = \frac{1}{2}\left(e_\perp(\phi) + e_\parallel(\phi)\right). \tag{5.46}$$

Linear Polarization Ratio

It is not difficult to show that the fresnel reflectivities for radiation incident on the surface from below, $R'_\perp(\phi')$ and $R'_\parallel(\phi')$, are equal to the reflectivities for radiation incident from above, $R_\perp(\phi)$ and $R_\parallel(\phi)$. The polarization ratio is thus given by

$$\frac{e_\parallel(\phi)}{e_\perp(\phi)} = \frac{1 - R'_\parallel(\phi')}{1 - R'_\perp(\phi')} = \frac{1 - R_\parallel(\phi)}{1 - R_\perp(\phi)}. \tag{5.47}$$

Note that this ratio is completely independent of the density or albedo of the scatterers; it depends only on the properties of the material surrounding the scatterers. This is a natural outcome of the assumption of isotropic scattering and emission; however, even for nonisotropic scattering and emission, we might still reasonably expect the polarization ratio to be largely controlled by the fresnel reflectivities of the surface/atmosphere boundary.

Results

The major prediction of this model (and, to be sure, of most volume scattering models) is that low values of emissivity, if produced by volume scattering, require highly efficient scattering in a low-loss medium. Figures 5-3 and 5-4 show the predicted emissivities at normal incidence as a function of the effective single scattering albedo ϖ_0, for several values of the surface dielectric constant. It is clear that for values of dielectric constant corresponding to ordinary solid rock (about 4 and above), ϖ_0 must be extremely high, somewhere above 0.998, to result in emissivities as low as those observed in some areas on Venus. Even much lower values of dielectric constant require a very high value of ϖ_0. Since loss in the medium always tends to reduce ϖ_0 as compared to ϖ_s, perfectly lossless scattering ($\varpi_s = 1.0$) is almost certainly required. Values of ϖ_s near 1.0 can be achieved by three types of scatterer: perfect conductors, lossless materials, or voids.

An example of the model's prediction for the emissivity of a particular scattering layer is shown in figure 5-5. In this example, the atmosphere is approximated by a vacuum ($\varepsilon_1 = 1.0$), the surface material is a low-loss rock of low to intermediate dielectric constant ($\varepsilon_2 = 4.8 - i0.001$), and the scatterers are voids ($\varpi_s = 1.0$, $E_s = 6.585$ m^{-1}). (These parameters correspond to one of a number of surfaces investigated by Monte Carlo techniques, as described below.) The major distinguishing characteristic of the volume scattering emissivity curve is that the emissivity in the vertical polarization does not rise to unity at the Brewster angle, as it does for a smooth Fresnel surface.

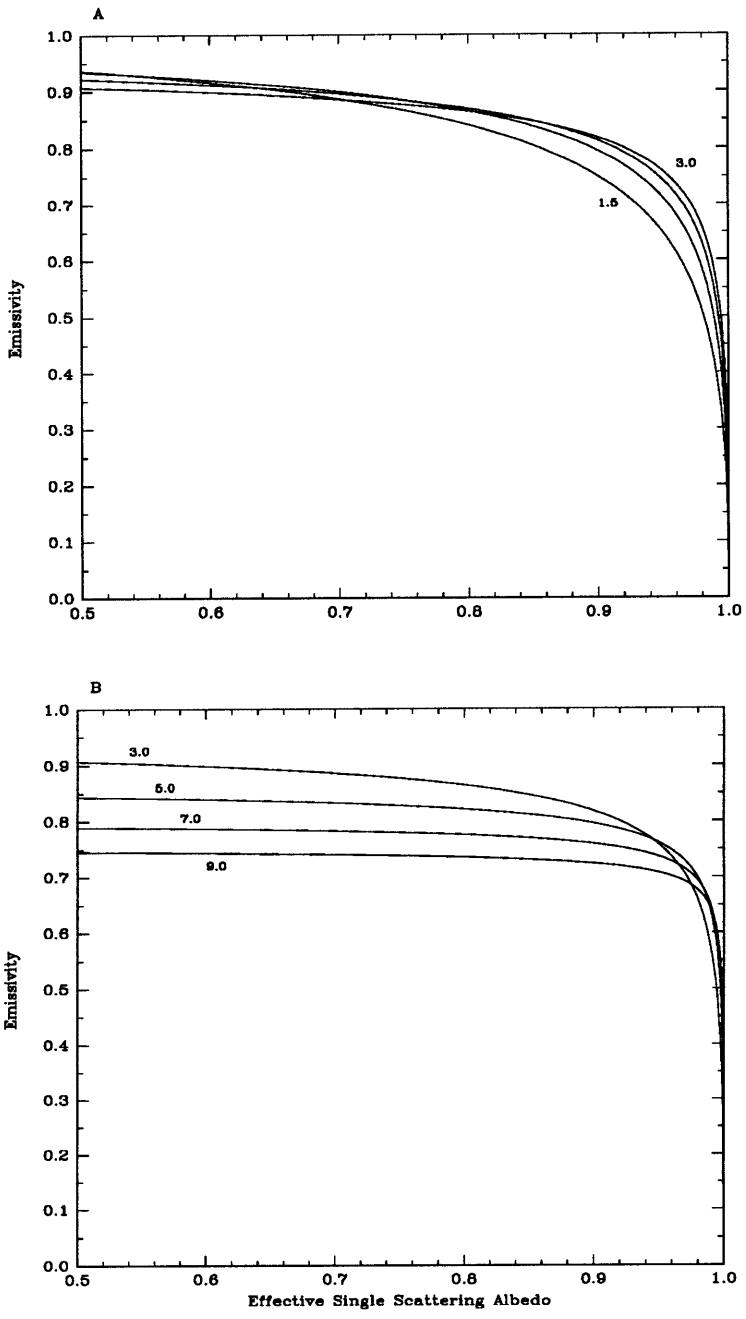

Figure 5-3: Theoretical predictions of emissivity as a function of effective single scattering albedo ($\varpi_0 = 0.5$ to 1.0) for various dielectric constants of surface material. Values of dielectric constant are (A) $\varepsilon = 1.5$, 2.0, 2.5, 3.0; (B) $\varepsilon = 3.0$, 5.0, 7.0, 9.0.

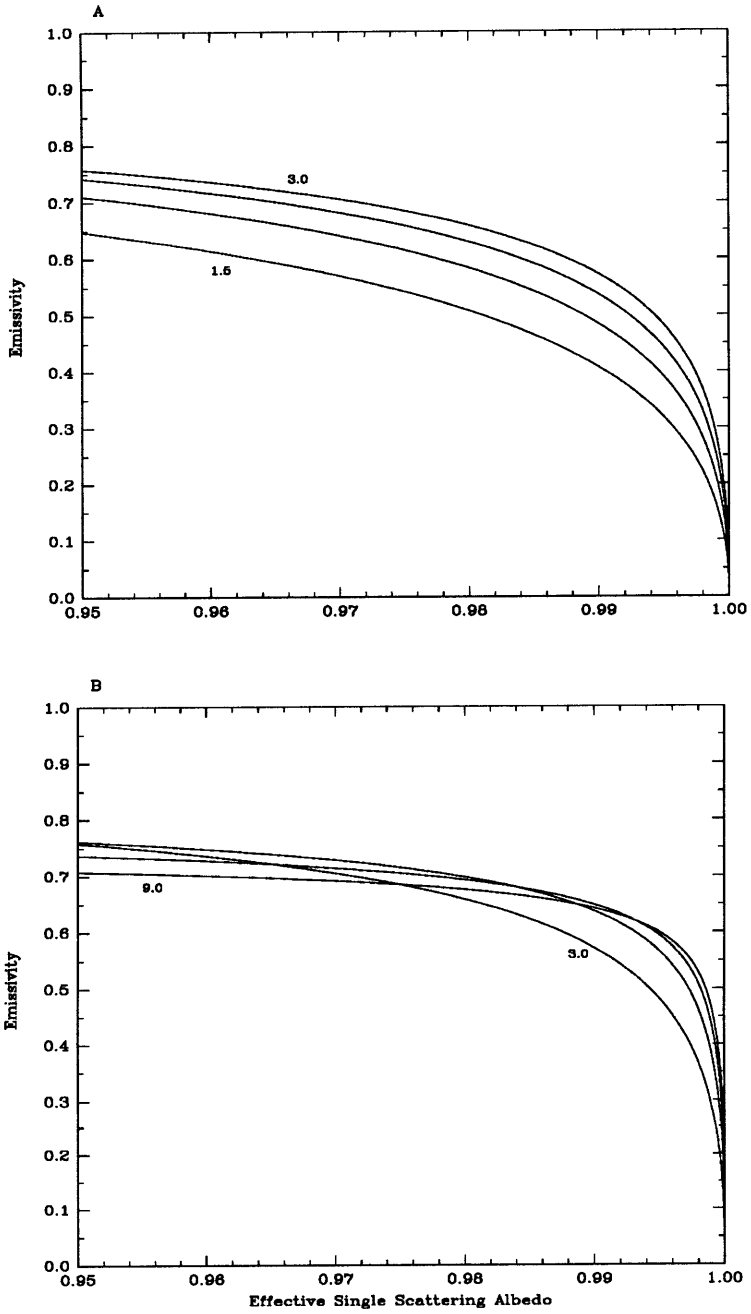

Figure 5-4: Theoretical predictions of emissivity as a function of effective single scattering albedo ($\varpi_0 = 0.95$ to 1.0) for various dielectric constants of surface material. Values of dielectric constant are (A) $\varepsilon = 1.5$, 2.0, 2.5, 3.0; (B) $\varepsilon = 3.0$, 5.0, 7.0, 9.0. (Curves are identical to those in figure 5-4.)

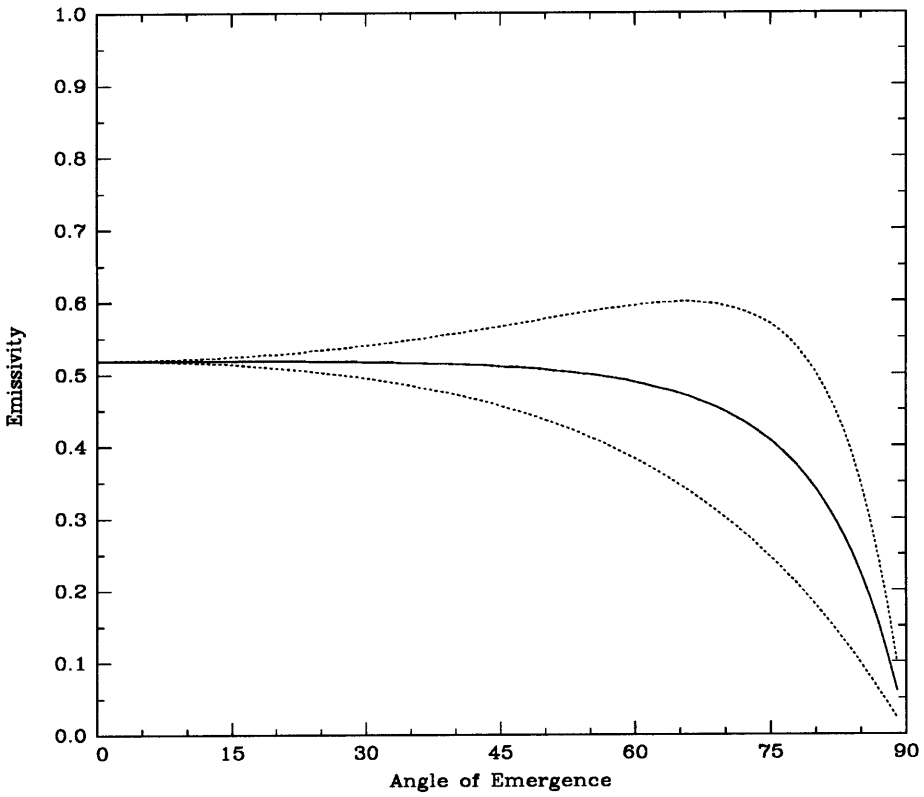

Figure 5-5: Theoretical prediction of the emissivity of a scattering layer. Curves are (dotted, upper) vertical polarization, (dotted, lower) horizontal polarization, (solid) average. Model parameters: atmosphere: $\varepsilon_1 = 1.0$; surface: $\varepsilon_2 = 4.8 - i0.001$; scatterers: $\varpi_s = 1.0$, $E_s = 6.585$ m^{-1}.

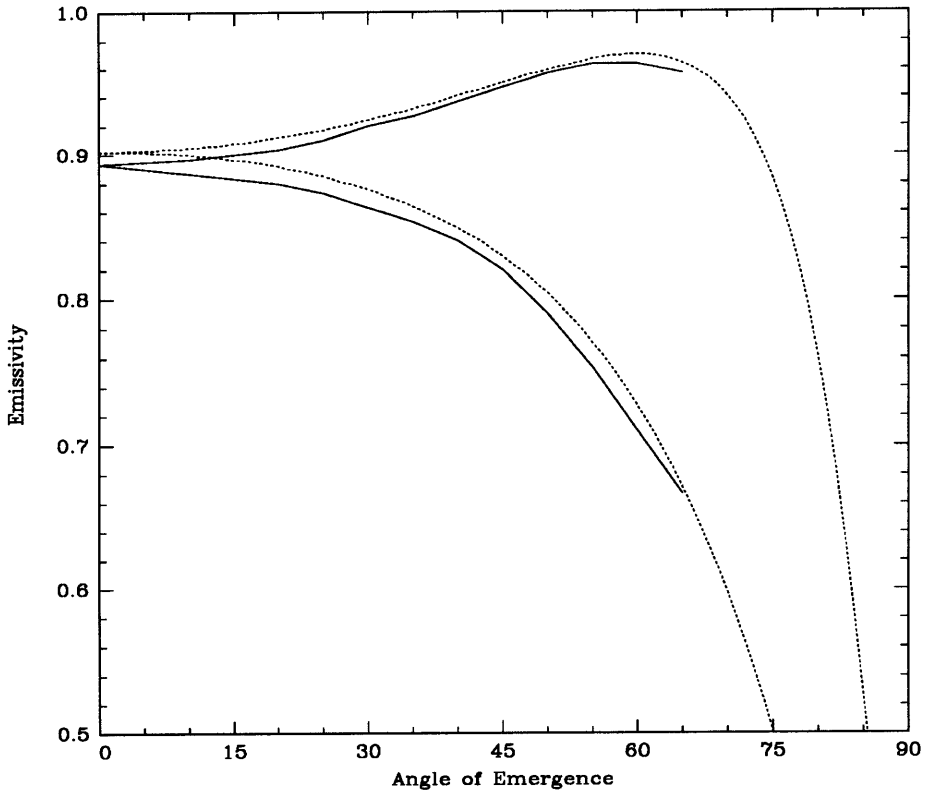

Figure 5-6: Comparison of our theoretical model (dotted lines) to theoretical results of Tsang and Kong for Mie scatterers [72, Fig. 9] (solid lines). Surface contains scatterers of radius 5 mm, occupying 3% of the volume; scatterers are lossless, with dielectric constant 8.3; matrix material has permittivity $3.0 - i0.0159$. Radiation frequency is 5 GHz.

Comparison to Similar Work

It should be noted that the emissivity of a bounded, lossy layer containing scatterers has previously been investigated by England, for isotropic [16] and Rayleigh [17] scatterers, and by Tsang and Kong for Mie scatterers [72]. The main advantage of the result above over these previous works is its simplicity of form and relative ease of use. Figure 5-6 compares data from Fig. 9 of Tsang and Kong [72] to results obtained from the above model. In this particular case, the results are very similar; this is not surprising, as the particular Mie particle size used in this example is small enough to be largely isotropic in its scattering properties.

It should also be noted that if the matrix material and atmosphere material are the same, then there is no dielectric boundary at the top of the scattering layer; $R'_{\perp}(\phi') = R'_{\parallel}(\phi') = 0$, $\mathcal{R}' = 0$, $\phi' = \phi$, and (with a little algebraic manipulation) equation 5.46 reduces to the expression for an isotropic atmosphere, equation 5.7.

5.3 Monte-Carlo Simulations of Scattering Layers

To supplement the theoretical treatment of volume scattering, the emissivities of several types of scattering layers were studied by means of a Monte-Carlo simulation. The general idea of the simulation is to illuminate a unit area of the hypothetical surface uniformly from above, as would occur in a blackbody cavity, and to record the pattern of reflected radiation which is reflected back up again, thereby obtaining the hemispherical-directional reflectivities and (by equation 2.10) emissivities. In the simulation, radiation is quantized into individual rays, which are followed as they encounter various obstacles and are scattered or absorbed. The ray optics approximation is invalid under certain conditions, for example, when a ray encounters a scatterer whose dimensions are of the order of, or smaller than, the radiation wavelength. Encounters with scatterers are resolved by wave mechanics (specifically, Mie scattering theory—see Appendix A), which is used to calculate the scattering and absorption cross sections and the probability distribution function for the direction of the scattered ray. The direction of linear polarization of the rays is followed, also; electrical phase information is not kept (the radiation is assumed incoherent).

5.3.1 Specification of Surface

The geometry of the surface being simulated is shown in Figure 5-7. At the top is the atmosphere. All radiation originates in the atmosphere, and if it returns there, is considered to have escaped. The atmosphere is characterized by its permittivity and permeability (in all cases discussed in this paper, the atmosphere is treated as vacuum). Loss in the atmosphere is ignored. The lowest layer is called the base layer. Radiation which enters the base layer is considered to have been absorbed by the

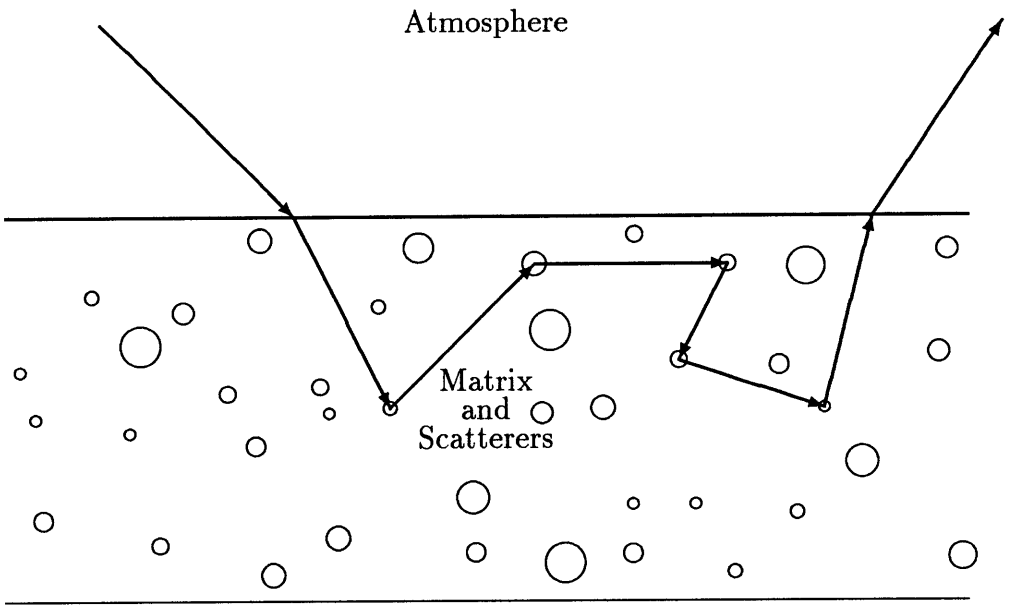

Figure 5-7: Layer geometry in scattering simulation.

surface. The base is also characterized by its permittivity and permeability.

The interesting layer is the middle layer. This layer consists of a homogeneous material, called the matrix material, which may contain an assortment of scatterers. The matrix material is characterized by its permittivity and permeability. Scatterers are of two general classes: isotropic point scatterers, and spherical Mie scatterers. Isotropic point scatterers are specified by their single scattering albedo and by the mean distance between them (equivalently, their cross section density). Spherical scatterers are specified by their radius, their number density, and the permittivity and permeability of the material. Any (finite) number of different types of scatterers are allowed; thus, for example, the scattering from a layer containing a discrete

distribution of particle sizes can be studied.

Scatterers are not handled as individual entities; that is, we do not keep a long list of the locations and properties of all the scatterers under the surface. This can be done in principle, but in practice, the search for the intersection of a ray with each scatterer is a computational nightmare. Rather, the scatterers are encountered with a certain probability per unit length, whose value is determined by their cross section and number density. The method is explained below.

5.3.2 Illumination

Except when otherwise specified, the frequency of the illuminating radiation is 2.385 GHz, the frequency of the Magellan radar. The frequency-dependent properties of materials in the simulation must correspond to this frequency.

Illumination may either come from a particular direction (useful mainly in calculating bidirectional reflectance) or from the entire sky (useful in calculating emissivity). The polarization may be horizontal, vertical, or random. In this work we are concerned mainly with emissivity; thus the illumination is of random polarization, and from the entire sky.

5.3.3 Encounters with Interfaces between Media

The interfaces between the atmosphere and matrix, and between the matrix and base, are considered to be flat and smooth; thus the scattering obeys Fresnel's laws (section 4.2.4). On encountering an interface, the following steps are taken. First, the polarization vector is resolved into horizontal and vertical components. Then, the ray is "collapsed" into either purely horizontal or purely vertical polarization. The probability of becoming one or the other is based on the relative power in the two orthogonal modes. Once the direction of polarization is established, the Fresnel reflection coefficient is calculated and the ray is either reflected or transmitted.

5.3.4 Encounters with Scatterers

A ray which encounters an isotropic scatterer is absorbed with probability $1 - \varpi_i$, where ϖ_i is the single scattering albedo of that particle. If not absorbed, the ray is scattered into a random direction with random polarization.

Mie scattering is discussed in Appendix A. A ray which encounters a Mie scatterer is treated as follows. First, it is absorbed with probability Q_{abs}/Q_{ext}, where the efficiencies pertain to the particular scatterer type under consideration (see equations A.25 and A.27). If not absorbed, an azimuthal direction perpendicular to the direction of travel is chosen randomly. The scattering plane is determined by the direction of travel and this azimuthal direction. The polarization of the ray is then resolved into either vertical or horizontal, as was done in encounters with surfaces. Once this is done, the appropriate intensity function (see equations A.11 and A.12), normalized by solid angle, is used as a probability distribution function to choose a direction for the scattered ray.

5.3.5 Dielectric Attenuation

Since rays are quantized, they are not attenuated in the normal sense, but rather are absorbed with a probability based on their distance of travel through the medium and the power attenuation coefficient of the medium (section 4.2). Its reciprocal, the power absorption length, is equivalent to the mean free path for absorption in the medium. The use of this value is described below.

5.3.6 Finding the First Event

As a ray moves through a material, a few different things may happen. It may encounter the top or bottom of the layer, at which point it would undergo a Fresnel scatter as described above. It may be absorbed by the medium. Or, it may encounter a scatterer of any of a finite number of types. Of all the events which might happen, we must decide which one occurs first. Encounters with the top and bottom of the layer are determined geometrically, by the location and direction of the ray. Absorption

and enounters with scatterers, though, must be determined by the probability of their occurrence.

Let L_i be the mean free path between scatterers of type i. For isotropic scatterers, this mean free path is given. For Mie scatterers, it is calculated from the number density and extinction cross section:

$$L_i = \frac{1}{N_i C_{ext\,i}}, \tag{5.48}$$

where $C_{ext\,i}$ is given by equation A.22. Let X_i be the distance that a ray travels before encountering a scatterer of type i. The cumulative probability distribution of X_i is given by the Poisson distribution,

$$P(X_i \leq x) = \int_0^x p(x')dx' = 1 - e^{\frac{x}{L_i}}. \tag{5.49}$$

To randomly choose a value of X_i with the proper probability distribution, we must choose $P(X_i \leq x)$ uniformly on the interval $[0, 1)$ and solve for x [63]. If U is a random number chosen uniformly on $[0, 1)$,

$$X_i = -L_i \ln(1.0 - U). \tag{5.50}$$

In this way, a random distance X_i for an encounter with each type of scatterer may be chosen. Likewise, a random distance X_{abs} for absorption may be chosen using the mean free path for absorption L_{abs}. Finally, the distance to the top or bottom of the layer, X_{lay}, is calculated geometrically. The event which actually occurs is the closest one:

$$X_{event} = \min(X_{lay}, X_{abs}, X_1, X_2, \ldots X_n). \tag{5.51}$$

The ray is moved this distance and the event processed as described in each case above. Then, if the ray has not escaped or been absorbed, we start loop again from the new position.

5.3.7 Statistics and Analysis

The main statistic recorded is the number of rays escaped as a function of direction and polarization. Emissivity may be calculated from the hemispherical-directional reflectance $R_{hd}(\phi)$, as per equation 2.10. If N_{tot} is the number of rays incident on the surface, the isotropic radiation intensity in the hypothetical blackbody cavity is

$$B_\nu = \frac{N_{tot}}{\pi}. \tag{5.52}$$

The intensity of radiation scattered by the surface into a direction at an angle ϕ from the surface normal is

$$B_{sca}(\phi, sky) = \frac{N(\phi)}{\Omega(\phi)\cos(\phi)}, \tag{5.53}$$

where $N(\phi)$ is the number of rays observed to emerge at angle ϕ from the surface normal into a solid angle $\Omega(\phi)$ (integrated over all azimuth angles). By application of equation 2.7, the hemispherical-directional reflectance is

$$R_{hd}(\phi) = \frac{B_{sca}(\phi, sky)}{B_\nu}. \tag{5.54}$$

This may be applied to each polarization separately, replacing B_ν by $B_\nu/2$.

5.3.8 Results

Results for a number of different scattering layers are presented in the next section. A typical case is illustrated in figure 5-8. This simulation corresponds to the example theoretical curve in section 5.2.2 (compare it to figure 5-5). The surface material is a low-loss rock of low to intermediate dielectric constant ($\varepsilon_2 = 4.8 - i0.001$), and the scatterers are spherical voids in the size range 1–10 cm ($\varpi_s = 1.0$, $E_s = 6.585$ m^{-1}. Note that the emissivities are somewhat higher than those predicted by the isotropic scattering model. We will return to this point below.

Figure 5-9 shows the standard error range in emissivity in each polarization, for the above example. In this case, 500,000 rays were followed. In cases where the loss

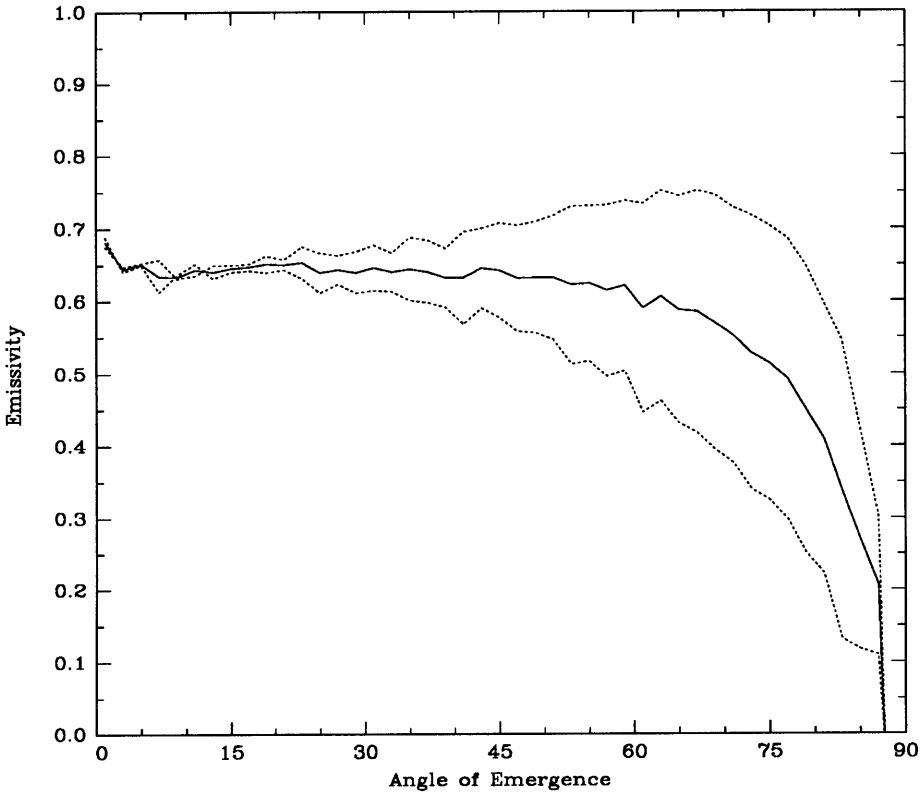

Figure 5-8: Monte-Carlo prediction for the emissivity of a scattering layer. Curves are (dotted, upper) vertical polarization, (dotted, lower) horizontal polarization, (solid) average. Model parameters: atmosphere: $\varepsilon_1 = 1.0$; surface: $\varepsilon_2 = 4.8 - i0.001$; scatterers: 1–10 cm, 25% by volume, $\varepsilon_s = 1.0$. 500,000 rays were traced.

in the matrix is much lower, computation time prevented the simulation of so many rays, and we expect the errors to be somewhat greater. The error bars, however, are never large enough to be of any great concern, for our purposes.

Figure 5-10 compares data from Fig. 9 of Tsang and Kong [72] to the emissivity curve produced by the scattering simulation for the same materials and scatterer population. In theory the curves should be identical. The emissivity of the simulation, though, is consistently 0.03 higher than that of Tsang and Kong. We will not further pursue the cause of this disparity, but will simply note that there is a difference in the results predicted by the two methods.

5.4 Results and Analysis

In this section we will first revisit Tryka and Muhleman, and discuss their model of a low emissivity surface on Venus. It will be seen that the particular materials they selected cannot explain the lowest emissivities observed by Magellan. However, by lowering the dielectric constant of their matrix material, or by decreasing the loss factor in their matrix and scatterers, lower values of emissivity can be reached. We will then consider ordinary materials containing bubbles, and will see how much the loss factor of these materials must be lowered in order to satisfy the observations. Finally, we discuss whether any of the hypothetical surfaces which display sufficiently low emissivity are physically realizable.

5.4.1 Tryka and Muhleman Surfaces

Tryka and Muhleman [71] investigate (theoretically) the properties of a low-loss soil containing spherical scatterers made of ordinary rock materials. Their soil has a dielectric constant of 2 and an absorption length of about 2.5 m, and thus a relative permittivity of $\varepsilon = 2.0 - i0.0113$. This permittivity is consistent with measurements of the permittivities of powdered rocks at density 1.0g/cm^3 made by Campbell and

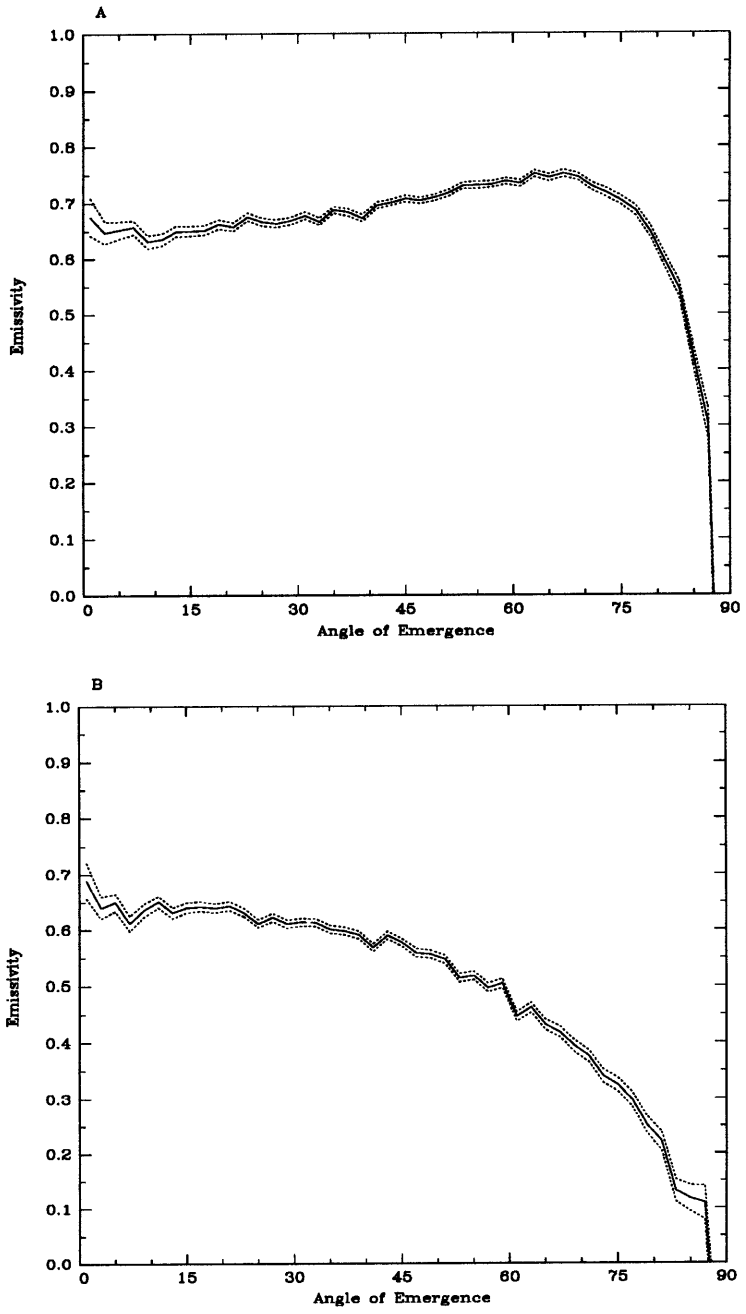

Figure 5-9: Range of standard errors for Monte-Carlo prediction of the emissivity of a scattering layer: vertical polarization (A) and horizontal polarization (B). Dotted curves show variation of one standard deviation in each direction. Parameters of simulation are as in figure 5-8.

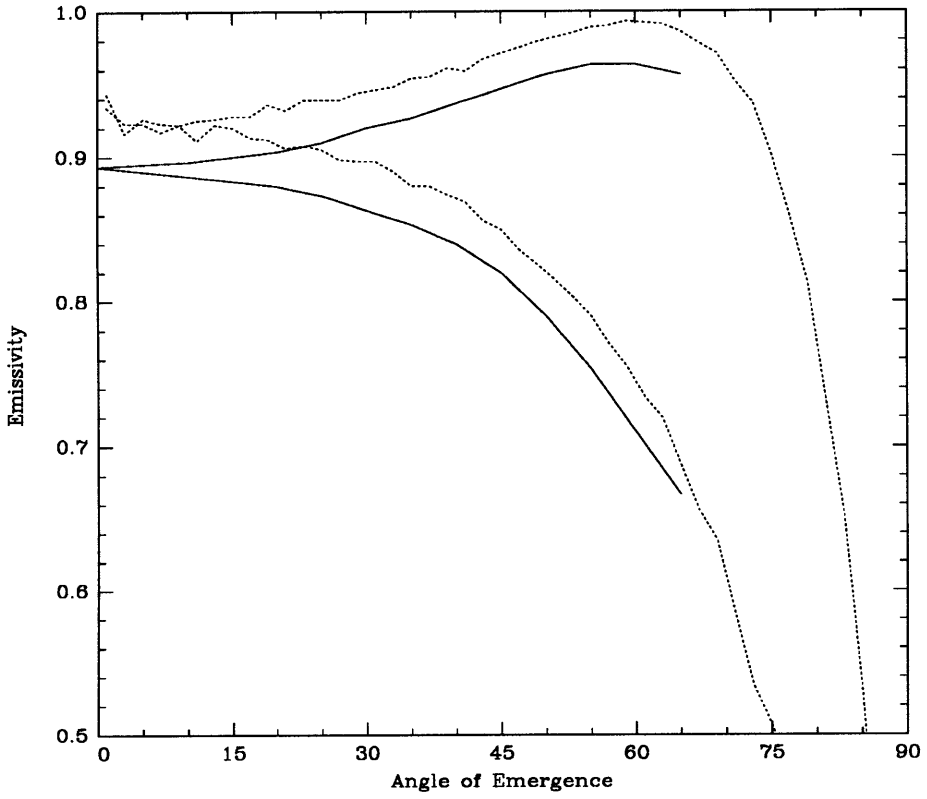

Figure 5-10: Comparison of our simulation results (dotted lines) to theoretical results of Tsang and Kong for Mie scatterers (solid lines) [72, Fig. 9]. Surface contains scatterers of radius 5 mm, occupying 3% of the volume; scatterers are lossless, with dielectric constant 8.3; matrix material has permittivity $3.0 - i0.0159$. Radiation frequency is 5 GHz.

Ulrichs [5]. The composition of the scatterers is also obtained from Campbell and Ulrichs; Tryka and Muhleman average data for basalts and granites, and find a permittivity of $\varepsilon = 5.5 - i0.075$ for an average granite and $\varepsilon = 7.5 - i0.145$ for an average basalt.

Tryka and Muhleman then use Mie scattering theory to compute the average single scattering albedoes for populations of scatterers. The size distribution is given by a power law of the form $N(a) \propto a^{-q}$, where a is the particle radius, and q is either 2 or 3; the upper size cutoff is varied from 5 cm to 100 cm. The maximum computed value of $\varpi_s = 0.974$ is for a population of granite spheres with $q = 3$ and maximum radius 5 cm.

When viewed in light of the theoretical expression they derived for the emissivity of an isotropically-scattering atmosphere (equation 5.6 and figure 5-1), it appears that a single scattering albedo of this magnitude can result in very low emissivities. Putting the value $\varpi_0 = 0.974$ into equation 5.7 yields a normal-incidence emissivity of 0.37. Tryka and Muhleman interpret this as encouraging evidence that low emissivities in certain regions on Venus could be caused by common rocks embedded in dry soils.

Unfortunately, the results are not so encouraging when we take into account the surface/atmosphere interface and the loss in the matrix medium. If we ignore the loss in the medium (which we know would only reduce the effective single scattering albedo and increase the emissivity), the normal-incidence emissivity calculated from equation 5.46, given $\varpi_0 = 0.974$, is $e = 0.62$. Figure 5-11 shows the emissivity as a function of viewing angle for this surface.

To take into account loss in the medium, we must know the density and cross sections of scatterers. For density, we adopt a volume filling fraction of 0.25, noting that it is rather high and thus can serve as an upper limit on the effects the scatterers will have. The cross sections must be computed from Mie theory. We recalculate the scattering properties of a population of granite spheres with $N(a) \propto a^{-3}$ and a maximum size of 5 cm. Our calculations give an average single scattering albedo $\varpi_s = 0.949$ (lower than the value computed by Tryka and Muhleman) and extinction

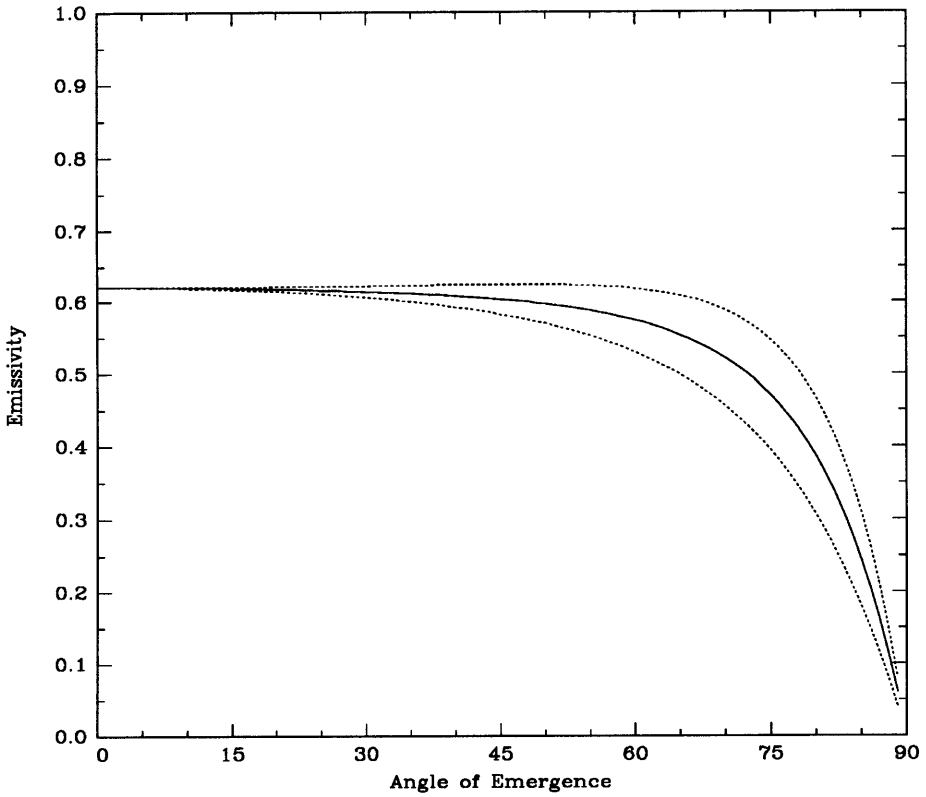

Figure 5-11: Theoretical prediction of emissivity of lossless surface with dielectric constant 2.0 and scatterers with $\varpi_s = 0.974$. Curves are (dotted, upper) vertical polarization, (dotted, lower) horizontal polarization, (solid) average.

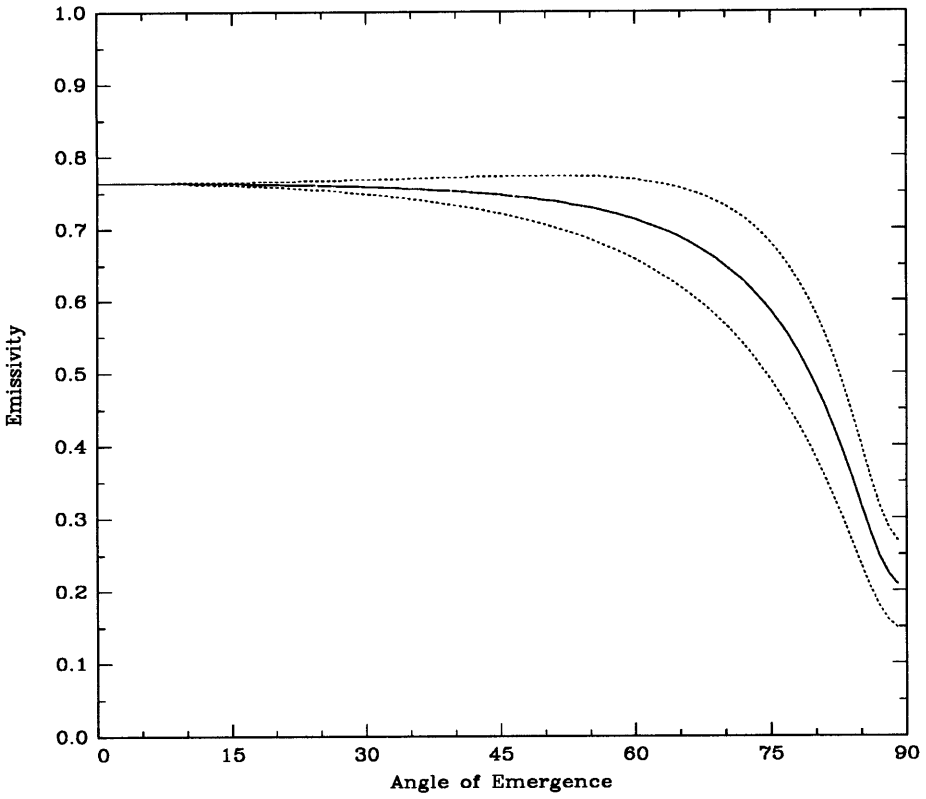

Figure 5-12: Theoretical prediction of emissivity of surface with permittivity $2.0 - i0.0113$, containing granite spheres ($\varepsilon_s = 5.5 - i0.075$) with continuous radius distribution in range 0–5 cm, which occupy 25% of subsurface volume. Curves are (dotted, upper) vertical polarization, (dotted, lower) horizontal polarization, (solid) average.

coefficient $E_s = 12.41$ m^{-1} at filling fraction 0.25. Note that $A_s = \varpi_s E_s = 0.63$ m^{-1}; this is of the same order as $\alpha_P = 1/(2.5 \text{ m}) = 0.4$ m^{-1}, meaning that absorption by the scatterers and loss in the matrix medium are of similar magnitude. The effective single scattering albedo in the medium is $\varpi_0 = 0.920$, and the normal-incidence emissivity calculated from equation 5.46 is $e = 0.76$. Figure 5-12 shows the emissivity as a function of viewing angle for this surface.

We have also investigated the properties of surfaces of this type by means of the Monte Carlo simulation described in section 5.3. Four different size ranges for each type of scatterer (basalt and granite) were investigated. Results are presented in tables 5.1 and 5.2. The data in these tables is as follows. Parameters (specified and

calculated) of the model include:

- The matrix permittivity (in this case, $\varepsilon = 2.0 - i0.0113$).
- The matrix power absorption coefficient, α_P.
- The scatterer permittivity ($\varepsilon = 5.5 - i0.075$ for granite, $\varepsilon = 7.5 - i0.145$ for basalt).
- The scatterer size range. Ten to twenty different sizes of scatterer in this range were used. The number density of each type of scatterer was computed using $N(a) \propto a^{-3}$.
- The volume fraction of scatterers in the matrix (25% in all cases).
- The net extinction coefficient of the scatterers, E_s.
- The net absorption coefficient of the scatterers, A_s. This may be compared to α_P to gauge the relative importance of absorption by the scatterers and by the medium.
- The average particle single scattering albedo, ϖ_s.
- The scattering layer depth (50 m in all cases).
- The effective extinction coefficient, E.
- The effective single scattering albedo, ϖ_0.

Results of the simulation are:

- Total fraction of rays in simulation which escaped back to the atmosphere. We further subdivide this into those which were reflected back upward at their initial encounter with the atmosphere/surface interface, and those which escaped after subsurface scattering, thus providing an indication of the importance of volume scattering in the model.

- Total fraction of rays in simulation which were absorbed. This is subdivided into those which were absorbed in the matrix material, by scatterers, and by the base layer. This provides another indication of the relative importance of absorption by scatterers and by the medium. Because of the thickness of the scattering layer relative to the absorption length in the layer, rays very rarely reach the base layer.

- Normal incidence emissivity. This value is computed by fitting a straight line to the calculated emissivity curve, for angles less than 30°.

The final items in the table are the theoretical normal-incidence emissivity based on equation 5.46, for the given matrix permittivity and effective single scattering albedo, and the normal-incidence fresnel emissivity of the matrix material (no volume scattering).

The net particle single scattering albedoes calculated for the particle size distributions used in the simulation are slightly lower than those quoted by Tryka and Muhleman; the size distributions are somewhat different, however, and we use a limited number of particle sizes, rather than calculating a continuous distribution. Because of the discrete size constraint, we tend to obscure the effects of the Mie resonance peak, where the particle single scattering albedo reaches its maximum.

The emissivities found by the simulations are quite high. The lowest value, for granite spheres of 1–10 cm radius, is $e = 0.93$. The corresponding predicted theoretical value of emissivity is $e = 0.80$. It must be kept in mind, though, that the theoretical prediction is for isotropic scatterers. As may be seen in the data for Mie scatterering presented in Appendix A, granite spheres of radius on the order of 3 cm or greater in a material of dielectric constant 2.0 tend to scatter preferentially in the forward direction. This has the effect of allowing radiation which penetrates the surface boundary to penetrate deeper than it would if the scattering were isotropic; the deeper penetration results in greater absorption, lower reflectance, and greater emissivity.

Table 5.1: Simulation parameters and results for granite spheres in soil matrix (see text).

Parameters:				
Matrix:				
ε	$2.00 - i0.01130$	$2.00 - i0.01130$	$2.00 - i0.01130$	$2.00 - i0.01130$
α_P	$0.399\ \mathrm{m}^{-1}$	$0.399\ \mathrm{m}^{-1}$	$0.399\ \mathrm{m}^{-1}$	$0.399\ \mathrm{m}^{-1}$
Scatterers:				
ε	$5.50 - i0.07500$	$5.50 - i0.07500$	$5.50 - i0.07500$	$5.50 - i0.07500$
size range	0.05–1 cm	1–10 cm	2–20 cm	10–100 cm
fill factor	25%	25%	25%	25%
E_s	$0.787\ \mathrm{m}^{-1}$	$9.627\ \mathrm{m}^{-1}$	$6.541\ \mathrm{m}^{-1}$	$1.310\ \mathrm{m}^{-1}$
A_s	$0.298\ \mathrm{m}^{-1}$	$0.699\ \mathrm{m}^{-1}$	$0.675\ \mathrm{m}^{-1}$	$0.343\ \mathrm{m}^{-1}$
ϖ_s	0.621	0.927	0.897	0.738
Layer Depth	50 m	50 m	50 m	50 m
E	$1.186\ \mathrm{m}^{-1}$	$10.026\ \mathrm{m}^{-1}$	$6.940\ \mathrm{m}^{-1}$	$1.709\ \mathrm{m}^{-1}$
ϖ_0	0.412	0.890	0.845	0.566
Simulation Results:				
Number of Rays	1500000	1500000	1500000	1500000
% Escaped	8.76%	12.49%	10.45%	8.21%
(surface)	(7.88%)	(7.89%)	(7.90%)	(7.87%)
(volume)	(0.88%)	(4.60%)	(2.55%)	(0.34%)
% Absorbed	91.24%	87.51%	89.55%	91.79%
(matrix)	(52.24%)	(31.77%)	(33.31%)	(49.35%)
(scatterers)	(39.00%)	(55.74%)	(56.24%)	(42.44%)
(base)	(0.00%)	(0.00%)	(0.00%)	(0.00%)
Normal Emissivity	0.966 ± 0.001	0.931 ± 0.002	0.950 ± 0.001	0.969 ± 0.001
Theoretical Emissivity	0.943	0.800	0.837	0.924
Fresnel Emissivity	0.971	0.971	0.971	0.971

Table 5.2: Simulation parameters and results for basalt spheres in soil matrix (see text).

Parameters:				
Matrix:				
ε	$2.00 - i0.01130$	$2.00 - i0.01130$	$2.00 - i0.01130$	$2.00 - i0.01130$
α_P	$0.399\ \mathrm{m}^{-1}$	$0.399\ \mathrm{m}^{-1}$	$0.399\ \mathrm{m}^{-1}$	$0.399\ \mathrm{m}^{-1}$
Scatterers:				
ε	$7.50 - i0.14500$	$7.50 - i0.14500$	$7.50 - i0.14500$	$7.50 - i0.14500$
size range	0.05–1 cm	1–10 cm	2–20 cm	10–100 cm
fill factor	25%	25%	25%	25%
E_s	$1.289\ \mathrm{m}^{-1}$	$12.369\ \mathrm{m}^{-1}$	$8.085\ \mathrm{m}^{-1}$	$1.208\ \mathrm{m}^{-1}$
A_s	$0.415\ \mathrm{m}^{-1}$	$1.466\ \mathrm{m}^{-1}$	$1.189\ \mathrm{m}^{-1}$	$0.420\ \mathrm{m}^{-1}$
ϖ_s	0.678	0.882	0.853	0.652
Layer Depth	50 m	50 m	50 m	50 m
E	$1.688\ \mathrm{m}^{-1}$	$12.768\ \mathrm{m}^{-1}$	$8.484\ \mathrm{m}^{-1}$	$1.607\ \mathrm{m}^{-1}$
ϖ_0	0.518	0.854	0.813	0.490
Simulation Results:				
Number of Rays	1500000	1500000	1500000	1500000
% Escaped	9.29%	11.65%	10.22%	8.08%
(surface)	(7.89%)	(7.89%)	(7.86%)	(7.88%)
(volume)	(1.40%)	(3.76%)	(2.36%)	(0.20%)
% Absorbed	90.71%	88.35%	89.78%	91.92%
(matrix)	(44.49%)	(18.87%)	(22.56%)	(44.73%)
(scatterers)	(46.22%)	(69.48%)	(67.21%)	(47.18%)
(base)	(0.00%)	(0.00%)	(0.00%)	(0.00%)
Normal Emissivity	0.959 ± 0.001	0.940 ± 0.002	0.953 ± 0.001	0.969 ± 0.001
Theoretical Emissivity	0.931	0.831	0.856	0.934
Fresnel Emissivity	0.971	0.971	0.971	0.971

5.4.2 Alterations to the Tryka and Muhleman Model

The surface model presented by Tryka and Muhleman may be altered in two different ways to create models with lower emissivities.

The first way is to lower the dielectric constant of the matrix. We showed earlier that a major problem of the Tryka and Mulheman results was in their use of the isotropically-scattering atmosphere model to predict the emissivity of the surface; we have also remarked that the theoretical expression derived in this paper (equations 5.44–5.45) reduces to the expression for an isotropically-scattering atmosphere when the dielectric constant of the surface material and atmosphere are the same. It thus seems reasonable that a surface material of dielectric constant somewhat lower than Tryka and Muhleman's value of 2.0 would result in emissivities closer to those predicted by the isotropically-scattering atmosphere.

Figure 5-13 plots the theoretical prediction for the normal-incidence emissivity of a surface containing granite spheres, as a function of the dielectric constant of the matrix material. The matrix is assumed lossless, and the spheres are assumed to have a single scattering albedo of 0.974, the highest value of the distributions listed by Tryka and Muhleman. The curve shows a continuous decrease in the predicted emissivity as the permittivity of the matrix falls from 2 to 1.

We also investigate a low-dielectric surface of this type by simulation. As an exercise in extremity, we set the permittivity of the matrix to 1.0. We use the previous population of granite spheres of 1–10 cm radius. Results are presented in table 5.3 (first column). The normal-incidence emissivity is 0.82. In light of this result, and the general improbability of surfaces with dielectric constants much less than 2.0, it seems that this avenue of pursuit will not be fruitful.

A second alteration to the Tryka and Muhleman surface is to lower the loss in the materials. The materials used by Tryka and Muhleman were chosen as being average; what happens if we consider more extreme values, in particular, the lowest values of dielectric loss? Figure 14 in Campbell and Ulrichs [5] shows the absorption length, in wavelengths, of various rock powders. The longest absorption lengths shown are

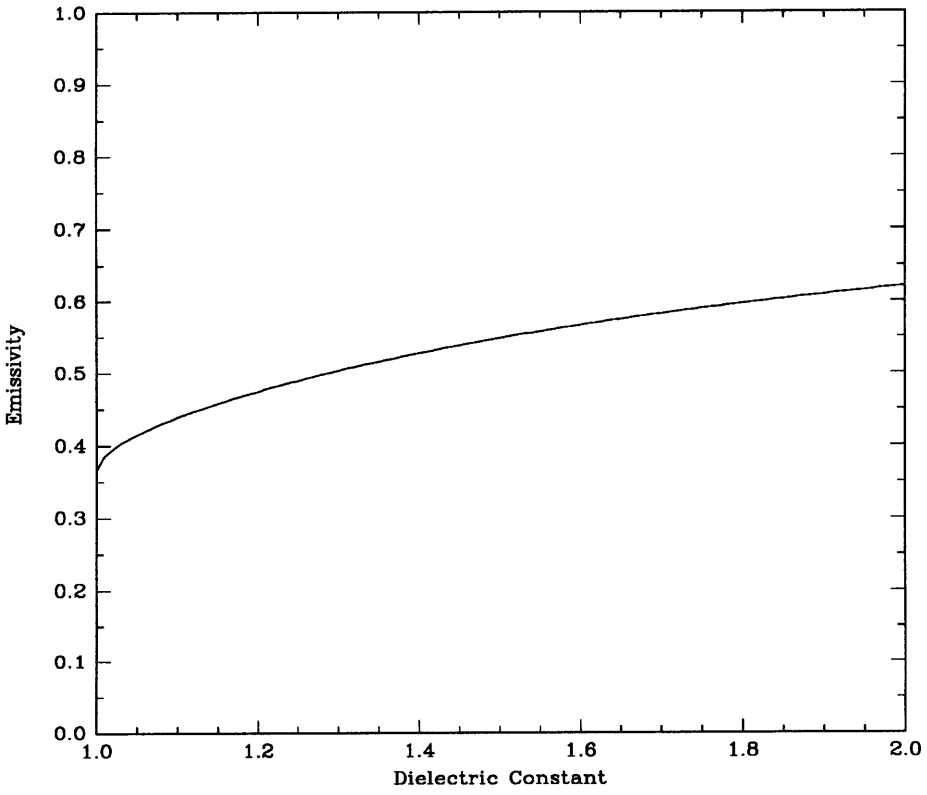

Figure 5-13: Theoretical prediction of normal incidence emissivity for matrix materials with low dielectric constant. The matrix is considered to be lossless, and scatterers have single scattering albedo $\varpi_s = 0.974$.

Table 5.3: Simulation parameters and results for (first column) granite spheres in matrix of extremely low dielectric constant and (second column) low-loss granite spheres in very low-loss soil matrix (see text).

Parameters:		
Matrix:		
ε	$1.00 - i0.00000$	$2.00 - i0.00220$
α_P	$0.000\ \mathrm{m}^{-1}$	$0.078\ \mathrm{m}^{-1}$
Scatterers:		
ε	$5.50 - i0.07500$	$5.50 - i0.02200$
size range	1–10 cm	1–10 cm
fill factor	25%	25%
E_s	$9.558\ \mathrm{m}^{-1}$	$9.621\ \mathrm{m}^{-1}$
A_s	$0.760\ \mathrm{m}^{-1}$	$0.221\ \mathrm{m}^{-1}$
ϖ_s	0.921	0.977
Layer Depth	50 m	50 m
E	$9.558\ \mathrm{m}^{-1}$	$9.698\ \mathrm{m}^{-1}$
ϖ_0	0.921	0.969
Simulation Results:		
Number of Rays	1000000	1000000
% Escaped	27.75%	23.88%
(surface)	(0.00%)	(7.86%)
(volume)	(27.75%)	(16.02%)
% Absorbed	72.25%	76.12%
(matrix)	(0.00%)	(19.75%)
(scatterers)	(72.25%)	(56.37%)
(base)	(0.00%)	(0.00%)
Normal Emissivity	0.817 ± 0.004	0.818 ± 0.003
Theoretical Emissivity	0.541	0.643
Fresnel Emissivity	1.000	0.971

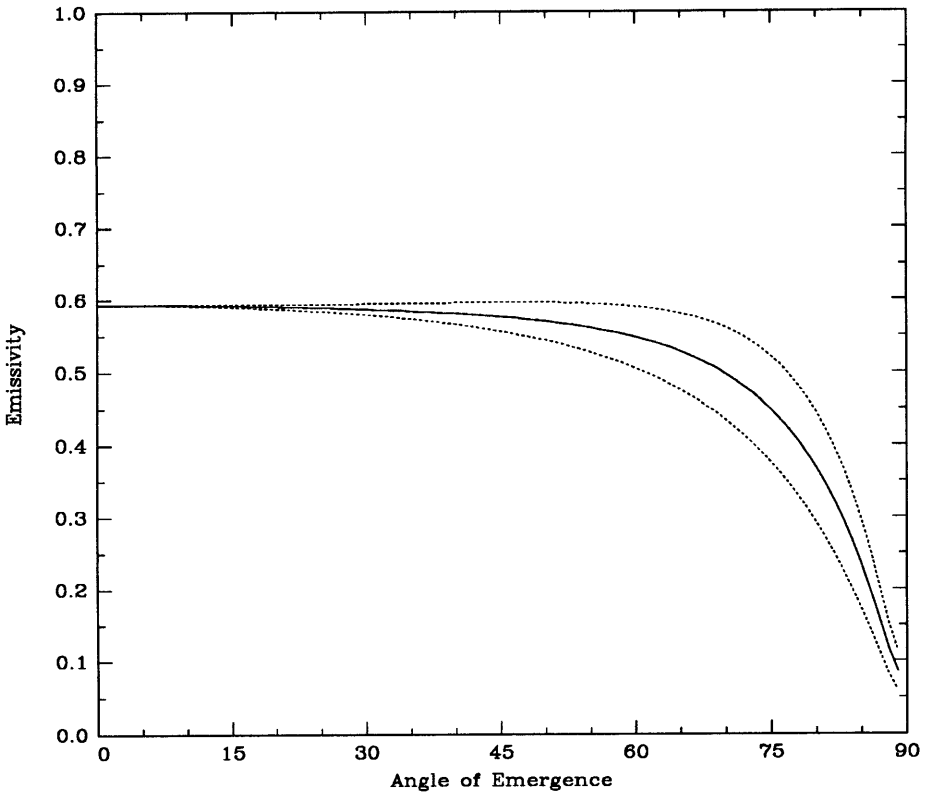

Figure 5-14: Theoretical prediction of emissivity of surface with permittivity $2.0 - i0.0022$, containing low-loss granite spheres ($\varepsilon_s = 5.5 - i0.022$) with continuous radius distribution in range 0–5 cm, which occupy 25% of subsurface volume. Curves are (dotted, upper) vertical polarization, (dotted, lower) horizontal polarization, (solid) average.

between 50 and 100 wavelengths. The lowest value of loss tangent in Campbell and Ulrichs, table 1, is about 0.004. If we adopt an absorption length of 100 wavelengths (12.6 m), our soil has a permittivity $\varepsilon = 2.0 - i0.0022i$. The low value of loss tangent results in a granite of permittivity $\varepsilon = 5.5 - i0.022$. With these parameters, for a continuous distribution of particle radii from 0 to 5 cm occupying 25% of the matrix volume, we calculate an average particle single scattering albedo $\varpi_s = 0.984$ and net particle extinction coefficient $E_s = 12.34$ m^{-1}. The normal emissivity predicted for this surface by equation 5.46 is 0.59. Figure 5-14 is a plot of the emissivity as a function of viewing angle for this surface.

We also investigate this surface by simulation. Once again we use the population of spheres of radius 1–10 cm. Results are presented in table 5.3 (second column). The normal-incidence emissivity is 0.82.

By decreasing the loss in the matrix medium and scatterers as far as can be done based on the Campbell and Ulrichs data, we have decreased the normal emissivity of our hypothetical surface just below 0.6 by the isotropic layer model, but only to 0.82 by our simulation of Mie scatterers. Undoubtedly we could reduce the value in the simulation by choosing more carefully the size of the scatterers; however, it is not likely we could get below the theoretical value. Decreasing the loss in the matrix or the scatterers even further would undoubtedly have beneficial results, and by reducing them to arbitrarily low values, we could manufacture a surface of arbitrarily low emissivity. We will do something along these lines in the next section.

5.4.3 Surfaces Containing Bubbles

If lowering the dielectric loss of the surface materials is the key to producing low emissivity surfaces by volume scattering, then it makes sense to use a known (nearly) lossless material as either the matrix or the scatterer. Most gasses, including the gas comprising the lower atmosphere of Venus, are sufficiently lossless for our needs. Thus in this section we will consider volume scattering by surfaces containing bubbles.

The matrix materials we will use in this section include are the average granite ($\varepsilon = 5.5 - i0.075$) and average basalt ($\varepsilon = 7.5 - i0.145$) from above, and the low-loss soil with dielectric constant of 2 and attenuation distance of 2.5 m ($\varepsilon = 2.0 - i0.0113$). It should be noted that a dielectric constant of 2 is representative of powders, not of solid rocks, and probably would not be able to sustain a structure containing bubbles. In addition to these materials, we will consider a rock from the data of Ulaby et al. [74]. The material is described as "silicified volcanic"; its composition is over 96% SiO_2. It has a fairly low loss factor, lower than any of the other volcanic rocks listed; its permittivity is $\varepsilon = 4.8 - i0.014$. (We will mention some other low-loss rocks from this study later on.)

In all cases, the bubbles will be considered to have permittivity 1.0, and thus

Table 5.4: Theoretical prediction of normal incidence emissivity for surfaces containing 25% bubbles with continuous size distribution in range 0–5 cm, $N(a) \propto a^{-3}$.

Matrix Material	Relative Permittivity	α_P	E_s	Normal Emissivity
Granite	$5.5 - i0.075$	1.597	8.136	0.76
Basalt	$7.5 - i0.145$	2.645	9.676	0.80
Low-loss Soil	$2.0 - i0.0113$	0.399	1.967	0.85
Silica	$4.8 - i0.014$	0.319	7.449	0.75

single scattering albedo 1.0. The actual relative permittivity of the lower atmosphere of Venus is approximately 1.03, and varies with altitude [48]. The atmospheric attenuation is extremely low; the attenuation distance is approximately 160 km at the mean surface (calculation based on tables in [45]), and increases with altitude. Thus the power absorption coefficient is on the order of 10^{-5} or less. In our context, there is no significant difference between the dielectric properties of the atmosphere and of a vacuum.

We will start by considering the theoretical prediction for the emissivity of a surface of each type containing bubbles with a continuous range of radii 0–5 cm. In each case it is necessary to first calculate the extinction coefficient using Mie theory; then the equations from section 5.2.2 can be employed to predict the emissivity. Results are shown in table 5.4.

Monte Carlo simulations of the scattering from surfaces with each type of matrix material have been performed. The particular size ranges and distribution, volume filling fraction, and scattering layer thickness are the same as were used in previous simulations. Results are presented in tables 5.5–5.8.

Neither the theoretical nor the simulation results are very promising. Examination of the simulation results indicates that almost none of the reflected rays are scattered back up from below the surface. The problem is the absorption in the matrix.

We know in theory that if there were no loss in the matrix, that the emissivity of the surface would be 0. How far must the dielectric loss in the matrix be reduced in order to produce the desired low values of emissivity?

Table 5.5: Simulation parameters and results for bubbles in granite matrix (see text).

Parameters:				
Matrix:				
ε	$5.50 - i0.07500$	$5.50 - i0.07500$	$5.50 - i0.07500$	$5.50 - i0.07500$
α_P	1.597 m^{-1}	1.597 m^{-1}	1.597 m^{-1}	1.597 m^{-1}
Scatterers:				
ε	$1.00 - i0.00000$	$1.00 - i0.00000$	$1.00 - i0.00000$	$1.00 - i0.00000$
size range	0.05–1 cm	1–10 cm	2–20 cm	10–100 cm
fill factor	25%	25%	25%	25%
E_s	1.825 m^{-1}	6.954 m^{-1}	4.848 m^{-1}	1.175 m^{-1}
A_s	0.000 m^{-1}	0.000 m^{-1}	0.000 m^{-1}	0.000 m^{-1}
ϖ_s	1.000	1.000	1.000	1.000
Layer Depth	50 m	50 m	50 m	50 m
E	3.422 m^{-1}	8.552 m^{-1}	6.446 m^{-1}	2.773 m^{-1}
ϖ_0	0.533	0.813	0.752	0.424
Simulation Results:				
Number of Rays	1000000	1000000	1000000	1000000
% Escaped	20.65%	20.77%	20.59%	20.42%
(surface)	(20.36%)	(20.36%)	(20.38%)	(20.40%)
(volume)	(0.29%)	(0.41%)	(0.21%)	(0.02%)
% Absorbed	79.35%	79.23%	79.41%	79.58%
(matrix)	(79.35%)	(79.23%)	(79.41%)	(79.58%)
(scatterers)	(0.00%)	(0.00%)	(0.00%)	(0.00%)
(base)	(0.00%)	(0.00%)	(0.00%)	(0.00%)
Normal Emissivity	0.837 ± 0.002	0.836 ± 0.003	0.838 ± 0.003	0.840 ± 0.003
Theoretical Emissivity	0.827	0.804	0.812	0.830
Fresnel Emissivity	0.838	0.838	0.838	0.838

Table 5.6: Simulation parameters and results for bubbles in basalt matrix (see text).

Parameters:				
Matrix:				
ε	$7.50 - i0.14500$	$7.50 - i0.14500$	$7.50 - i0.14500$	$7.50 - i0.14500$
α_P	2.645 m^{-1}	2.645 m^{-1}	2.645 m^{-1}	2.645 m^{-1}
Scatterers:				
ε	$1.00 - i0.00000$	$1.00 - i0.00000$	$1.00 - i0.00000$	$1.00 - i0.00000$
size range	0.05–1 cm	1–10 cm	2–20 cm	10–100 cm
fill factor	25%	25%	25%	25%
E_s	3.232 m^{-1}	7.842 m^{-1}	5.296 m^{-1}	1.225 m^{-1}
A_s	0.000 m^{-1}	0.000 m^{-1}	0.000 m^{-1}	0.000 m^{-1}
ϖ_s	1.000	1.000	1.000	1.000
Layer Depth	50 m	50 m	50 m	50 m
E	5.876 m^{-1}	10.486 m^{-1}	7.941 m^{-1}	3.869 m^{-1}
ϖ_0	0.550	0.748	0.667	0.317
Simulation Results:				
Number of Rays	1000000	1000000	1000000	1000000
% Escaped	25.13%	25.00%	25.03%	24.87%
(surface)	(24.94%)	(24.83%)	(24.95%)	(24.86%)
(volume)	(0.19%)	(0.17%)	(0.08%)	(0.01%)
% Absorbed	74.87%	75.00%	74.97%	75.13%
(matrix)	(74.87%)	(75.00%)	(74.97%)	(75.13%)
(scatterers)	(0.00%)	(0.00%)	(0.00%)	(0.00%)
(base)	(0.00%)	(0.00%)	(0.00%)	(0.00%)
Normal Emissivity	0.787 ± 0.004	0.784 ± 0.004	0.784 ± 0.004	0.787 ± 0.004
Theoretical Emissivity	0.775	0.766	0.771	0.780
Fresnel Emissivity	0.784	0.784	0.784	0.784

Table 5.7: Simulation parameters and results for bubbles in soil matrix (see text).

Parameters:				
Matrix:				
ε	$2.00 - i0.01130$	$2.00 - i0.01130$	$2.00 - i0.01130$	$2.00 - i0.01130$
α_P	$0.399\ \mathrm{m}^{-1}$	$0.399\ \mathrm{m}^{-1}$	$0.399\ \mathrm{m}^{-1}$	$0.399\ \mathrm{m}^{-1}$
Scatterers:				
ε	$1.00 - i0.00000$	$1.00 - i0.00000$	$1.00 - i0.00000$	$1.00 - i0.00000$
size range	0.05–1 cm	1–10 cm	2–20 cm	10–100 cm
fill factor	25%	25%	25%	25%
E_s	$0.110\ \mathrm{m}^{-1}$	$3.485\ \mathrm{m}^{-1}$	$2.984\ \mathrm{m}^{-1}$	$1.150\ \mathrm{m}^{-1}$
A_s	$0.000\ \mathrm{m}^{-1}$	$0.000\ \mathrm{m}^{-1}$	$0.000\ \mathrm{m}^{-1}$	$0.000\ \mathrm{m}^{-1}$
ϖ_s	1.000	1.000	1.000	1.000
Layer Depth	50 m	50 m	50 m	50 m
E	$0.509\ \mathrm{m}^{-1}$	$3.884\ \mathrm{m}^{-1}$	$3.383\ \mathrm{m}^{-1}$	$1.549\ \mathrm{m}^{-1}$
ϖ_0	0.216	0.897	0.882	0.742
Simulation Results:				
Number of Rays	1500000	1500000	1500000	1500000
% Escaped	8.22%	9.68%	9.07%	8.04%
(surface)	(7.92%)	(7.89%)	(7.90%)	(7.90%)
(volume)	(0.30%)	(1.79%)	(1.17%)	(0.14%)
% Absorbed	91.78%	90.32%	90.93%	91.96%
(matrix)	(91.78%)	(90.32%)	(90.93%)	(91.96%)
(scatterers)	(0.00%)	(0.00%)	(0.00%)	(0.00%)
(base)	(0.00%)	(0.00%)	(0.00%)	(0.00%)
Normal Emissivity	0.969 ± 0.001	0.959 ± 0.001	0.961 ± 0.001	0.970 ± 0.001
Theoretical Emissivity	0.959	0.793	0.808	0.884
Fresnel Emissivity	0.971	0.971	0.971	0.971

Table 5.8: Simulation parameters and results for bubbles in silica matrix (see text).

Parameters:				
Matrix:				
ε	$4.80 - i0.01400$	$4.80 - i0.01400$	$4.80 - i0.01400$	$4.80 - i0.01400$
α_P	$0.319\ \mathrm{m}^{-1}$	$0.319\ \mathrm{m}^{-1}$	$0.319\ \mathrm{m}^{-1}$	$0.319\ \mathrm{m}^{-1}$
Scatterers:				
ε	$1.00 - i0.00000$	$1.00 - i0.00000$	$1.00 - i0.00000$	$1.00 - i0.00000$
size range	0.05–1 cm	1–10 cm	2–20 cm	10–100 cm
fill factor	25%	25%	25%	25%
E_s	$1.378\ \mathrm{m}^{-1}$	$6.585\ \mathrm{m}^{-1}$	$4.654\ \mathrm{m}^{-1}$	$1.203\ \mathrm{m}^{-1}$
A_s	$0.000\ \mathrm{m}^{-1}$	$0.000\ \mathrm{m}^{-1}$	$0.000\ \mathrm{m}^{-1}$	$0.000\ \mathrm{m}^{-1}$
ϖ_s	1.000	1.000	1.000	1.000
Layer Depth	50 m	50 m	50 m	50 m
E	$1.697\ \mathrm{m}^{-1}$	$6.904\ \mathrm{m}^{-1}$	$4.974\ \mathrm{m}^{-1}$	$1.523\ \mathrm{m}^{-1}$
ϖ_0	0.812	0.954	0.936	0.790
Simulation Results:				
Number of Rays	1000000	1000000	1000000	1000000
% Escaped	20.20%	21.58%	20.39%	18.76%
(surface)	(18.47%)	(18.50%)	(18.42%)	(18.47%)
(volume)	(1.73%)	(3.08%)	(1.97%)	(0.29%)
% Absorbed	79.80%	78.42%	79.61%	81.24%
(matrix)	(79.80%)	(78.42%)	(79.61%)	(81.24%)
(scatterers)	(0.00%)	(0.00%)	(0.00%)	(0.00%)
(base)	(0.00%)	(0.00%)	(0.00%)	(0.00%)
Normal Emissivity	0.846 ± 0.003	0.835 ± 0.003	0.846 ± 0.003	0.861 ± 0.003
Theoretical Emissivity	0.823	0.756	0.775	0.827
Fresnel Emissivity	0.861	0.861	0.861	0.861

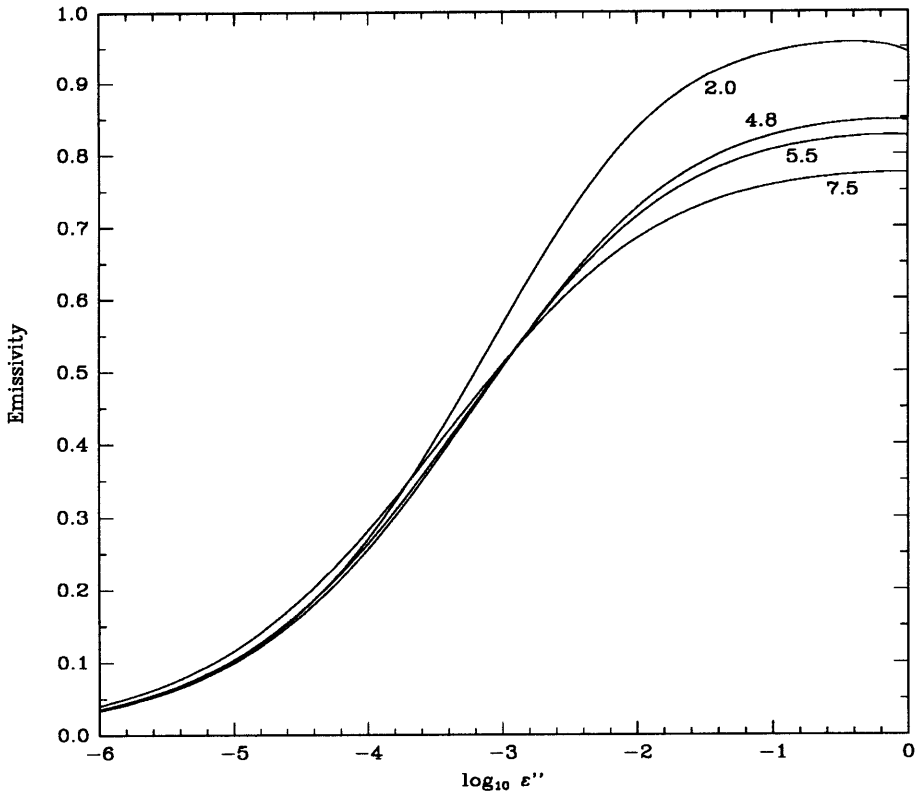

Figure 5-15: Theoretical prediction of emissivity at normal incidence as a function of loss factor for various materials containing bubbles. Materials are granite ($\varepsilon' = 5.5$), basalt ($\varepsilon' = 7.5$), soil ($\varepsilon' = 2.0$), and silica ($\varepsilon' = 4.8$). Bubbles have a continuous distribution of radii in the range 0–5 cm, and occupy 25% of the subsurface volume.

This question is answered in figure 5-15. In this figure, the theoretical emissivity of the surface is plotted as a function of (the base 10 logarithm of) the loss factor of the matrix. In all cases we have again used bubbles in the range 0–5 cm at a filling factor of 25%; we have assumed that the extinction coefficient does not vary significantly with the changing loss factor, and thus the values of E_s in table 5.4 are valid.

This graph shows that the emissivity of a surface containing the aforementioned distribution of bubbles can fall into the range 0.25–0.50, corresponding to the lowest emissivities on the surface of Venus, if the imaginary part of the permittivity falls as low as 10^{-3}–10^{-4}. For materials in the range of dielectric constants we have

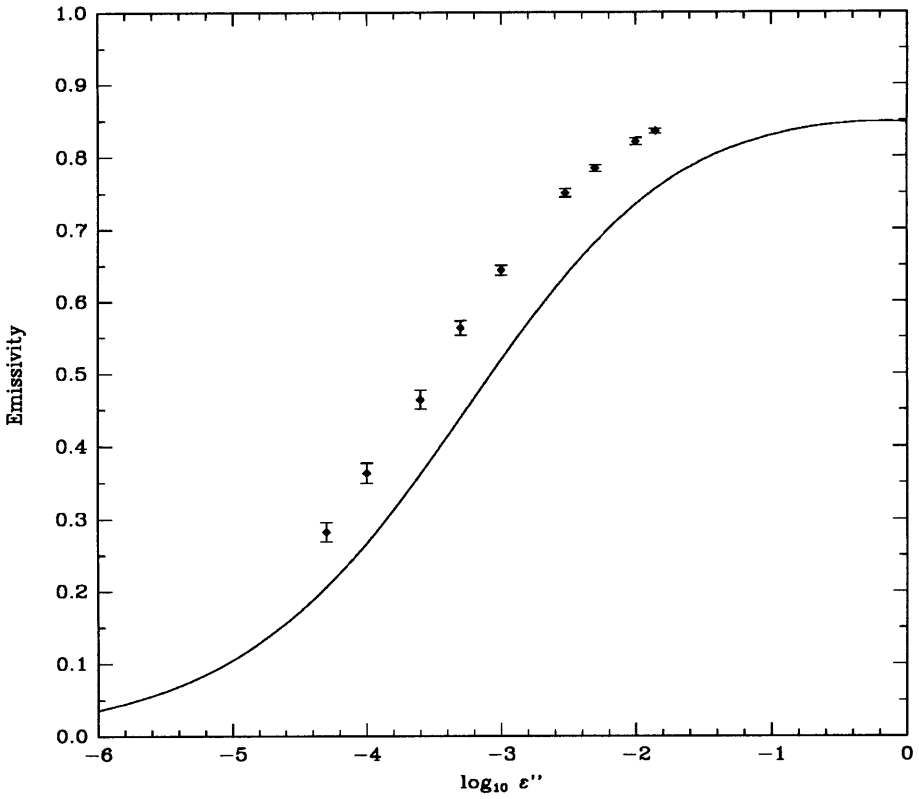

Figure 5-16: Normal-incidence emissivity as a function of loss factor as measured by simulation of silica matrix containing bubbles (see tables 5.9 and 5.10). Solid line is theoretical prediction for the same model ($E_s = 6.585$ m^{-1}).

considered, this requirement on ε'' is largely independent of the value of the real part of the permittivity, ε'.

Our final set of simulations investigates the effects of lowering the loss factor of the matrix. We have chosen to use the silica matrix, $\varepsilon' = 4.8$, with scatterer radii in the range 1–10 cm. Eight tests were performed, with values of ε'' as low as 5×10^{-5}. Data from these simulations is presented in tables 5.9 and 5.10. The resulting emissivities are plotted in figure 5-16, along with the theoretical curve for the same extinction coefficient as is found for the simulation's population.

Table 5.9: Simulation parameters and results for bubbles in silica matrix with reduced loss factor (see text).

Parameters:				
Matrix:				
ε	$4.80 - i0.01000$	$4.80 - i0.00500$	$4.80 - i0.00300$	$4.80 - i0.00100$
α_P	0.228 m^{-1}	0.114 m^{-1}	0.068 m^{-1}	0.023 m^{-1}
Scatterers:				
ε	$1.00 - i0.00000$	$1.00 - i0.00000$	$1.00 - i0.00000$	$1.00 - i0.00000$
size range	1–10 cm	1–10 cm	1–10 cm	1–10 cm
fill factor	25%	25%	25%	25%
E_s	6.585 m^{-1}	6.585 m^{-1}	6.585 m^{-1}	6.585 m^{-1}
A_s	0.000 m^{-1}	0.000 m^{-1}	0.000 m^{-1}	0.000 m^{-1}
ϖ_s	1.000	1.000	1.000	1.000
Layer Depth	50 m	50 m	50 m	50 m
E	6.813 m^{-1}	6.699 m^{-1}	6.654 m^{-1}	6.608 m^{-1}
ϖ_0	0.967	0.983	0.990	0.997
Simulation Results:				
Number of Rays	500000	500000	500000	500000
% Escaped	22.78%	26.35%	29.54%	39.05%
(surface)	(18.44%)	(18.58%)	(18.43%)	(18.37%)
(volume)	(4.34%)	(7.77%)	(11.11%)	(20.68%)
% Absorbed	77.22%	73.65%	70.46%	60.95%
(matrix)	(77.22%)	(73.65%)	(70.46%)	(60.95%)
(scatterers)	(0.00%)	(0.00%)	(0.00%)	(0.00%)
(base)	(0.00%)	(0.00%)	(0.00%)	(0.00%)
Normal Emissivity	0.821 ± 0.005	0.784 ± 0.005	0.750 ± 0.006	0.643 ± 0.007
Theoretical Emissivity	0.734	0.682	0.636	0.519
Fresnel Emissivity	0.861	0.861	0.861	0.861

Table 5.10: Simulation parameters and results for bubbles in silica matrix with reduced loss factor (see text).

Parameters:				
Matrix:				
ε	$4.80 - i0.00050$	$4.80 - i0.00025$	$4.80 - i0.00010$	$4.80 - i0.00005$
α_P	0.011 m^{-1}	0.006 m^{-1}	0.002 m^{-1}	0.001 m^{-1}
Scatterers:				
ε	$1.00 - i0.00000$	$1.00 - i0.00000$	$1.00 - i0.00000$	$1.00 - i0.00000$
size range	1–10 cm	1–10 cm	1–10 cm	1–10 cm
fill factor	25%	25%	25%	25%
E_s	6.585 m^{-1}	6.585 m^{-1}	6.585 m^{-1}	6.585 m^{-1}
A_s	0.000 m^{-1}	0.000 m^{-1}	0.000 m^{-1}	0.000 m^{-1}
ϖ_s	1.000	1.000	1.000	1.000
Layer Depth	50 m	50 m	50 m	50 m
E	6.597 m^{-1}	6.591 m^{-1}	6.587 m^{-1}	6.586 m^{-1}
ϖ_0	0.998	0.999	1.000	1.000
Simulation Results:				
Number of Rays	250000	200000	200000	250000
% Escaped	46.71%	54.52%	64.94%	72.05%
(surface)	(18.47%)	(18.48%)	(18.68%)	(18.63%)
(volume)	(28.24%)	(36.04%)	(46.26%)	(53.42%)
% Absorbed	53.29%	45.48%	35.06%	27.95%
(matrix)	(53.28%)	(45.32%)	(33.73%)	(24.53%)
(scatterers)	(0.00%)	(0.00%)	(0.00%)	(0.00%)
(base)	(0.01%)	(0.17%)	(1.33%)	(3.42%)
Normal Emissivity	0.563 ± 0.010	0.464 ± 0.013	0.363 ± 0.014	0.282 ± 0.013
Theoretical Emissivity	0.440	0.361	0.267	0.206
Fresnel Emissivity	0.861	0.861	0.861	0.861

5.4.4 Discussion

We have shown in the preceding section that it is not likely that materials of ordinary composition could produce volume scattering effects of sufficient magnitude to result in surface emissivities as low as those described in chapter 3. However, if the loss factors of the scatterers and of the matrix are sufficiently low, the desired low emissivities can be produced. The problem is simplified by using voids, or bubbles, as the scatterer; we then only need to find one material with extremely low loss.

It is difficult to say how far into the realm of fantasy we must tread in order to find naturally-occurring materials with loss factors low enough to satisfy our requirements. Such materials can be manufactured; synthetic materials used in waveguides and transmission lines are examples. However, these materials go through a purification process which is very rare in nature, as far as we know.

There are two rocks listed in the study by Ulaby et al. [74] (see table 4.2) which have loss factors below the threshold of measurement. First there is a sample of gypsum ($CaSO_4 \cdot 2H_2O$), whose measured permittivity is $\varepsilon' = 3.9$, $\varepsilon'' < 0.002$. Gypsum is not expected to be stable on the surface of Venus; however, anhydrite ($CaSO_4$) is thought to be stable [18]. A second rock with low loss is quartzite; their sample has a measured permittivity of $\varepsilon' = 4.9$, $\varepsilon'' < 0.002$. Its composition is nearly 100% SiO_2. This rock's permittivity provides us with some rationalization for lowering the loss factor of the silica matrix, as we did in the last section.

The existence of vesicles in volcanic rocks is not unusual. Pumice, for example, is often less dense than water. Many pahoehoe flows contain more than 20% vesicles, by volume; it is not uncommon to find parts of flows with 50% vesicles [7]. Most basalts contain only a few volume percent of vesicles, however. Vesicle sizes may range from sub-millimeter to several centimeters. The growth and coalescence rates of bubbles within a magma are controlled by several factors, including the composition, solubility, concentration, and diffusion rate of volatiles in the magma, the ascent rate of the magma, and the density, viscosity and surface tension of the magma [7]. In surface flows, it is generally observed that lavas become denser with increasing distance from the point of eruption; this is caused by the coalescence of bubbles and

by the release of bubbles to the atmosphere at the surface or at cracks within the lava [81].

The question of magmatic vesiculation on Venus has been explored by Garvin et al. [26]. They find that vesicles with sizes between 0.1 mm and 10 cm should be common in Venusian basaltic lavas, providing that at least trace amounts of volatiles exist in the magma. The high atmospheric pressure on Venus tends to retard bubble coalescence and disruption; while this makes explosive volcanism unlikely, it makes vesicular lavas more likely. The total volume percent of bubbles is heavily dependent on the identity and concentration of the volatiles. Although Garvin et al. mention that they studied vesiculation under a range of surface atmospheric pressures (55–95 bars), they do not mention any significant differences in the vesiculation of lavas erupting at different altitudes. Rather, they infer that the ambient surface pressure plays only a small role in the vesiculation of the magma; the main effect is on the possibility of disruption (and explosive volcanism) at the surface.

Based on this last statement, there is little reason to expect significant differences in the vesiculation of lavas at high altitudes as opposed to the rest of the surface of Venus. Instead, we would expect most variations in vesiculation to occur because of differences in magma composition and volatile content. We would not generally expect these factors to be the same at different volcanic sites, or even to remain constant across the eruptive lifetime of a single volcano.

In conclusion, it is quite difficult to piece together a geological scenario where volume scattering from vesicles in a low-loss material can play the major role in reducing the emissivities in high altitude areas of Venus. We know that such surfaces, if they existed, could result in the observed emissivities. We have support for the existence of vesicles in Venus basalts. We know of materials with relatively low loss, although we are not sure if materials with the extremely low loss necessary for our purposes exists in nature; if they exist at all, they are likely to be quite rare. A very pure silica would be the most likely candidate. Beyond this, we have no basis for believing that pure silicas containing vesicles exist in large quantities at high altitudes on Venus. Likewise, uplifted areas such as Dali are not explained at all by

this mechanism.

One type of volume scattering has been mostly ignored throughout this chapter: the scattering by subsurface facets, as was proposed by Goldstein and Green [28] to explain the unusual radar reflectivity of Ganymede. Like bubble scattering, this type of scattering is lossless, and thus we need only be concerned about the loss in the surface medium. The problem of scattering in such a surface is a little more difficult to study than the scattering from a surface containing discrete objects. Although we may treat large facets as Fresnel reflectors, there is no theory regarding the scattering of radiation from a matrix containing fractures of size near or below the wavelength. An investigation in this area would be a logical next step in the study of volume scattering. On the other hand, the problem of the generation of large quantities of a low loss material, and only at high altitudes, still makes this an unlikely mechanism to be responsible for the large areas of low emissivity on Venus.

Chapter 6

Conclusions

Observations performed by the Magellan radiometer experiment have confirmed previous findings that a few regions on Venus, primarily at higher elevations, possess unexpectedly low values of radiothermal emissivity, occasionally reaching as low as 0.3. Values of emissivity below 0.7 are displayed by over 1.5% of the surface observed during cycle 1 of the Magellan mission; features which exhibit low emissivity include highlands, volcanoes, tectonically uplifted terrain, and impact craters. There is a strong correlation between low emissivity and high elevation; the emissivity remains relatively high up to a certain elevation, the "critical radius," above which it drops rapidly to a lower value in a short elevation span. The critical radius varies from feature to feature, but on average, lies at an altitude of about 6054 km. Notable exceptions to the association of low emissivity and high altitude exist; for example, Maat Mons, Lakshmi Planum, and the low-backscatter summits of many volcanoes display normal to high emissivities at high elevations, while in some impact craters and plains areas we find low emissivities at low elevations.

Two mechanisms which could be responsible for low emissivities have been investigated: emission from a highly reflective single interface between the atmosphere and a surface material having a bulk dielectric constant of order 80 or more, and emission from the surface of a low-loss material having a more usual permittivity, but which contains subsurface scatterers.

A consideration of previously suggested models involving high-dielectric materi-

als in light of the Magellan observations leads us to favor a model in which rocks containing a conductive mineral form a "loaded dielectric." Most of the Magellan observations could be explained if this conductive mineral were created by weathering of ordinary Venus rocks at high altitudes. Unfortunately, the identity of the conductive phase, or of equal importance, the complementary nonconductive phase, is not known. Experimental work to study the electrical properties of real loaded dielectric rocks, the properties of conductive minerals under Venus surface conditions, and the properties of more unusual materials than have previously been considered would be helpful in solving this problem.

Theoretical results and Monte Carlo simulations have been used to study the properties of surfaces containing subsurface scatterers. We show that the previously proposed volume scattering model, a low-loss soil of dielectric constant 2 containing scatterers made of ordinary granite or basalt, cannot account for the low emissivities observed by Magellan. However, scattering from a material with very low loss (loss tangent of order 10^{-3} or less) containing subsurface voids could produce the observed results. The most likely candidate for a low loss material is a very pure silica. We do not find it likely that such a surface could exist over large areas of Venus.

Two different measurements could be made to distinguish between low emissivity caused by a high-dielectric surface, and low emissivity caused by volume scattering. The first is a measurement of the linear polarization ratio of the emission from a low-emissivity area. If the surface is a high-dielectric material, then the dielectric constant of the material would of course be very high; if volume scattering is at work, the dielectric constant would probably be quite low. The difference in polarization ratios for materials of low and high dielectric constants can be seen in figure 4-4. Note that the difference is greater at larger angles of incidence, so the measurements should be made at as large of an angle of incidence as possible. Measurements of emissivity in vertical polarization could be made by rotating the Magellan spacecraft by 90°. In fact, this experiment is expected to be carried out later in the Magellan mission.

A second method involves measurement of the circular polarization ratio of re-

flected radiation. From a normal smooth surface, we expect the echo from the surface to be entirely in the opposite sense of polarization from what we sent. Surface roughness may cause some amount of echo return in the unexpected sense (the same sense as what was sent); if the surface is perfectly rough, we would receive echoes with equal power in the expected and unexpected sense. However, coherent backscatter from a surface containing subsurface scatterers (see [34]) could cause us to receive backscatter polarized predominantly in the unexpected sense. Measurements of circular polarization ratio could easily be made from earth, and in fact, data should be available fairly soon.

The ultimate observations to resolve this issue will be made by a spacecraft on the surface of Venus. We would like to recommend that a future Venus lander be set down in the festooned flow in Ovda Regio, which is likely to be one of the smoother surfaces in the highlands, and within which is located the lowest measured emissivity on Venus.

Appendix A

Mie Scattering

Mie theory is an exact theory for the scattering of a plane wave by an isotropic, homogeneous sphere of any size. This appendix will present only the important results of the theory which were used in the scattering simulation (section 5.3. For a full derivation of the theory, the interested reader is referred to [78, 42, 2]. After the theory, there is a discussion of Mie scattering in lossy media and how we handle it in the scattering simulation, a set of figures showing typical Mie scattering properties, and a discussion of scattering by nonspherical particles.

A.1 Theory

The main references used in preparing this section were van de Hulst [78] and Kerker [42].

The usual presentation of the theory assumes that both the sphere medium and the surrounding medium (referred to as the "matrix" in the present work) are isotropic, homogeneous, and nonmagnetic; also, the matrix medium is assumed to be lossless. The key results of Mie theory we wish to use are the pattern of scattered radiation and the cross sections for extinction, scattering, and absorption.

Let λ_0 be the free-space wavelength of the radiation incident on a particle of radius a. ε_1 and ε_2 are the relative complex permittivities of the matrix and particle media, respectively (note that since the matrix is lossless, ε_1 is real). From these

basic quantities we may derive the indices of refraction of the (non-magnetic) media

$$n_1 = \sqrt{\varepsilon_1}, \tag{A.1}$$

$$n_2 = \sqrt{\varepsilon_2} \tag{A.2}$$

and their ratio $n_{21} = n_2/n_1$; the wavelength of radiation in the two media

$$\lambda_1 = \lambda_0/n_1, \tag{A.3}$$

$$\lambda_2 = \lambda_0/n_2; \tag{A.4}$$

the wave numbers in the two media

$$k_1 = 2\pi/\lambda_1, \tag{A.5}$$

$$k_2 = 2\pi/\lambda_2; \tag{A.6}$$

and the particle size parameters in the two media

$$x = k_1 a = 2\pi a/\lambda_1, \tag{A.7}$$

$$y = k_2 a = 2\pi a/\lambda_2. \tag{A.8}$$

The geometry is shown in Figure A-1. ϕ is the scattering angle; $\phi = 0°$ corresponds to forward scattering, and $\phi = 180°$ corresponds to backscattering. θ is the azimuth angle.

Consider a plane wave of unit intensity linearly polarized with the electric vector parallel to $\theta = 0$, incident on a spherical scatterer at the origin. The far-field radiant intensity scattered into direction (ϕ, θ) will be

$$I_\perp(r, \phi, \theta) = \frac{1}{k_1^2 r^2} i_1(\phi) \sin^2(\theta), \tag{A.9}$$

$$I_\parallel(r, \phi, \theta) = \frac{1}{k_1^2 r^2} i_2(\phi) \cos^2(\theta). \tag{A.10}$$

$I_\perp$ and $I_\parallel$ are normal to and parallel to the plane of scattering, respectively. $i_1(\phi)$

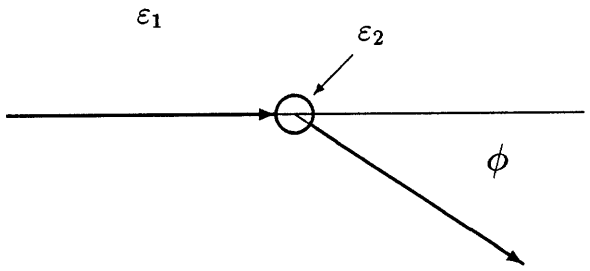

Figure A-1: Geometry of Mie scattering. Sphere of relative permittivity ε_2 is imbedded in matrix of relative permittivity ε_1.

and $i_2(\phi)$ are the intensity functions, related to the Mie amplitude functions $S_1(\phi)$ and $S_2(\phi)$ by

$$i_1(\phi) = |S_1(\phi)|^2, \tag{A.11}$$

$$i_2(\phi) = |S_2(\phi)|^2. \tag{A.12}$$

S_1 and S_2 are expressed as infinite series:

$$S_1(\phi) = \sum_{n=1}^{\infty} \frac{2n+1}{n(n+1)} \{a_n \pi_n(\cos\phi) + b_n \tau_n(\cos\phi)\}, \tag{A.13}$$

$$S_2(\phi) = \sum_{n=1}^{\infty} \frac{2n+1}{n(n+1)} \{b_n \pi_n(\cos\phi) + a_n \tau_n(\cos\phi)\}. \tag{A.14}$$

In practice these series converge rapidly when $n > x$, so only the first approximately $x+3$ terms need be calculated. π_n and τ_n are related to Associated Legendre functions:

$$\pi_n(\cos\phi) = \frac{1}{\sin\phi} P_n^1(\cos\phi), \tag{A.15}$$

$$\tau_n(\cos\phi) = \frac{d}{d\phi} P_n^1(\cos\phi). \tag{A.16}$$

a_n and b_n, functions only of the size parameters x and y, are sometimes called the

Mie Coefficients and are given by

$$a_n = \frac{\psi_n'(y)\psi_n(x) - n_{21}\psi_n(y)\psi_n'(x)}{\psi_n'(y)\zeta_n(x) - n_{21}\psi_n(y)\zeta_n'(x)}, \tag{A.17}$$

$$b_n = \frac{n_{21}\psi_n'(y)\psi_n(x) - \psi_n(y)\psi_n'(x)}{n_{21}\psi_n'(y)\zeta_n(x) - \psi_n(y)\zeta_n'(x)}. \tag{A.18}$$

where ψ_n and ζ_n are Riccati-Bessel functions, related to Bessel functions by

$$\psi_n(z) = \sqrt{\frac{\pi z}{2}} J_{n+1/2}(z), \tag{A.19}$$

$$\chi_n(z) = -\sqrt{\frac{\pi z}{2}} N_{n+1/2}(z), \tag{A.20}$$

$$\zeta_n(z) = \psi_n(z) + i\chi_n(z). \tag{A.21}$$

ψ_n' and ζ_n' are their derivatives.

The extinction cross section C_{ext} is defined such that the total power removed from the incident beam by the scatterer is equal to that which would have fallen on an area C_{ext} in the absense of a scatterer. The power removed from the incident beam is either scattered into other directions, or absorbed by the scatterer; thus we may define in a similar manner the scattering cross section C_{sca} and the absorption cross section C_{abs}. For a Mie scatterer, the extinction and scattering cross sections are given by

$$C_{ext} = \frac{2\pi}{k_1^2} \sum_{n=1}^{\infty} (2n+1)\ \mathrm{Re}\{a_n + b_n\}, \tag{A.22}$$

$$C_{sca} = \frac{2\pi}{k_1^2} \sum_{n=1}^{\infty} (2n+1)\ (|a_n|^2 + |b_n|^2), \tag{A.23}$$

and the absorption cross section is the difference between them:

$$C_{abs} = C_{ext} - C_{sca}. \tag{A.24}$$

The extinction, scattering, and absorption efficiencies are given by

$$Q_{ext} = C_{ext}/C_{geo}, \tag{A.25}$$

$$Q_{sca} = C_{sca}/C_{geo}, \tag{A.26}$$

$$Q_{abs} = C_{abs}/C_{geo}, \tag{A.27}$$

where $C_{geo} = \pi a^2$ is the geometric cross section of the particle. The particle single scattering albedo, the ratio of power scattered to power removed from the incident beam, is

$$\varpi_p = Q_{sca}/Q_{ext}. \tag{A.28}$$

A.2 Scattering in Lossy Media

Bohren and Gilra are among those who have investigated Mie scattering in a lossy medium [3]. When the matrix medium is lossy, the extinction cross section must be rewritten

$$C_{ext} = 2\pi \sum_{n=1}^{\infty} (2n+1) \operatorname{Re}\left\{\frac{a_n + b_n}{k_1^2}\right\}. \tag{A.29}$$

Bohren and Gilra further explain that in the case of an absorbing medium, the extinction cross section can no longer be separated into components representing scattering by the particle and absorption by the particle, since the matrix takes part in the absorption process. We have found that blind application of the above equations to lossy media containing lossless scatterers, for example, leads to negative absorption cross sections. In general terms, this is an effect of having an area inside the medium—specifically, the volume inside the scatterers—where there is less loss than there would have been in the absence of scatterers.

In the work presented in this paper, we have circumvented the problem by ignoring the loss in the matrix medium when calculating the Mie scattering pattern and efficiencies. The main justification for doing this is that the loss in the matrix media we are using is fairly low. Thus, the fractional difference in permittivities between lossy and lossless versions of the same material is not expected to change the scattering pattern, total amount of scattered radiation, or total amount of radiation

absorbed inside the scatterer significantly. What we will not take into account with this method is the change in loss in the medium, especially the reduction in absorption which occurs when part of the volume is occupied by lossless scatterers. A rough estimate of this effect is that the actual loss per unit length in a matrix containing a volume fraction f of lossless scatterers is $1 - f$ of what it would be without the scatterers. By this estimate, for fill factors of 25% we overestimate the loss in the medium by a factor of about 1.3. Based on the results in chapter 5, it does not seem that this will be a significant difference. We will leave a better calculation for a future date.

A.3 Example: Granite Spheres in Soil

Figures A-2 through A-5 illustrate some of the scattering characteristics of granite spheres ($\varepsilon = 5.5 - i0.075$) in a soil matrix ($\varepsilon = 2.0$), at the Magellan radar frequency of 2.385 GHz. The significance of this particular example is explained in section 5.4.1; it is qualitatively representative of the results for many types of scatterer. The value of x, the particle size parameter in the matrix medium (equation A.7), is useful as a rough dividing line for different regimes of particle scattering behavior. For $x \ll 1$, the extinction efficiency is small, and the particles absorb most of the intercepted radiation (thus, the single scattering albedo is low). The scattering pattern is fairly isotropic. This is the Rayleigh scattering regime. For $x \gg 1$, the extinction efficiency approaches 2.0, and the single scattering albedo gradually falls toward 0.5. About half of the incident radiation is scattered into a progressively narrower cone in the forward direction. This is the regime of geometrical optics. For $x \sim 1$, the extinction efficiency and single scattering albedo reach maxima. The scattering pattern is somewhat forward-directed, as it changes from a Rayleigh pattern to a geometrical-optic pattern. This is the regime of the Mie resonance. (In the case at hand, $x = 1$ at $a = 1.4$ cm.)

Figure A-2 illustrates the extinction and scattering efficiencies for spheres of radius up to 20 cm. The maximum extinction efficiency ($Q_{ext} = 4.6$) is reached at a particle radius of 4.5 cm ($x = 3.2$). Figure A-3 plots the particle single scattering albedo.

The resonance peak for this quantity is broad and flat; values of $\varpi_p > 0.95$ are maintained for particle radii in the range 2.3–5.0 cm ($1.6 < x < 3.5$). Figure A-4 shows the extinction and scattering cross sections per unit particle volume. To obtain the actual cross section per unit volume in the scattering layer, these values must be multiplied by the filling factor for particles of each particular size. If the particle size distribution obeys a law where $N(a) \propto a^{-3}$, then there will be equal volumes of particles of all sizes, and this curve directly indicates the relative importance of extinction by particles of different radii. Here, the maximum extinction cross section per unit volume of 87.7 m^{-1} is obtained by particles of radius 3.6 cm ($x = 2.5$).

Figure A-5 displays the scattering pattern for three different particle sizes. The sphere of radius 5 mm is only slightly different from a perfect Rayleigh scatterer. At 3 cm, the incident radiation is scattered more strongly in the forward direction; at 10 cm, the scattering is highly forward directed.

A.4 Nonspherical Scatterers

It is common practice to use Mie scattering theory in conjunction with particles of irregular shape; the assumption is that the scattering properties of an irregular particle, averaged over all possible orientations, are the same as for a spherical particle of the same volume. Thus, the scattering behavior of an ensemble of irregular particles is much like that of an ensemble of spherical particles. Is the assumption valid? This question has been investigated by Cuzzi and Pollack [14]. The remainder of this section is a summary of their findings.

Previous laboratory data (for example, [31]) indicate that the parameters integrated over angle (the extinction, scattering, and absorption efficiencies) are not dependent on sphericity. The major effect is on the phase function. The experimental

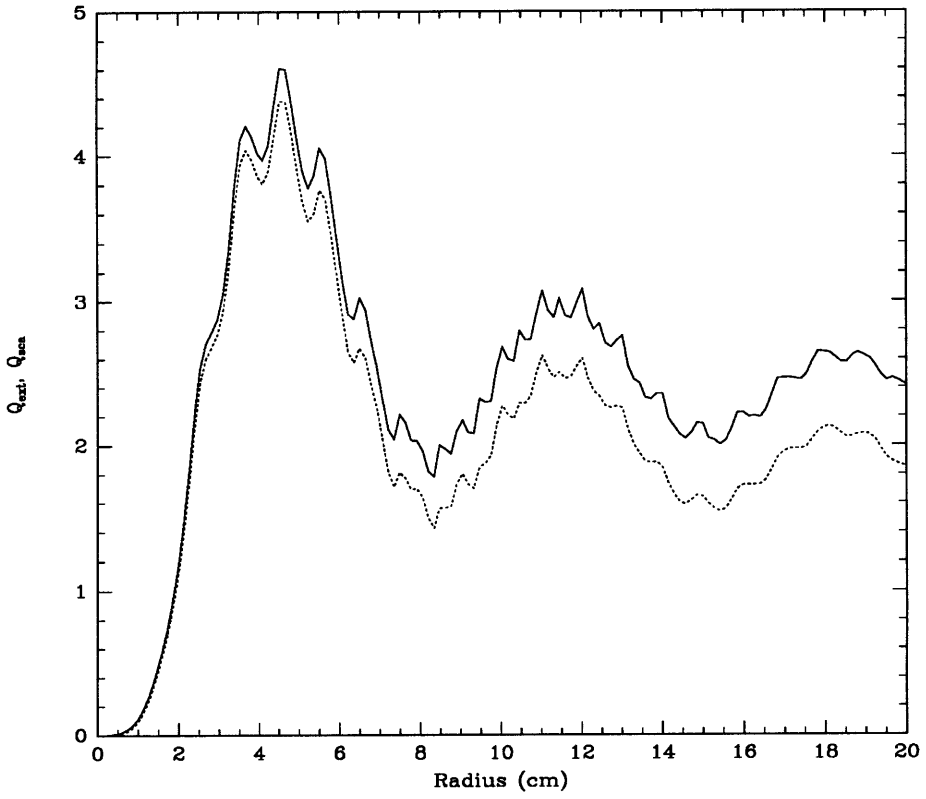

Figure A-2: Extinction (solid) and scattering (dotted) efficiencies of granite spheres ($\varepsilon = 5.5 - i0.075$) in soil ($\varepsilon = 2.0$), calculated by Mie theory.

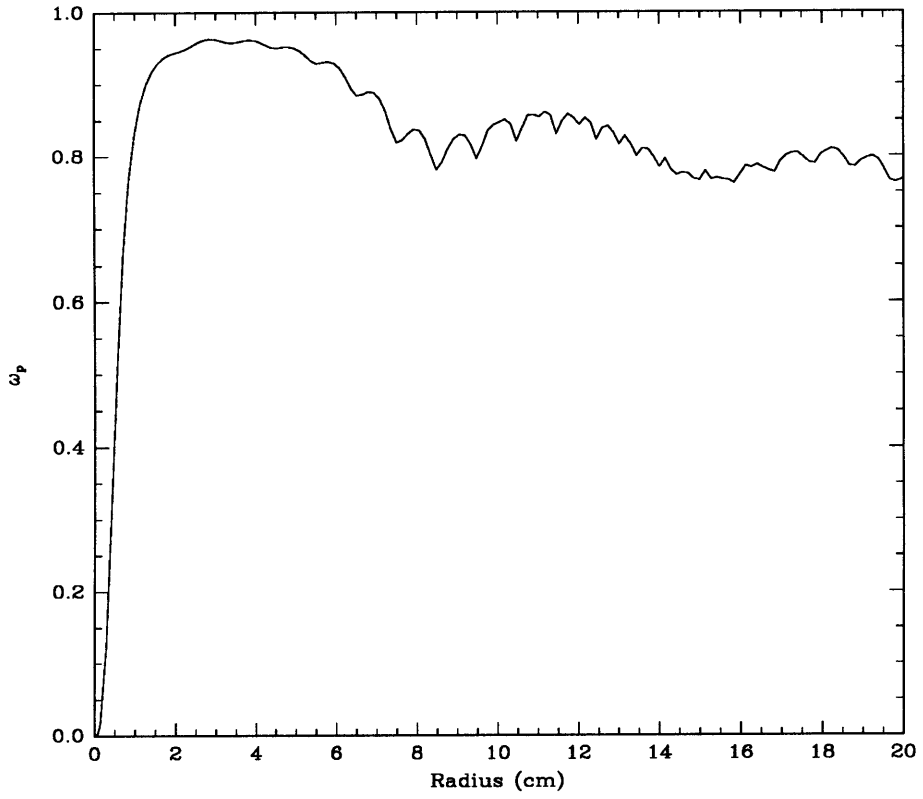

Figure A-3: Single scattering albedos of granite spheres ($\varepsilon = 5.5 - i0.075$) in soil ($\varepsilon = 2.0$), calculated by Mie theory.

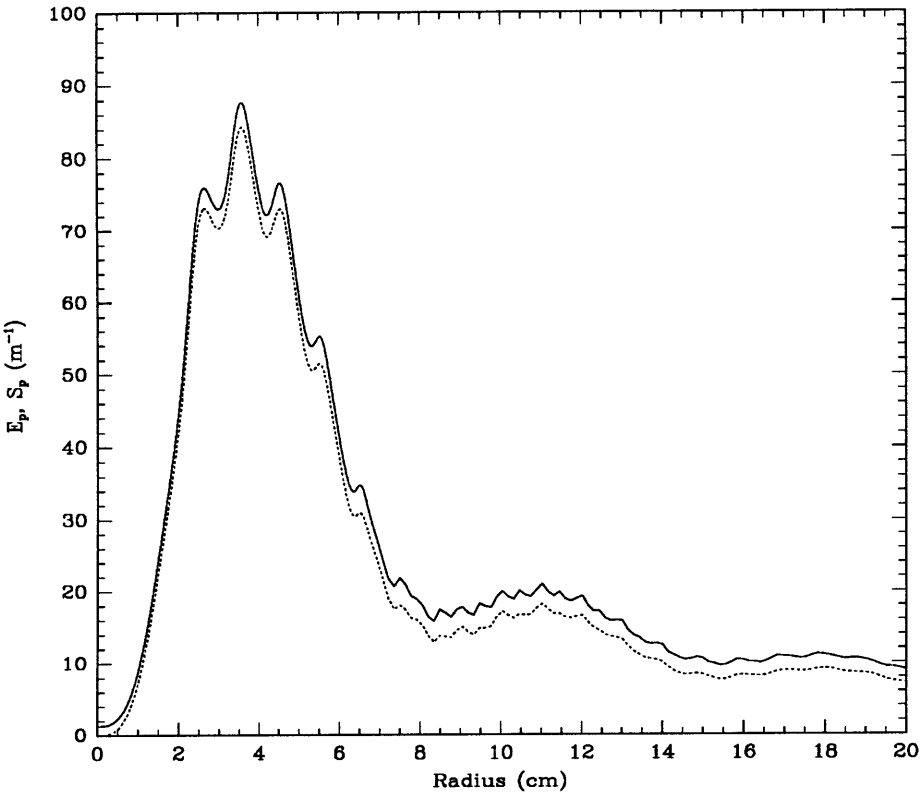

Figure A-4: Extinction (solid) and scattering (dotted) coefficients of granite spheres ($\varepsilon = 5.5 - i0.075$) in soil ($\varepsilon = 2.0$), calculated by Mie theory. The values of E_p and S_p are calculated as cross section per unit particle volume; thus, these values must be multiplied by the volume filling factor for particles of the given size to arrive at the actual coefficient.

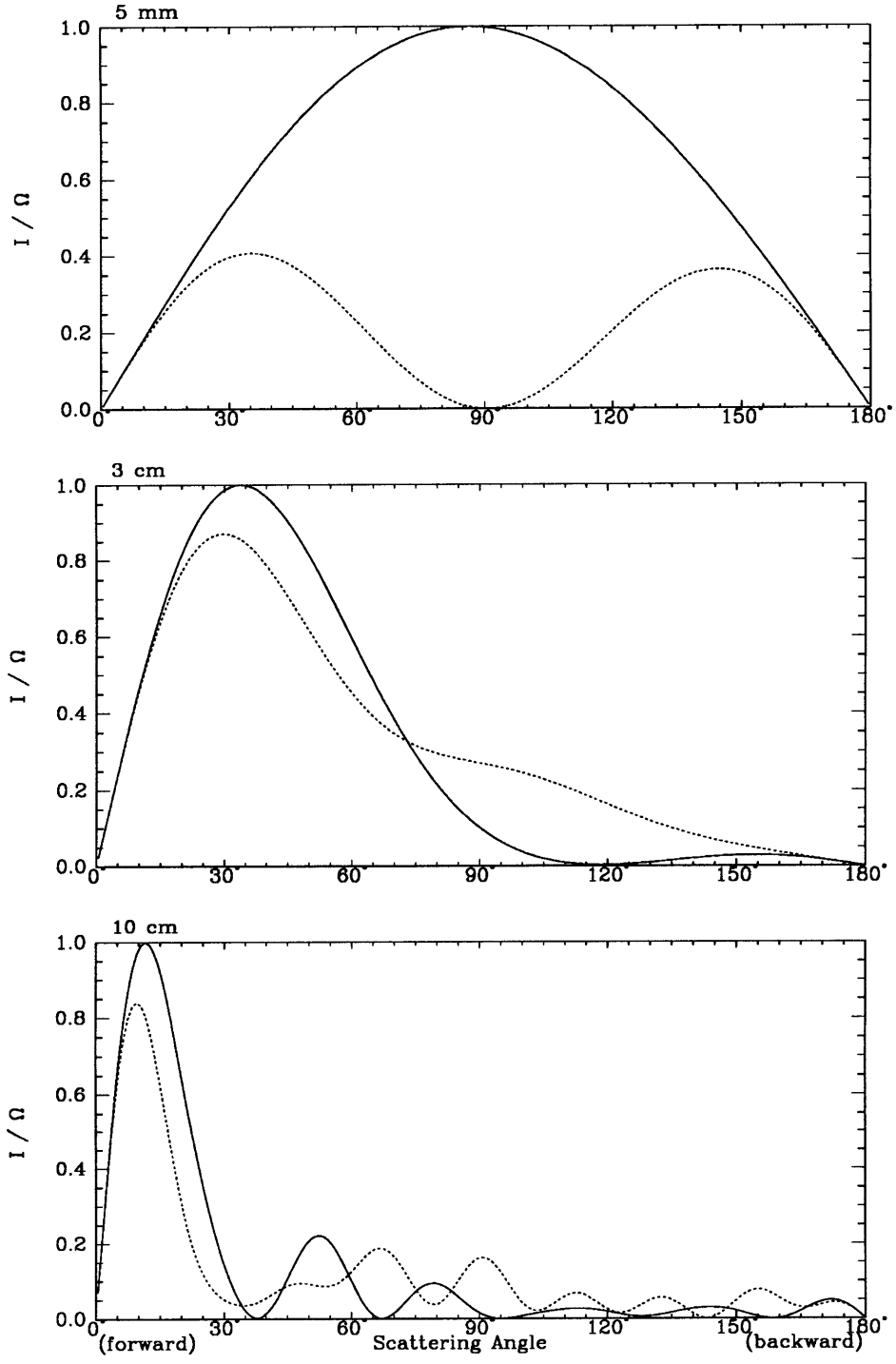

Figure A-5: Radiation scattering pattern for three different sizes of granite spheres ($\varepsilon = 5.5 - i0.075$) in soil ($\varepsilon = 2.0$), calculated by Mie theory. Shown are separate curves for horizontal (solid) and vertical (dotted) polarizations. Values plotted are the intensity functions (equations A.11 and A.12) normalized by solid angle, and to a maximum value of 1.0.

data of Cuzzi and Pollack suggests that, for a given particle shape and permittivity, there is a size below which the particle behaves very much like a spherical Mie scatterer, and above which the scattering behavior diverges from Mie theory. Examples include cubes with size parameter $x = 4$, and corrugated spheres with size paramter $x = 14$, both of which still scatter much like spheres of equal volume.

Above the critical size, the irregularity of the particle permits total internal reflections (these do not occur with spheres); the net effect is to increase the amount of energy scattered into larger scattering angles, producing a more nearly isotropic pattern. Also, the total scattered intensity of larger particles is proportional to their surface area; thus, for a given particle volume, any irregular particle will have a greater scattering efficiency. The absorption efficiency, dependent mainly on volume, will not be significantly changed. Thus, in addition to having higher extinction efficiencies, large irregular particles have greater single scattering albedoes. If $A_{i/s}$ is the ratio of the surface area of an irregular particle to that of a sphere of equal volume, then the scattering efficiency of the irregular particle, $Q_{sca\,i}$, is given by

$$Q_{sca\,i} = A_{i/s} Q_{sca\,s} \tag{A.30}$$

where $Q_{sca\,s}$ is the Mie scattering efficiency of a sphere of equal volume. The single scattering albedo of the irregular particle is

$$\varpi_i = \frac{A_{i/s}}{A_{i/s} + (1/\varpi_s - 1)} \tag{A.31}$$

where ϖ_s is the single scattering albedo of the sphere.

The polarization by scattering from irregular particles has not been studied in detail. Experiments measuring the depolarization of the backscattered component, though, do show that large irregular particles return significant amounts of radiation in the orthogonal linear polarization. (Spheres do not depolarize the backscattered radiation.)

Bibliography

[1] R. E. Arvidson, V. R. Baker, C. Elachi, R. S. Saunders, and J. A. Wood. Magellan: Initial analysis of Venus surface modification. *Science*, 252:270–275, 1991.

[2] L. P. Bayvel and A. R. Jones. *Electromagnetic Scattering and its Applications.* Applied Science Publishers, Englewood, NJ, 1981.

[3] C. F. Bohren and D. P. Gilra. Extinction by a spherical particle in an absorbing medium. In M. Kerker, editor, *Selected Papers on Light Scattering.* Cambridge University Press, 1988. Originally published in *Journal of Colloidal and Interface Science* 72, 1979.

[4] J. Brown. Artificial dielectrics. In J. B. Birks, editor, *Progress in Dielectrics, Volume 2.* John Wiley and Sons, New York, 1960.

[5] M. J. Campbell and J. Ulrichs. Electrical properties of rocks and their significance for lunar radar observations. *Journal of Geophysical Research*, 74:5867–5881, 1969.

[6] R. S. Carmichael, editor. *Handbook of Physical Properties of Rocks.* CRC Press, Boca Raton, FL, 1982.

[7] R. A. F. Cas and J. V. Wright. *Volcanic Successions, Modern and Ancient.* Allen and Unwin, London, 1987.

[8] S. Chandrasekhar. *Radiative Transfer.* Dover, New York, 1960.

[9] B. D. Chapman. *Thermal Radio Emission from the Surfaces of Venus and Mercury.* PhD thesis, Massachusetts Institute of Technology, Cambridge, MA, 1986.

[10] R. Clausius. *Die Mechanische Wärmelehre*, volume 2, pages 62–97. Braunschweig, 1879.

[11] L. Colin. Basic facts about Venus. In D. M. Hunten, L. Colin, T. M. Donahue, and V. I. Moroz, editors, *Venus*. University of Arizona Press, Tucson, AZ, 1983.

[12] J. Conel. Infrared emissivities of silicates: Experimental results and a cloudy atmosphere model of spectral emission from condensed particulate mediums. *Journal of Geophysical Research*, 74:1614–1634, 1969.

[13] D. P. Cruikshank. The development of studies of Venus. In D. M. Hunten, L. Colin, T. M. Donahue, and V. I. Moroz, editors, *Venus*. University of Arizona Press, Tucson, AZ, 1983.

[14] J. N. Cuzzi and J. B. Pollack. Saturn's rings: Particle composition and size distribution as constrained by microwave observations 1. Radar observations. *Icarus*, 33:233–262, 1978.

[15] A. Emslie and J. Aaronson. Spectral reflectance and emittance of particulate materials 1: Theory. *Applied Optics*, 12:2563–2572, 1973.

[16] A. W. England. Thermal microwave emission from a halfspace containing scatterers. *Radio Science*, 9:447–454, 1974.

[17] A. W. England. Thermal microwave emission from a scattering layer. *Journal of Geophysical Research*, 80:4484–4496, 1975.

[18] B. Fegley Jr., A. H. Tremain, and V. L. Sharpton. Venus surface mineralogy: Observational and theoretical constraints. In *Proceedings of Lunar and Planetary Science, Volume 22*, pages 3–19, Houston, 1992. Lunar and Planetary Institute.

[19] K. P. Florenskiy, A. T. Bazilevskiy, G. A. Burb, O. V. Nikolayeva, A. A. Pronin, A. S. Selivanov, M. K. Narayeva, A. S. Panfilov, and V. P. Chemodanov. Panorama of Venera 9 and 10 landing sites. In D. M. Hunten, L. Colin, T. M. Donahue, and V. I. Moroz, editors, *Venus*. University of Arizona Press, Tucson, AZ, 1983.

[20] C. P. Florensky, A. T. Basilevsky, V. P. Kryuchkov, R. O. Kusmin, O. V. Nikolaeva, A. A. Pronin, I. M. Chernaya, Y. S. Tyuflin, A. S. Selivanov, M. K. Naraeva, and L. B. Ronca. Venera 13 and Venera 14: Sedimentary rocks on Venus? *Science*, 221:57–59, 1983.

[21] P. G. Ford and G. H. Pettengill. Venus: Global surface radio emissivity. *Science*, 220:1379–1381, 1983.

[22] P. G. Ford and G. H. Pettengill. Venus topography and kilometer-scale slopes. *Journal of Geophysical Research*, 1992. In press.

[23] P. G. Ford and D. A. Senske. The radar scattering characteristics of Venus landforms. *Geophysical Research Letters*, 17:1361–1364, 1990.

[24] J. B. Garvin. On the role of Mn and Ti at the surface of Venus. In *Lunar and Planetary Science XVI Abstracts*, pages 262–263, Houston, 1985. Lunar and Planetary Institute.

[25] J. B. Garvin and J. W. Head. High dielectric surfaces on the terrestrial planets. In *Lunar and Planetary Science XVI Abstracts*, pages 264–265, Houston, 1985. Lunar and Planetary Institute.

[26] J. B. Garvin, J. W. Head, and L. Wilson. Magma vesiculation and pyroclastic volcanism on Venus. *Icarus*, 52:365–372, 1982.

[27] J. B. Garvin, J. W. Head, and S. H. Zisk. On the origin of high radar reflectivity surfaces on Venus. In *Lunar and Planetary Science XVI Abstracts*, pages 266–267, Houston, 1985. Lunar and Planetary Institute.

[28] R. M. Goldstein and R. R. Green. Ganymede: Radar surface characteristics. *Science*, 207:179–180, 1980.

[29] R. Greeley and R. E. Arvidson. Aeolian processes on Venus. *Earth, Moon, and Planets*, 50:127–157, 1990.

[30] R. Greeley, J. R. Marshall, D. Clemens, A. R. Dobrovolskis, and J. B. Pollack. Venus: Concentrations of radar-reflective minerals by wind. *Icarus*, 90:123–128, 1991.

[31] J. M. Greenberg, R. T. Wang, and L. Bangs. Extinction by rough particles and the use of Mie theory. *Nature Phys. Sci.*, 230:110, 1971.

[32] T. Hagfors. Remote probing of the moon by infrared and microwave emissions and by radar. *Radio Science*, 5:189–227, 1970.

[33] B. Hapke. Bidirectional reflectance spectroscopy: I. Theory. *Journal of Geophysical Research*, 86:3039–3054, 1981.

[34] B. Hapke. Coherent backscatter and the radar characteristics of outer planet satellites. *Icarus*, 88:407–417, 1990.

[35] B. Hapke. Combined theory of reflectance and emittance spectroscopy. In C. Pieters and P. Englert, editors, *Remote Geochemical Analyses*. Cambridge University Press, 1992. In press.

[36] J. W. Head. Assemblages of geologic/morphologic units in the northern hemisphere of Venus. *Earth, Moon, and Planets*, 50/51:391–408, 1990.

[37] J. W. Head, A. R. Peterfreund, J. B. Garvin, and S. H. Zisk. Surface characteristics of Venus derived from pioneer venus altimetry, roughness, and reflectivity measurements. *Journal of Geophysical Research*, 90:6873–6885, 1985.

[38] N. E. Hill, W. E. Vaughan, A. H. Price, and M. Davies. *Dielectric Properties and Molecular Behaviour*. Van Nostrand Reinhold, London, 1969.

[39] B. F. Howell, Jr. and P. H. Licastro. Dielectric behavior of rocks and minerals. *The American Mineralogist*, 46:269–288, 1961.

[40] S. J. Keihm. Effects of subsurface volume scattering on the lunar microwave brightness temperature spectrum. *Icarus*, 52:570–584, 1982.

[41] J. M. Kelly, J. O. Stenoien, and D. E. Isbell. Waveguide measurements in the microwave region on metal powders suspended in paraffin wax. *Journal of Applied Physics*, 24:258–262, 1953.

[42] M. Kerker. *The Scattering of Light and Other Electromagnetic Radiation.* Academic Press, New York, 1969.

[43] A. J. Kliore, V. I. Moroz, and G. M. Keating. The Venus international reference atmosphere. *Advances in Space Science*, 5(11), 1985. COSPAR report JPL-D-2216.

[44] K. B. Klose, J. A. Wood, and A. Hashimoto. Mineral equilibria and the high radar reflectivity of Venus mountaintops. *Journal of Geophysical Research*, 1992. In press.

[45] M. LeMere. JPL IOM 3344-85-060, 23 June 1986.

[46] A. N. Lowan. *Tables of Scattering Functions for Spherical Particles*, volume 4 of *National Bureau of Standards (U.S.), Applied Math Series.* Government Printing Office, Washington, D.C., 1949.

[47] K. Lumme and E. Bowell. Radiative transfer in the surfaces of airless bodies: I. Theory. *Astronomical Journal*, 86:1694–1704, 1981.

[48] Magellan planetary constants and models. JPL D-2300 Rev. D, 9 January 1991.

[49] Magellan radar sensor compensation report. C. Cuevas, Hughes Aircraft Co., editor. Magellan project document HS513, 18 August 1989.

[50] V. I. Moroz. Summary of preliminary results of the Venera 13 and Venera 14 missions. In D. M. Hunten, L. Colin, T. M. Donahue, and V. I. Moroz, editors, *Venus.* University of Arizona Press, Tucson, AZ, 1983.

[51] O. F. Mossotti. Discussione analitica sull' influenza che l'azione di un mezzo dielettrico ha sulla distribuzione dell' elettricità alla superficie di più corpi elet-

trici disseminati in esso del socio attuale. *Mem. Math. Fisica, Soc. Ital. Sci., Modena*, 24:49, 1850.

[52] S. D. Nozette. *The Physical and Chemical Properties of the Surface of Venus.* PhD thesis, Massachusetts Institute of Technology, Cambridge, MA, 1982.

[53] J. J. O'Dwyer and E. Harting. Theories of dielectric loss. In J. B. Birks, editor, *Progress in Dielectrics, Volume 7.* Heywood Books, London, 1967.

[54] G. R. Olhoeft and D. W. Strangway. Dielectric properties of the first 100 meters of the moon. *Earth and Planetary Science Letters*, 24:394–404, 1975.

[55] E. I. Parkhomenko. *Electrical Properties of Rocks.* Plenum, New York, 1967.

[56] G. H. Pettengill. Physical properties of the planets and satellites from radar observations. *Annual Review of Astronomy and Astrophysics*, 16:265–292, 1978.

[57] G. H. Pettengill, P. G. Ford, and B. D. Chapman. Venus: Surface electromagnetic properties. *Journal of Geophysical Research*, 93:14,881–14,892, 1988.

[58] G. H. Pettengill, P. G. Ford, W. T. K. Johnson, R. K. Raney, and L. A. Soderblom. Magellan: Radar performance and data products. *Science*, 252:260–265, 1991.

[59] G. H. Pettengill, P. G. Ford, and S. Nozette. Venus: Global surface radar reflectivity. *Science*, 217:640–642, 1982.

[60] G. H. Pettengill, P. G. Ford, and R. J. Wilt. Venus surface radiothermal emission as observed by Magellan. *Journal of Geophysical Research*, 1992. In press.

[61] G. H. Pettengill, D. F. Horwood, and C. H. Keller. Pioneer Venus orbiter radar mapper: Design and operation. *I.E.E.E. Transactions on Geoscience and Remote Sensing*, GE-18(1):28–32, 1980.

[62] R. J. Phillips, R. E. Arvidson, J. M. Boyce, D. B. Campbell, J. E. Guest, G. G. Schaber, and L. A. Soderblom. Impact craters on Venus: Initial analysis from Magellan. *Science*, 252:288–297, 1991.

[63] W. H. Press, B. P. Flannery, S. A. Teukolsky, and W. T. Vetterling. *Numerical Recipes.* Cambridge University Press, Cambridge, 1986.

[64] R. S. Saunders and G. H. Pettengill. Magellan: Mission summary. *Science*, 252:247–249, 1991.

[65] A. Seiff. Thermal structure of the atmosphere of Venus. In D. M. Hunten, L. Colin, T. M. Donahue, and V. I. Moroz, editors, *Venus.* University of Arizona Press, Tucson, AZ, 1983.

[66] R. T. Shin and J. A. Kong. Theory for thermal microwave emission from a homogeneous layer with rough surfaces containing spherical scatterers. *Journal of Geophysical Research*, 87:5566–5576, 1982.

[67] S. C. Solomon, S. E. Smrekar, D. L. Bindschadler, R. E. Grimm, W. M. Kaula, G. E. McGill, R. J. Phillips, R. S. Saunders, G. Schubert, S. W. Squyres, and E. R. Stofan. Venus tectonics: An overview of Magellan observations. *Journal of Geophysical Research*, 1992. In press.

[68] J. A. Stratton. *Electromagnetic Theory.* McGraw-Hill, New York, 1941.

[69] Y. A. Surkov. Studies of Venus rocks by Veneras 8, 9, and 10. In D. M. Hunten, L. Colin, T. M. Donahue, and V. I. Moroz, editors, *Venus.* University of Arizona Press, Tucson, AZ, 1983.

[70] Y. A. Surkov, L. P. Moskalyova, V. P. Kharyukova, A. D. Dudin, G. G. Smirnov, and S. Y. Zaitseva. Venus rock composition and the Vega 2 landing site. *Journal of Geophysical Research*, 91:E215–E218, 1986. Proceedings of the Seventeenth Lunar and Planetary Science Conference, part 1.

[71] K. A. Tryka and D. O. Muhleman. Reflection and emission properties in Alpha Regio. *Journal of Geophysical Research*, 1992. In press.

[72] L. Tsang and J. A. Kong. Theory for thermal microwave emissions from a bounded medium containing spherical scatterers. *Journal of Applied Physics*, 48:3593–3599, 1977.

[73] F. T. Ulaby, T. H. Bengal, M. C. Dobson, J. R. East, J. B. Garvin, and D. L. Evans. Microwave dielectric properties of dry rocks. *I.E.E.E. Transactions on Geoscience and Remote Sensing*, 28:325–336, 1990.

[74] F. T. Ulaby, T. H. Bengal, J. R. East, M. C. Dobson, J. B. Garvin, and D. L. Evans. Microwave dielectric spectrum of rocks. Technical report, University of Michigan, Ann Arbor, MI, March 1988.

[75] F. T. Ulaby, R. K. Moore, and A. K. Fung. *Microwave Remote Sensing Fundamentals and Radiometry*, volume 1 of *Microwave Remote Sensing, Active and Passive.* Artech House, Norwood, MA, 1981.

[76] F. T. Ulaby, R. K. Moore, and A. K. Fung. *Radar Remote Sensing and Surface Scattering and Emission Theory*, volume 2 of *Microwave Remote Sensing, Active and Passive.* Artech House, Norwood, MA, 1982.

[77] L. K. H. van Beek. Dielectric behavior of heterogeneous systems. In J. B. Birks, editor, *Progress in Dielectrics, Volume 7.* Heywood Books, London, 1967.

[78] H. C. van de Hulst. *Light Scattering by Small Particles.* Dover, New York, 1981.

[79] A. R. von Hippel. *Dielectrics and Waves.* M.I.T. Press, Cambridge, MA, 1954.

[80] R. C. Weast, editor. *CRC Handbook of Chemistry and Physics.* CRC Press, Boca Raton, FL, 1987.

[81] H. Williams and A. R. McBirney. *Volcanology.* Freeman, Cooper, and Co., San Francisco, 1979.